Physics – Uspekhi **65** (10) 1071 – 1103 (2022)

INSTRUMENTS AND METHODS OF INVESTIGATION PACS numbers: **29.30. – h**, 52.25.Os, **52.70. – m**

Spectroscopy of small gas components of a nonequilibrium low-temperature plasma

V N Ochkin

DOI: https://doi.org/10.3367/UFNe.2021.07.039026

Contents

Abstract. The state of the art and prospects for the development of quantitative optical spectroscopy methods for analyzing the composition of small chemically active components of a nonequilibrium plasma are discussed. The capabilities of the methods are considered in combination with the conditions of applicability, both for fundamental research in the fields of plasma physics and chemistry, and for monitoring the technological processes in reactors for the benefit of the energy sector, micro- and nano-electronics, medicine, the creation of optical coatings, and generating active radicals and excited particles.

Keywords: spectroscopy, plasma, equilibrium

1. Introduction

Plasma, the most widespread of the four known states of matter in nature [1], has been and remains the subject of ongoing research. This is motivated by a variety of applications, even at the earliest stages of the development of society, although a wide class of these objects was assigned to a separate aggregate group only in 1879 (Crookes), and the term 'plasma' for a partially or fully ionized electrically conducting quasi-neutral medium was introduced in 1928 (Langmuir) [2]. For a long time, interest in plasma was mainly related to its thermal and optical properties that allow applications for processing food and materials, room heating, illumination, and navigation. A large group of plasma forms, from primordial fire to jet engine torches, consists of various types of flames supported by combustion reactions. The scope of plasma forms of practical interest has been drastically widened by the application of electric current and voltage sources, i.e., discharges of various types, to produce them. Although some substances in 'traditional' aggregate states, e.g., charged particles in solids, also manifest plasma-like properties, it is accepted to consider objects formed of gaseous media to be plasma. Under terrestrial conditions, they are the atmosphere and ionosphere, as well as laboratory and technological devices. For them, the degree of ionization, as a rule, is not high, less than $10^{-1} - 10^{-3}$; such plasma is referred to as low-temperature plasma (LTP). If the notion of temperature has a physical sense to describe the motion of various sorts of particles in the translational and/or internal degrees of freedom, LTP heating does not exceed 10^5 K.

Interest in high-temperature plasma (HTP) heated above 10^6 K, when the gas particles are multiply ionized up to the nucleus charge, is mainly due to the possibility of nuclear reactions in it [3, 4]. In nature, this happens, e.g., in 'young' stars. Since the 1950s, efforts in the physics and technology of such plasma forms have been intensified in the direction of creating them under terrestrial conditions, prognosing their properties upon spontaneous initiation (explosion) with the intension of creating alternative sources of power using controlled thermonuclear fusion (CTF). In this case, the processes that restrict plasma stability are of importance; this is a separate field of investigation beyond the scope of this review. However, experience shows that, even in such systems due to incomplete isolation and/or dynamic peculiarities, processes beyond nuclear reaction zones, e.g., near reactor walls, are of importance. In fact, the presence of such zones is

V N Ochkin
Lebedev Physical Institute, Russian Academy of Sciences,
Leninskii prosp. 53, 119991 Moscow, Russian Federation
E-mail: ochkinvn@lebedev.ru

Received 4 June 2021, revised 22 July 2021
Uspekhi Fizicheskikh Nauk **192** (10) 1145 – 1178 (2022)
Translated by V L Derbov

'pay' for the isolation of central regions and the possibility of utilizing the released energy. LTP studies have accelerated and expanded since the 1960s due to the development of gas lasers, applications in ecology and medicine, the technology of elements in optics and electronics, etc.

LTP properties strongly depend on the plasma's chemical composition; elucidation of the mechanism of its formation is one of the central tasks of plasma physics and diagnostics. A deviation from thermodynamic equilibrium is characteristic of LTP. Even with the same chemical formula, particles possess different reactivity in different excited states with a discrete spectrum energy of terms. The proportion and role of atomic and molecular radicals and charged particles in chemical transformations increase; to describe the balance of particles, a large number of processes must be taken into account. Current modeling facilities allow operations with arrays of $10^2 - 10^4$ reactions, which implies using nearly the same number of input parameters in the form of reaction rate constants and plasma macroscopic characteristics. Even in the local approximation, this leads to difficulties because of limited accuracy and reliability. The completeness of a kinetic scheme also implies discussion in each particular case. Experimental methods of determining the concentrations of various particles in various states take on particular significance. Many analytic methods developed for gas analysis, although sometimes used for plasma, suffer from limitations related to correct sampling [5]. In this relation, methods of quantitative spectroscopy that do not disturb the plasma advantageously differ from them.

By now, LTP spectroscopy has developed into a specific line of research. Early papers and monographs mainly discussed the issues of equilibrium plasma spectroscopy [2, 6]. Later, more attention was paid to plasma forms with substantial deviations from thermodynamic equilibrium and selectivity of elementary processes [7–9], including those with nonequilibrium chemical kinetics [10]. The main current methods of spectroscopy, the physical grounds for their use, and interpretations of results of measurements under nonequilibrium conditions are considered in monograph [11], while some general issues are presented in reviews [5, 12–14]. Tens of more particular reviews on LTP spectroscopy achievements related to either a new measurement technique or application to new subjects are being published.

Review [15] discusses some methods of laser spectroscopy for measuring the concentration of radicals in plasma at atmospheric pressure. Reviews [16, 17] present the results of measuring the content of atoms and simple molecules in atmospheric-pressure plasma using a number of traditional diode and quantum-cascade lasers. A few reviews are devoted to the spectroscopy of radicals in plasma jets from capillaries and microdischarges. Due to favorable conditions for transport in the atmosphere, they find application in medicine, in biology, for the activation and inhibition of drugs, and for the disinfection of food [18–21]. Series of reviews are devoted to classical and laser spectroscopy of plasma in laboratory and industrial reactors for spurring coatings, etching parts in microelectronics, and growing nanostructures [22, 23]. Studies of plasma by intracavity laser spectroscopy and the attenuation of light in an external optical cavity are the subject of reviews [24–26]. Several reviews analyze studies that used nonlinear laser spectroscopy, including fluorescence and multiphoton excitation [27], as well as various versions of four-wave mixing [28]. Recent review [5] analyzes the state of the art in low-pressure plasma studies under conditions typical of a near-wall layer in electric-discharge CTF facilities; attention is focused on laser absorption methods and proposals for new methods of optical actinometry.

The present review of the current state of LTP quantitative spectroscopy is based on a list of particles studied under a wide range of conditions. The capabilities of new methods being outlined and those already used are compared. We intend

— to systemize methods by general characteristics accepted in spectroscopy and their correspondence to physical applicability conditions in nonequilibrium LTP;

— to give an idea of the prevalence and success of the methods used and the ranges of particle concentration measurements;

— to note the features of the experimental technique and the validity of its application to various objects;

— to evaluate the factors affecting the sensitivity and accuracy of measurements, and peculiarities of detecting and processing signals related to particle concentrations;

— to assess the nature of the change in priorities in the choice of spectroscopy methods and the prospects for emerging new opportunities.

Such an outline could become a base for further generalizations of appearing results and understanding the prospects of the spectroscopy of nonequilibrium LTP small components.

2. Direct absorption spectroscopy

2.1 Absorption and concentration of particles, general notes

The intensity of light at frequency ν of an atomic transition $u \to l$ (u and l being the upper and lower energy levels) passing distance z through a uniform medium decreases according to the Beer–Bouguer–Lambert (BBL) law

$$I(\nu, z = l) = I(\nu, z = 0) \exp\left[-\chi_{lu}(\nu) l\right] . \tag{1}$$

The quantities $\chi_{lu}(\nu)$, $\chi_{lu}(\nu) l$ are the spectral absorption index and coefficient, respectively. The relation between the integral absorption coefficient χ_{lu} with the populations of the lower and upper energy levels N_l, N_u has the form

$$\chi_{lu} = \int \chi_{lu}(\nu)\, \mathrm{d}\nu = \frac{h\nu_{ul}}{c}\, B_{lu} N_l \left(1 - \frac{g_l}{g_u}\frac{N_u}{N_l}\right) , \tag{2}$$

where g_u, g_l are the statistical weights, ν_{ul} is the center frequency of the absorption line contour, and B_{lu} is the Einstein coefficient for absorption. Instead of B_{lu}, other Einstein coefficients are used: the oscillator strengths $f_{ul} = -f_{lu} g_l / g_u$ and the line strength $S_{ul} = S_{lu} = S$ [2, 29].

The form of the relation between χ_{lu} and the absorption index for the center of the line contour $\chi_{lu}(\nu = \nu_{lu}) = \chi_{0,lu}$ depends on the line broadening mechanism [2, 6, 9, 29]. Ignoring the induced radiation ($N_l \gg N_u$) and assuming λ be measured in nanometers, N_l in cm^{-3}, and χ in cm^{-1}, we get for Doppler or Lorentz broadening

$$\begin{aligned} \chi_{0,lu} &= 1.23 \times 10^{-33}\, \frac{g_u}{g_l}\, \frac{A_{ul}}{\Delta\lambda_{\mathrm{D}}}\, \lambda_{lu}^4 N_l , \\ \chi_{0,lu} &= 0.84 \times 10^{-33}\, \frac{g_u}{g_l}\, \frac{A_{ul}}{\Delta\lambda_{\mathrm{L}}}\, \lambda_{lu}^4 N_l , \end{aligned} \tag{3}$$

where $\Delta\nu_D$, $\Delta\nu_L$ are the half-maximum widths, respectively. When $N_l \gg N_u$, the notion of cross section σ [cm^2] of light absorption by one particle at the lower energy level is also used in practice:

$$\sigma_{lu}(\nu) = \frac{\chi_{lu}(\nu)}{N_l} . \quad (4)$$

Absorption methods determine the difference between (or ratio of) N_l and N_u. In many cases, induced transitions can be ignored and the measurement yields the values of lower (absorbing) level populations. Generally, to determine the total concentration of particles N, it must be related to the population N_k of a particular energy level, in the present case, the absorbing one:

$$N_k = \frac{N g_k}{Q_{in}} , \qquad Q_{in} = \sum_i g_i N_i , \quad (5)$$

where Q_{in} is the so-called internal partition function (statistical sum over the bound states) of the particle. The statistical weights are determined by the structure of particles, and the quantities Q_{in} depend on both the structure of terms and the conditions of their excitation.

Under the thermodynamic condition, Q_{in} are determined by the unique temperature T,

$$Q_{in} = \sum_i g_i \exp\left(-\frac{\Delta E_{i0}}{k_B T}\right) , \quad (6)$$

if the energy ΔE_{i0} of the levels is counted from the ground state $k = l = 0$, k_B being the Boltzmann constant. The rules for calculating g_l and Q_{in} with the structure and symmetry of terms taken into account are described in Ref. [11]. In the absence of equilibrium, the quantity Q_{in} should be calculated, generally, by direct summation (5) over all states, which is practically unreal, so that additional assumptions and models are unavoidable.

For *atoms* and their ions, the internal states are the electronic ones. The number of excited energy levels can be rather large, but under plasma conditions, it is limited because of the interaction of charged particles [11]. The Debye energy of the interaction of electrons is e^2/r_D, and the atom ionizes spontaneously in states with a smaller binding energy — this is the effect of ionization potential lowering. Under the conditions characteristic of LTP, as a rule, energy levels with the principal quantum number $n \leqslant 40$ can be observed.

Another limitation for the number of energy levels to be taken into account is due to the fact that, as a rule, the energies of the first excited states already exceed the mean energies of electrons in LTP. If the lower level of a transition is the ground state and the energy distribution of electrons is Maxwellian, then in Eqn (6) the temperature corresponds to that of electrons, $T \approx T_e$. In this case, the value of the statistical sum can be replaced with the value of the ground state statistical weight [11].

Electronic states of *molecules* have an energetically dense vibrational-rotational structure. For many molecules with the number of atoms $N_a \leqslant 5-7$, the approximate independence of different kinds of particle motion in different degrees of freedom is well fulfilled, which leads to an expression for the internal partition function,

$$Q_{in} = Q_e Q_v Q_r , \quad (7)$$

where Q_e, Q_v, and Q_r are the electronic, vibrational, and rotational partition functions.

The *electronic partition function* Q_e is found by analogy with that in the case of atoms.

To calculate the *vibrational* partition function Q_v, the harmonic oscillator approximation is commonly used. In the same approximation, based on the analysis of relaxation processes due to collisions of the particles (vibration exchange and quenching), the deviation from thermodynamic equilibrium can be taken into account by introducing individual vibrational temperature T_v for each oscillator. This is justified for a long-lived ground state or a metastable excited electronic state. In short-lived excited states (with lifetimes shorter than the vibrational relaxation time) depending on the excitation mechanism, the values of T_v can differ from those for the ground state or cannot be introduced at all [30].

For a *diatomic* molecule, direct summation in Eqn (6) with $\Delta E_{v0} = v\nu$ (instead of k, we use a generally accepted notation v to denote a vibrational energy level number, ν being the oscillator frequency) with an infinite upper limit yields

$$Q_v = \left[1 - \exp\left(-\frac{hc\nu}{k_B T_v}\right)\right]^{-1} , \quad (8)$$

where the frequency ν is expressed in wavenumber units [cm^{-1}] and it is taken into account that for all diatomic molecules $g_v = 1$.

For vibrations of a *polyatomic* molecule, an individual oscillator corresponds to each normal mode frequency ν_n. Summation (6) for the number of modes n with the degeneracy multiplicity d_n and the statistical weights taken into account yields [31, 32]

$$Q_v = \prod_{n=1}^{n'_v} (1 - Z_n)^{-d_n} , \qquad Z_n = \exp\left(-\frac{hc\nu_n}{k_B T_{vn}}\right) , \quad (9)$$

where T_{vn} is the vibrational temperature in the nth mode.

When calculating the *rotational* partition function by means of Eqn (6), the model of rigid rotator is most frequently used. The rotational and kinetic temperatures are assumed to be equal, $T_r = T$, due to the rapid energy exchange between the rotating molecules and translationally moving ones. As in the case of vibrational temperatures T_v, the introduction of T_r is physically justified for long-lived electronic states (with the lifetime longer than the time of rotation-translational energy exchange) [11, 31]. For *diatomic* molecules,

$$Q_r = \frac{1}{\sigma} \frac{k_B T_r}{hcB_v} , \quad (10)$$

where B_v is the rotational constant of the vibrational energy level v, and the symmetry number (taken into account in the statistical weight) is $\sigma = 1$ for heteronuclear molecules and $\sigma = 2$ for homonuclear ones.

For *polyatomic* molecules,

$$Q_r = \frac{1}{\sigma} \sqrt{\frac{\pi}{A_v B_v C_v} \left(\frac{k_B T_r}{hc}\right)^3} , \quad (11)$$

where A_v, B_v, C_v are the rotational constants, not equal to each other in asymmetric top molecules. For symmetric tops, two of these constants coincide. The values of $\sigma = 1-24$ for a

number of molecules with the number of atoms from 2 to17 are presented in Ref. [11].

Approximation (7) for polyatomic molecules corresponds to vibration amplitudes and centrifugal stretching that are small compared to the internuclear distance. It is valid in most molecules with small number of atoms $N_a \leqslant 5-7$ at a relatively low level of energy in internal degrees of freedom. An example of violation of these conditions is the class of polyatomic molecules with internal rotations or torsional vibrations.

If the potential barrier that impedes free internal rotation of molecular fragments is high enough compared to the excitation energy (in equilibrium, to the temperature), then torsional vibrations arise, which can be considered an additional vibrational degree of freedom with the corresponding contribution to the vibrational partition function. If the barrier is exceeded and free internal rotation arises, the motion should be attributed to a rotational degree of freedom rather than a vibrational one, with the appropriate contribution to the rotational partition function. In this case, the symmetry numbers σ will also change. These issues have been considered in Refs [32, 33]. The data on barrier values in a number of molecules with internal rotation are presented in Refs [11, 33]. Direct calculations show that, for example, in the relatively simple molecule CH_2, Eqn (8) underestimates the internal partition function Q_{in} by nearly 40% at 300 K, and by nearly 3.5 times at 1000 K [33]. The appropriate corrections are important for absorption measurements.

2.2 Methods of absorption spectroscopy

In the absorption measurements of small concentrations of particles, the sensitivity is of importance. At the same time, to determine the total concentrations under nonequilibrium conditions, data on the distribution of particles over the excited states should be obtained, and it is often desirable to measure the concentrations for various sorts of particles. This implies the development and use of precise quantitative methods with wide spectral and dynamic ranges and the sensitivity retained. Practically, the set of such conditions makes it necessary to combine several methods. Some of them are known from general analytic spectroscopy, others are specific just to plasma investigations. They can be divided into three groups by the spectrum type of the radiation transilluminating the plasma and the method of detecting absorption.

2.2.1 Absorption against the continuum background. In the measurement region, source E transilluminating plasma P (Fig. 1) has a continuous spectrum, while the plasma absorption spectrum consists of discrete lines. A spectral instrument with entrance slit Sp selects an interval $\Delta\nu$ of frequencies including a line of plasma absorption. A single line is selected; within the interval $\Delta\nu$, the continuum intensity change is minor, $\Delta\nu_{\alpha\beta} > \Delta\nu > \Delta\nu_{ul}$, where $\Delta\nu_{\alpha\beta}$ is the spectral separation from the closest neighboring absorption line, and $\Delta\nu_{ul}$ is the half-width of the absorption line.

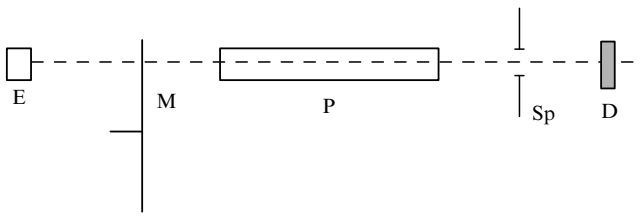

Figure 1. Absorption measurement. P — plasma, E — light source, Sp — spectrometer, M — modulator, D — detector.

To relate the intensity change to the populations of energy levels (see Eqn (2)), the notion of total absorption A_G is used:

$$A_G = \Delta\nu \frac{I_0 - I}{I_0} = \Delta\nu A_L \,, \tag{12}$$

where I_0, I are the intensities of light from the source E within the frequency interval $\Delta\nu$ before and after passing through the plasma. For homogeneous plasma with length L,

$$A_G = \int_{\Delta\nu} \left[1 - \exp\left(-\chi_{lu}(\nu)L\right)\right] \mathrm{d}\nu \,. \tag{13}$$

For the Doppler-broadened contour center,

$$A_G = \frac{1}{2}\sqrt{\frac{\pi}{\ln 2}}\, \Delta\nu_D \chi_{0,lu} L S(\chi_{0,lu}L) \,, \tag{14}$$

and for the Lorentz-broadened one,

$$A_G = \frac{\pi}{2}\, \Delta\nu_L \chi_{0,lu} L S'(\chi_{0,lu}L) \,. \tag{15}$$

The Ladenburg–Levi function S and the Ladenburg–Reiche function S' that enter Eqns (14) and (15) are tabulated in Ref. [9]. In the case of mixed Voigt broadening, the quantities $A_G(\chi_{0,lu}L)$ are calculated numerically [9, 11]. In graphical form, they are called van-Geld growth curves. For information on the calculation of S and S' functions for unresolved multiplets, see Ref. [11].

Let us note some of the circumstances not always taken into account. From Eqns (3), (12)–(15), it is seen that, independent of the broadening type for the given $\chi_{0,lu}L$, the measured quantity A_L becomes less as the ratio $\Delta\nu/\Delta\nu_{lu}$ increases. This limits the measurement sensitivity against the background of the continuum, since $\Delta\nu$ is determined by the spectral instrument. An increase in the resolution is accompanied by a decrease in the aperture ratio and signal-to-noise ratio of the detection.

When measuring absorption, a detector D fixes the light from both source E and plasma P (see Fig. 1). The total number of spontaneous transitions per unit time in a unit volume of plasma and the number of induced transitions caused by the radiation field of the transilluminating source with the spectrum $u_{\nu E}$ is equal to $N_u A_{ul} + N_u B_{ul} u_{\nu E}$. The number of absorption events amounts to $N_l B_{lu} u_{\nu E}$. If the radiation from the source and from the plasma propagate within the same solid angle, then, for an equal number of events,

$$u_{\nu E} h\nu_{ul}(N_u B_{ul} - N_l B_{lu}) = N_u A_{ul}\, h\nu_{ul} \,, \tag{16}$$

so that the plasma does not distort the source spectrum $u_{\nu E}$ and no absorption is detected. This corresponds to the condition of so-called spectral line reversal [34]. For a source with a black-body spectrum at a temperature of T and $u_{\nu E} = u_{\nu T}$,

$$\frac{N_u}{N_l} = \frac{g_u}{g_l} \exp\left(-\frac{h\nu_{ul}}{k_B T}\right) , \tag{17}$$

and the reversal occurs at the relative population of energy levels u and l, corresponding to the 'excitation temperature'

T_{exc} of particles in the plasma, equal to the temperature of the transilluminating source. Against the background of the source spectrum, the lines of plasma emission are seen at $T_{exc} < T$ and the lines of plasma absorption, at $T_{exc} > T$. Expression (17) can be applied as well to a source different from a black body (in this case, T has the sense of brightness temperature T_B) and to the 'excitation temperature' of particles averaged over a few optical transitions. To measure the absorption and the concentration of particles, the source should have brightness temperature $T_B > T_{exc}$, which can not always be estimated a priori for a nonequilibrium plasma. The difficulty can be avoided in experiments; for example, a modulator M placed between the source and the plasma can be used to avoid recording the light from plasma by the detector (see Fig. 1). In the case of lock-in detection at the modulation frequency, the plasma intrinsic emission plays the role of a background, its effect reducing to a shift of the working point of the detection system, which imposes a condition on the linearity of its response or a requirement to take into account the arising nonlinearity. As a rule, for a steady-state object and source at moderate intensities and photoelectric recording, the linearity condition is valid. If the plasma object is pulsed, it is also necessary to ensure the necessary modulation frequency, operation rate of the detector, and detection system bandwidth.

The possibility of saturation of the optical transition should also be taken into account. Let an entire beam of transmitted light with power P and cross section A be collected at the detector. Then, power change ΔP due to the absorption is [35, 36]

$$\Delta P = IA\,\frac{\sigma_{lu} N_l}{1 + I/I_s}\,L\,, \tag{18}$$

where $I = P/A$, I_s is the saturation power density. The minimum measured value $\Delta P = \Delta P_{min}$ is determined by the noise level. For example, in the typical case of photoelectric detection with the Poisson statistics of photoelectrons [37],

$$\Delta P_{min} = \xi' \sqrt{\frac{P h\nu_{lu}}{\Delta t\,\eta_D}}\,, \tag{19}$$

where Δt is the registration time, and η_D is the quantum yield of the photodetector. The factor $\xi' \sim 1$ depends on how the acceptable signal-to-noise ratio is defined in a particular measurement, and we will not specify it for estimates.

The minimum detectable number N'_{min} of particles related to ΔP_{min} at the lower energy level l in the light beam zone is reached at $I = I_s$,

$$N'_{min} = 2\sqrt{\frac{A\tau_{ul}}{\Delta t\,\eta_D \sigma_{lu}}}\,. \tag{20}$$

Practical measurements in the saturation regime, however, face certain difficulties associated with the nonlinear dependence of ΔP on P. It is more convenient to choose the regime with $I < I_s$ [35], the sensitivity degrading not being too much; according to Eqns (18)–(20), for $I = 10^{-2} I_s$, the quantity N'_{min} increases fivefold. The absolute power of light remains high. For example, the typical saturation intensity for resonance transitions in atoms is $I_s \sim 10$ W cm^{-2}. For a beam with a cross section of 1 cm^2, the corresponding light power is 0.1 W. Usually, noises are characterized by the noise equivalent power (NEP), at which the signal-to-noise ratio equals 1, or a reciprocal quantity, the detection ability $D^* = (\mathrm{NEP})^{-1}$. At high radiation power, the detector response is large and its intrinsic noises are not so critical. So, in the IR spectral region, where the limitations because of thermal noise are typical, using modern detectors with $\eta_D \sim 0.4$ and detection ability $D^* \sim 10^{10}$ cm Hz W^{-1} at wavelengths $\lambda \sim 10$ μm, in absorption measurements, it is possible to ignore the noises at power density $P > 1$ mW cm^{-2}. For more details on measuring the absorption against the noise background, see Ref. [38].

2.2.2 Absorption of light with a limited spectrum. Source E (see Fig. 1) emits light in the frequency band $\Delta\nu$ coincident at least partially with the line spectrum of plasma absorption (see Eqn (12)). The light is modulated by chopper M at a signal detection frequency from detector D, and the intrinsic radiation of the plasma is not recorded. A spectral instrument, if used, plays the role of a filter to select a portion of the spectrum in the region to be investigated. This known approach [39] is developed for various combinations of conditions in the light source and plasma studied. In application to equilibrium plasma, this technique is called atomic absorption (line absorption) and is used in the elemental analysis of different substances, when the plasma simultaneously plays the role of atomizer, too. In the simple case, when an object identical to the studied one is used as a source for transillumination (e.g., two discharge tubes), both having plasma length L for a singlet line

$$A_L^* = 2\left[1 - \frac{S^*(2\chi_{0,lu}L)}{S^*(\chi_{0,lu}L)}\right], \tag{21}$$

where $S^* = S$ for Doppler broadening, and $S^* = S'$ for the Lorentz one. Table 1 presents numerical values of the absorption function (21) for the Doppler (A_L) and Lorentz (A'_L) broadening. The bottom line presents the values of $A_L^* = A_L^0 = 1 - \exp(-\chi_{0,lu}L)$ for the case when source E emits a monochromatic line with the frequency at the maximum of the plasma absorption line. In all three cases, relative changes in the source line intensity transilluminating the plasma with the fixed values of $\chi_{0,lu}$ are comparable within a range of no worse than a factor of ~ 2. Therefore, the use of a high-resolution spectral instrument or transilluminating source with the emission line narrower than the absorption line will not lead to a principal increase in sensitivity. The absorption functions for multiplets with unresolved structure are presented in [30].

Table 1. Values of the absorption function of a single line [9].

$\chi_{0,lu}L$	0.1	0.2	0.4	0.6	0.8	1.0	2.0	4.0
A_L	0.066	0.130	0.238	0.329	0.404	0.469	0.673	0.806
A'_L	0.049	0.090	0.163	0.225	0.278	0.319	0.445	0.527
A_L^0	0.095	0.181	0.330	0.451	0.551	0.632	0.865	0.982

The advantage of line absorption over absorption in a continuum is mainly due to two reasons. First, as mentioned above in the discussion of Eqn (15), the absorption measurement sensitivity in a continuum decreases with a decrease in the ratio of the spectral width of the spectrometer slit $\Delta\nu$ to the spectral width of the absorption line $\Delta\nu_{lu}$, and the reduction in $\Delta\nu$ decreases the aperture ratio. In the absorption of light with a line spectrum, a spectral instrument with a high aperture ratio or a filter with large $\Delta\nu$ sufficient to select the required

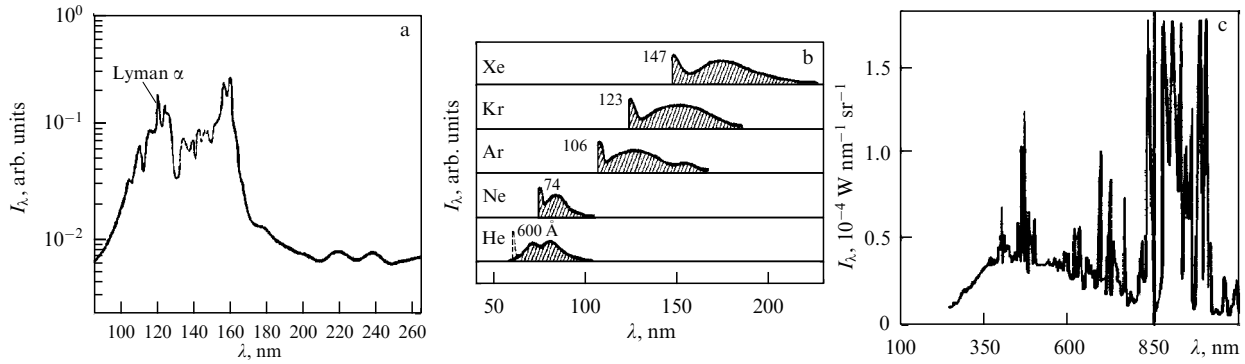

Figure 2. Spectra of plasma sources of continuous spectra: (a) hydrogen lamp, (b) continua of inert gases in discharge lamps, (c) continuum and lines in the spectrum of a high-pressure Xe lamp.

spectral region can be used. Second, the radiation from sources of the line spectrum has, as a rule, higher spectral density. The advantages of a broadband source are determined by the possibilities of measuring the absorption at many lines of transitions in different particles.

2.2.3 Broadband light sources. Such sources are used for illumination in everyday life and engineering, but a number of them have been developed especially for spectroscopy.

A. Thermal and plasma sources. *Incandescent* and *gas-discharge lamps* are sources with the radiator inside a transparent shell. In incandescent lamps of the visible region, the spectrum is often close to that of a black or grey body. The difference is usually taken into account by the color temperature parameter T_c, equal to the temperature of a black body, at which the ratio of radiation intensities and wavelengths λ_1 and λ_2 is the same as in the thermal Planck spectrum. It is accepted to use wavelengths of $\lambda_1 = 655$ nm and $\lambda_2 = 470$ nm. To approach the black body model with $T_c \approx T$ more closely, special configurations of heating elements made of heat-resistant materials with developed roughness and porosity of the surface are used [34].

The corresponding spectra are characterized by temperatures $T \leqslant 3000$ K. An exception is halogen-filled tungsten lamps, where temperatures can be higher. Among open heat sources, Chernin graphite sources [34] used in plasma spectroscopy should be noted, which have a spectrum close to thermal at a temperature of ~ 2500 K in the visible and IR ranges due to the screening of the central heating element.

In *gas-discharge lamps*, the deviations from a thermal spectrum are greater and the concept of T_c is conventional, although the contribution of continuous spectra can be significant, too. These nonequilibrium continua are present in the visible, UV, and VUV regions [40–42] and, along with the lines, are used for quantitative plasma spectroscopy by atomic and molecular transitions involving ground electronic states. Figure 2a shows the continuous spectrum of a hydrogen lamp, and Fig. 2b shows continuous spectra of gas-discharge lamps with inert gas filling. The spectra vary when changing the filling. Convenient designs are those in which the variation is achieved without loss of discharge stability.

Among gas-discharge lamps, hydrogen lamps with xenon filling at a high pressure of 10–20 atm provide the highest radiation power of 50–500 W. Figure 2c shows a typical spectral density distribution for an Xe lamp in W sr^{-1} nm^{-1}. A large number of spectral lines are observed, but a continuum with the maximum near 500–550 nm can also be selected at $T_c \sim 5000$ K.

Among other sources intended for plasma spectroscopy, we can mention various versions of lamps emitting in the VUV region, with discharges supported by miniature hollow cathodes (MHCs) [43, 44]. Instead of a hydrogen lamp, a deuterium lamp is often used, since its intensity is nearly twice as high and the spectrum is almost the same.

Gas-discharge sources without a shell are called *open* sources. The most known are arch discharges, which have been used in emission spectral analysis. In modern versions, these are mainly plasmatrons with magnetic-vortex stabilization and a spectrum close to the Planck one at temperatures of $\sim (3-4) \times 10^3$ K [41]. To study the composition of nonequilibrium plasma with high intrinsic emission, high-brightness pulsed discharges are used as external sources. A spectrum close to equilibrium at a temperature up to 4×10^4 K is produced by sources with spatially restricted discharges in narrow capillaries with a partially evaporating wall [45] and on a ferrite surface [46], as well as by a laser spark (LLDS) [47].

B. Light-emitting diodes. Under the electric current pumping of direct gap semiconductor diode structures (light-emitting diodes, LEDs) made of materials belonging to the $A^{III}B^{V}$, $A^{II}B^{VI}$ groups, recombination radiation is generated in the range of 180–2000 nm with varying band centers and characteristic diode powers. Due to the spectral power, it is more profitable for spectroscopy to use, from existing ones, diodes that emit bands with a nearly Gaussian shape. Their half-maximum width is $\sim 20-30$ nm and the power is up to 3 W in the range from 400 to 800 nm and 0.5–5 mW in the range from 280 to 350 nm. Figure 3 shows the relative spectral densities for an LED (340 mW, 455 nm), Xe

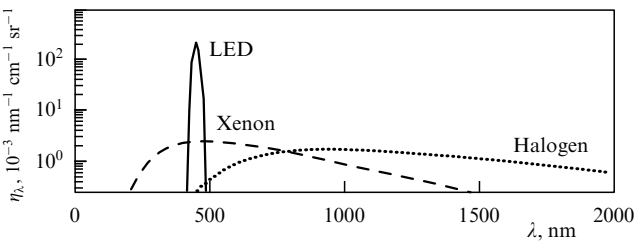

Figure 3. Relative spectral densities of radiation power per unit radiator area for unit power radiated into a unit solid angle. Gas-discharge Xe lamp Osram 450 W/2 XBO, LED Luxeon LXHL-LR3C (3 W), and tungsten halogen lamp (20 W, magnified 10 times).

lamp continuum (450 W, 6000 K), and tungsten incandescent lamp filled with halogen (20 W, 3000 K) [48].

With a large difference between the total power and efficiency, the spectral density of LED radiation multiply exceeds that for lamps due to the smaller thermal scattering and spectral width. At present, LEDs are being developed, including those intended for spectroscopy, with extended ranges and uniform intensity distribution in the range of 650–1050 nm (OSRAM SFH 4737). In comparison with gas discharge sources, LEDs possess a number of advantages. They are compact energy-efficient sources with a long service life for autonomous operation in optical systems. The radiation indicatrix is well described by the Lambert–Malus law $\sim \cos^2\theta$, where θ is the angle between the distribution axis and the normal to the emitting surface. The radiation is well collimated and can be power modulated by the pump current with a frequency of up to $\sim 10^6$ Hz. This practically removes the problem of the effect of intrinsic emission of the plasma studied upon the locked-in detection, including for a number of nonstationary objects. The drawbacks of LEDs include the following. To operate with plasma absorption spectra in an interval wider that 20 nm, a set of diodes is required. Reliable LEDs working in the UV and VUV regions (< 250 nm) are not yet available. In the emission spectra of a number of LEDs, structures associated with interference effects in them can be observed [48].

C. Synchrotron radiation. The bremsstrahlung of relativistic electrons accelerated in synchrotrons has a spectrum close to a high-brightness equilibrium spectrum with the maximum position depending on the energy of the electrons. At acceleration energies characteristic of synchrotrons, it lies in the UV, VUV, and X-ray regions. For example, at 680 MeV (S-60, DEZI), the effective temperature is about 100 kK. Since the 1960s, synchrotron radiation is widely used in the spectroscopy of solid state isolated atoms and molecules. A number of synchrotrons are either equipped with special channels for spectroscopy or especially intended for these applications [49]. In plasma spectroscopy, such a technique is also beginning to develop. Figure 4 shows an example of the atomic oxygen spectrum in a plasma jet at atmospheric pressure in the VUV region [50].

D. Laser frequency combs and continua. Since the end of the 1980s, methods of generating ultrashort pulses (USPs) with a duration of $\sim 10^{-13}-10^{-15}$ s (femtosecond lasers, FSLs; see, e.g., [51–57], etc.) have been developed. The effect of self-mode-locking in a laser cavity is used. The method has been known since the 1960s and has been used to generate nanosecond pulses, but qualitatively new facilities appeared after developing laser media with broadband gain. The interest is due to its applications, mainly in metrology, high-precision measurements, and nonlinear optics. The spectrum

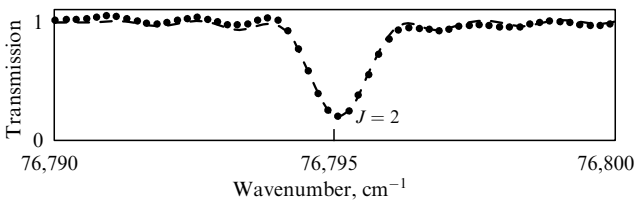

Figure 4. Spectrum of transmission of synchrotron radiation from atomic oxygen ($O(2p^4\,{}^3P_J \rightarrow 3s^3S_1^*)$) through an atmospheric-pressure plasma; a section for $J = 2$.

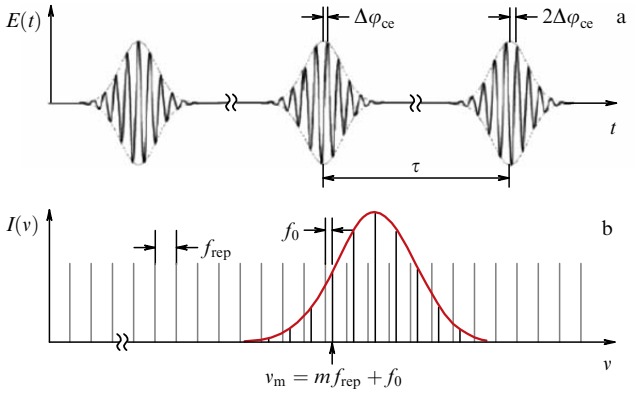

Figure 5. Comb structure in time (a) and frequency (b) domains [54, 55]. Electric field strength E (a) and intensity I (b) of light are plotted along the ordinate axes.

formation is usually explained using illustrations like that in Fig. 5 [52, 55, 57].

A train of ultrashort pulses (comb) separated by time interval τ equal to the duration of the light's round-trip in a cavity with length L is being studied (Fig. 5a). The pulses are envelopes of the oscillating carrier field. The structures of the repeated pulses are not fully identical. Due to group velocity dispersion in the cavity (reflectors, medium between them), the maxima of the carrier field oscillations in the adjacent trains have different phase shifts $\Delta\varphi_{ce}$ with respect to the envelope maxima. The radiation spectrum (Fig. 5b) is given by the Fourier transform of the square of the electric field (power) presented in Fig. 5a. The frequencies of the spectral lines ν_m are expressed in units of the pulse repetition rate $f_{rep} = 1/\tau = c/2L$ in the comb,

$$\nu_m = mf_{rep} + f_0\,, \tag{22}$$

and f_0 is the offset frequency corresponding to the phase detuning $\Delta\varphi_{ce}$, $f_0 = \Delta\varphi_{ce} f_{rep}/2\pi$, $0 < f_0 < f_{rep}$.

Equation (22) represents the direct relation between optical frequencies ν_m and frequencies f_{rep} and f_0. Depending on the FSL construction and length L, the latter frequencies vary, staying within the radio frequency range of 10^7-10^{10} Hz, and can be measured with sufficient accuracy using direct detection. The comb spectral lines have a finite width, but it can be very small. From the Fourier transform, it follows that, if the FSL generates a series of combs and their shape and amplitude reproduce during time T^*, then the line width is $\delta f = 1/T^*$. With appropriate stabilization of the lasing conditions during more than 1 s, the linewidth lies in the sub-Hz range. For absorption spectroscopy, the resolution is determined by the frequency f_{rep}. In principle, the measurement of positions ν_m in such intervals is possible using optical spectral instruments of high resolution, e.g., Fourier spectrometers [58]. To measure f_0, methods of higher accuracy have also been proposed, e.g., the method of nonlinear optical interferometry [59]. The absorption spectrum can be recorded in the entire range without scanning when using multichannel detection for a duration sufficient to provide an acceptable signal-to-noise ratio. New methods are also being developed for spectroscopy, e.g., using two sequences of combs with different f_{rep} (dual comb) and a number of others, which in the future can allow increasing the resolution to the width of a single line of the comb. A number of reviews are devoted to this issue [57, 60].

These properties are realized in a wide region of the spectrum $\Delta^* v$, which, in turn, depends on the properties of the active medium, pumping conditions, and cavity radiation losses. In the early 2000s, Ti:sapphire lasers and Er, Yb, and Tm fiber lasers in the visible and near-IR ranges of 0.8–2.5 μm were studied and brought to application [61–63]. A number of developments are commercially available. The possibilities of proceeding to the mid-IR 2.5–20 μm and far-IR 20–100 μm regions, the most interesting for molecular spectroscopy, are being studied. Direct comb generation in the far IR range is achieved by using quantum cascade lasers [64]. Thanks to the high FSL peak power of $\sim 10^{15}-10^{16}$ W, the radiation gives rise to nonlinear optical effects, which can be used to extend $\Delta^* v$, particularly upon focusing or propagation through optically bulk and fiber media. These possibilities are realized in several areas.

The most obvious one is difference frequency generation (DFG). It is possible to use combinations of lines from one comb at its high- and low-frequency wings (their frequencies can differ by more than twofold), from pairwise chosen combs using special selectors (stickers) [60], or from two independent phase-matched comb sequences [65]. At present, sources of so-called supercombs are being technically developed and are available for applications. The mechanism of their generation includes several nonlinear processes at once: stimulated Raman scattering, phase self-modulation, etc. It is realized in optical fibers having a photonic crystal type (with air channels) [53] or double-cladding structure with a special longitudinal profile [61]. The fiber length varies; at present, commercially available sources cover spectral regions from near UV to mid-IR and the range $f_{\text{rep}} \sim 10^{-1}-10^{2}$ MHz, which offers a wide choice for solving problems of quantitative absorption spectroscopy. Figure 6 presents examples of supercontinua from an Er fiber laser ranging from near UV to near IR for two models of NKT Photonics generators. Along the ordinate axis, the spectral density of mean power is plotted.

Broadband sources of light based on USP lasers are of interest for nonequilibrium plasma spectroscopy. Having a high spectral brightness of radiation, they can be used practically for all glowing objects.

Although the prospects of such pico- and femtosecond sources for spectroscopy are obvious, there is still little experience with combs in plasma absorption diagnostics. One can, for example, point to papers on the spectroscopy of laser plasma using the lines of Ar and He [66]. In Ref. [67], using absorption in the spectrum of a femtosecond comb in the range of 2.9–4.6 μm, the concentrations of polyatomic radicals in the afterglow of barrier discharge were measured. In recent paper [68], using a 0.4–2.4-μm supercontinuum of the NKT Photonics SuperK EXTREME/FIANIUM commercial laser, the concentrations of metastable argon Ar $1s_2$ and Ar $1s_4$ were measured, and gas temperatures were determined from Doppler broadening in the glowing discharge.

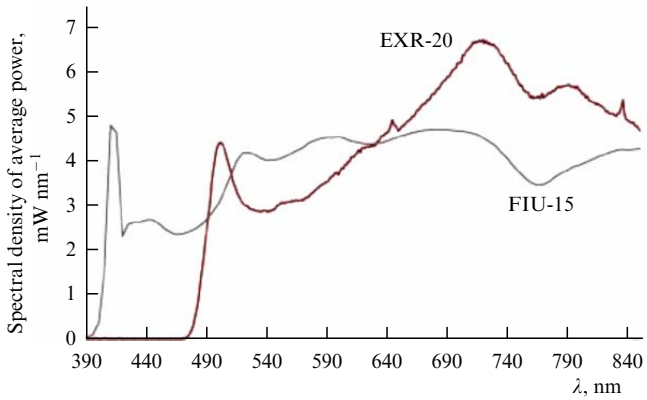

Figure 6. Supercontinua for two models of commercial USP lasers.

2.2.4 Frequency-tunable laser sources. To measure the absorption by small molecular components, laser sources of probe light are used. In a number of cases, these may be gas lasers with fixed or discretely switched frequencies. Their application provides high sensitivity to the absorption, but the list of particles is limited. For example, using a CO_2 laser with the frequency switched from one line of rotational structure to another, it is possible to determine the content of small concentrations of $^{13}CO_2$ isotopes in a discharge in a mixture of gases exhaled by a human [69]. Examples of using lasers on rotational transitions of molecules and other sources in the millimeter and terahertz ranges to measure absorption by plasma particles are practically absent, although these sources are successfully applied for measuring the parameters of plasma electrons [11]. As a rule, lasers with the frequency continuously tuned in individual ranges from the UV to mid-IR regions are used in combination with frequency conversion methods; such a technique is described in a number of monographs [11, 35, 36]. In recent years, a large number of studies have been carried out on LTP spectroscopy using semiconductor lasers, including traditional diode (compounds A^3B^5, A^2B^6) and quantum cascade ones (A^4B^6). This is due to the progress in the technology of heterostructures, their availability and flexible capabilities of digital control of operation modes of such lasers, and light signal processing (see reviews [15, 17, 22] and the results in Section 6 below).

2.2.5 Optical schemes for increasing the direct absorption sensitivity. According to law (1), an increase in the concentration sensitivity at small absorption indices χ_{lu} can be achieved by increasing the length l of the optical path in the medium, e.g., by placing the object between reflectors. Such White, Erio, Chernin, and other types of optical cuvettes [70] with an effective number of passages of $\sim 10-300$ have been also used with classical transilluminating light sources, but in recent times they are oriented at lasers with their directional radiation. Novel solutions have appeared using light coherence and resonance cuvette properties.

One such solution is *intracavity laser spectroscopy* (ICLS) [71–73]. An object is placed inside the cavity of a laser with a homogeneously broadened gain band, covering the absorption spectrum to be studied (Fig. 7a).

The plasma introduces frequency-selective losses into the laser cavity. If the absorption linewidths are small compared to the gain contour width of the laser, the distribution of intensity over the modes does not change and the absorption spectrum will manifest itself in the structure of the oscillation spectrum. The concentration of particles at the absorbing energy levels is again determined by Eqns (1)–(4), but the effective absorption length becomes $L_{\text{eff}} = ct$, where t is the lasing duration and

$$\chi_{lu} = \frac{1}{ct} \ln\left(\frac{I}{I_0}\right). \qquad (23)$$

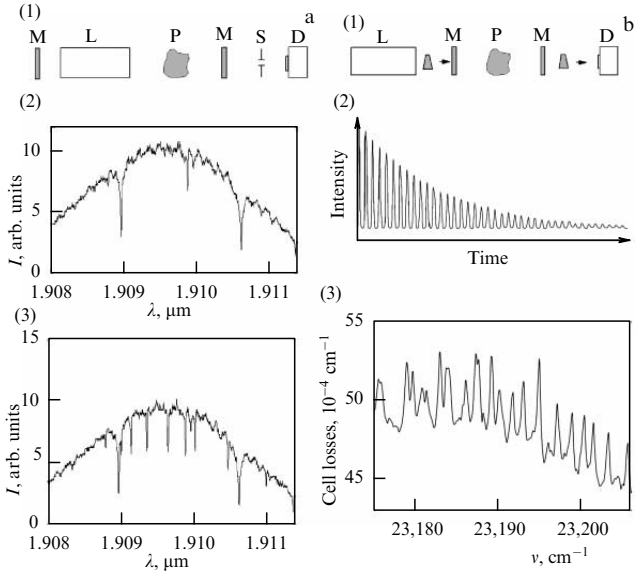

Figure 7. ICLS (a) and CRDS (b) methods. (1) Block diagrams. P — plasma, L — laser, M — mirrors of the laser (a) and the external cavity (b), S — monochromator, D — detector. (2) Characteristic view of recorded signal. (3) Fragments of absorption spectra of metastable oxygen $O_2(a^1\Delta_g - b^1\Sigma_g^+)$ (a) and $CH(X^2\Pi(v'' = 0) - A^2\Delta(v' = 0))$ (b).

The quantity I/I_0 is found as a ratio of the intensity in the lasing spectrum at the frequency of the absorption line to the intensity at a close frequency beyond the absorption line. At duration $t = 300$ μs and $I/I_0 = 1/e$, the lines with the absorption index $\chi_{lu} = 1/ct \sim 10^{-7}$ cm^{-1} are recorded and at $t = 3$ ms, those with $\chi_{lu} \sim 10^{-8}$ cm^{-1}, which corresponds to an effective absorbing layer of 1000 km. The ultimate absorption corresponds to $t \to \infty$, but the sensitivity remains finite and is determined by the spontaneous noise [72, 73]:

$$\chi_{lu,\min} = \frac{\gamma}{c\langle M\rangle}, \tag{24}$$

where γ is the reciprocal lifetime of a photon in the cavity, and $\langle M\rangle$ is the mean number of photons per mode. At typical values of $\gamma = 3 \times 10^7$ s^{-1} and $\langle M\rangle = 3 \times 10^7$, we have $\chi_{\min} \sim 3 \times 10^{-11}$ cm^{-1}. This is reached at $t \sim \langle M\rangle/\gamma \sim 1$ s, after which the development of spectral dips stops. Under real conditions, time t is limited not only by the duration of the lasing pulse but also by the lifetimes of the laser modes due to their coupling and Rayleigh scattering. The desired combination of sensitivity and time resolution in the spectral range of interest $\Delta\nu$ is achieved by choosing the laser type [72, 73].

It is also possible to increase the path length of light-matter interaction in a cell external with respect to the laser (Fig. 7b). To increase the efficiency of the radiation input, the resonance properties of an interferometer cell with high reflection R of the mirrors are used. If a laser with a narrow generated line operates in the short-pulse mode, then, if a cuvette roundtrip occurs in a time less than the interval between the pulses, a small part of the radiation passes through the mirrors and is fixed by the detector as a damping sequence of pulses. That is why the method is called cavity ringdown spectroscopy (CRDS). The presence of absorption in the medium affects the damping times that determine the absorption spectrum upon laser frequency variation. An example of the spectrum is presented in Fig. 7b. If during one passage through the cell the loss of pulse energy at the mirrors is $1 - R$, the loss due to absorption is $A(1 - \exp(-\chi_{lu}ct))$, the mirrors are identical, $A \ll 1$, and $1 - R \ll 1$, then the pulse decays exponentially as

$$I(t) = I_0 \exp\left(-\frac{2(1 - R + A)t}{\tau_r}\right), \tag{25}$$

where $\tau_r = 2L/c$ is the roundtrip time, L is the cell length, A is the absorption per passage. The decay is determined by the envelope of a series of pulses from the detector. For an empty cuvette $A = 0$ and decay time $\tau_0 = L/(c(1 - R))$, in the presence of absorption, $\tau = L/(c(1 - R + A))$ and the minimal measurable absorption index equals

$$(\chi_{lu})_{\min} = \frac{1 - R}{L}\left(\frac{\tau_0 - \tau}{\tau_0}\right)_{\min}. \tag{26}$$

The spatial resolution in the direction normal to the cavity axis is limited by the Gaussian mode waist diameter W_0,

$$W_0^2 = \frac{L\lambda}{\pi}\sqrt{\frac{g_1 g_2(1 - g_1 g_2)}{(g_1 + g_2 - 2g_1 g_2)^2}}, \tag{27}$$

where $g_{1,2} = 1 - L/r_{1,2}$ is the confocal parameter, and $r_{1,2}$ are the curvature radii of the mirrors. At damping times of $10^{-6} - 10^{-7}$ s, getting an accuracy of 1% in their measurement is not a serious problem, and at $\chi_{lu} \sim 10^{-7} - 10^{-9}$ cm^{-1}, the absorption can be registered at a plasma length of 10–100 cm.

The CRDS method is also used with CW lasers (CW-CRDS) in cavity-enhanced absorption spectroscopy (CEAS), also referred to as integrated cavity output spectroscopy (ICOS). In this case, the radiation of a CW laser with a tunable frequency sequentially finds itself in resonance with modes of a cavity with low matching losses and passes through it many times. To provide a spectral resolution of ICOS better than the spacing between the longitudinal modes, the radiation entering into the cavity is shifted from the optical axis (off-axis ICOS). To involve the transverse modes and to reduce the spacing between them, techniques of laser-cell feedback and other approaches have been developed [15, 74, 75]. The stability of diode lasers allows measuring the absorption at a level of $\chi_{lu} \sim 10^{-9} - 10^{-11}$ cm^{-1}.

When using the ICOS technique with an external cell with high-reflection mirrors, a limitation on the spectrum recording rate arises. The time of recording should not be less than the photon lifetime in the cavity; otherwise, the spectrum will be distorted. So, in Ref. [76], it was noted that substantial distortions of the Doppler contour of the line and the integral absorption by H_2O molecules near the region of 1.4 μm in a cell with mirrors with $R = 99.98\%$ occur at the rate of $\sim 10^3$ cm^{-1} s^{-1} of tuning the diode laser frequency.

3. Absorption measurements by indirect evidence

Direct methods of absorption are based on ratio (1) of light intensities incident on the object and transmitted through it. If the optical transition is not saturated and the intrinsic emission of the object can be ignored, the result of measuring the population of the lower energy level does not depend on the equilibrium conditions in the absorbing medium. Another very important advantage of these methods is that the absolute values of the density of states can be obtained from relative measurements.

Methods in which the absorbed energy of light is determined from a change in a certain parameter of the object, the relation between the quantities being provided by the model and the absolute values by calibration, can serve as alternatives. Such methods are used to achieve higher sensitivity and locality if allowed by the nature of the object and measurement conditions.

One more group of methods is based on the fundamental relation between absorption and refraction in the structure of medium permittivity. In spectroscopy, it manifests itself in the polarization characteristics of radiation at frequencies of absorbing transitions in the medium when removing the degeneracy of states in the magnetic quantum number in an external field.

3.1 Induced fluorescence

When light is absorbed by a particle at transition $1-2$, additional population of the upper energy level 2 occurs, and the intensity of spontaneous emission at transitions $2-1$ (resonance fluorescence) or $2-3$, where 3 is a foreign level (nonresonance fluorescence), grows (Fig. 8). At present, lasers are used as transilluminating sources, and the analysis of laser-induced fluorescence (LIF) requires considering coherent effects and induced transitions [11, 77]. If the laser light intensity is sufficient to saturate the transition $1-2-1$, then the LIF intensity is proportional to the Einstein coefficient $I_f \sim A_{21}$, which ensures a high sensitivity of detecting particles in state 1. The physical meaning of such a result is that, during the detection time determined by the detector bandwidth, cycles $1-2-1$ repeat many times.

When measuring absorption by LIF spectra, it is necessary to keep in mind that, besides the excitation of level 2 by the light, other processes also contribute to the balance of its population. The proportion of the contributions depends on the conditions. Frequently, collisional quenching processes are of importance. For some pairs of particles, the cross sections of quenching collisions are known from independent measurements; however, this does not remove the problem completely because of the complexity of the plasma chemical composition, especially in the presence of molecules. Two methods of considering or excluding the quenching contribution are known. Both are based on choosing state 2 strongly coupled to the predissociation (D) or ionization (I) continuous spectrum (see Fig. 8). The time of a transition from the bound state to that of the continuum, as a rule, is less than the time $\tau_q = Q_q^{-1}$ of collisional quenching due to the thermal motion of the particles under a wide enough range of conditions. The realization of such opportunity in the case of spontaneous transition from a bound state to a state of continuous spectrum is studied for the OH radical, which plays an important role in many plasmochemical reactions [78]. This radical experiences predissociation in the state $OH(A^2\Sigma, v' = 3)$ because of interaction with the repulsive state $OH(^4\Sigma^-)$. Under typical conditions in a flame at atmospheric pressure, for excitation at a wavelength of 248 nm, $OH(X^2\Pi, v'' = 0 \rightarrow A^2\Sigma, v' = 3)$ $A_{21} \approx 10^6$ s^{-1}, $Q_{21} \approx 10^9$ s^{-1}, $Q_{2s} \approx 10^{10}$ s^{-1}. Analogous schemes are applicable to H_2O and O_2 [79]. An alternative possibility of introducing controlled losses of particles in the excited state 2 is related to exploiting the processes $2 \rightarrow \mathbf{i}, \mathbf{d}$ (photoionization, photodissociation). It is possible to use an additional laser with the frequency of the lighting radiation off resonance $1 \rightarrow 2$ sufficient to transfer the particles from state 2 to the continuum. The powers of both lasers are controlled independently, which allows separating their contributions to the $2 \rightarrow \mathbf{i}$ process [80]. Of course, it should be kept in mind that the cost of this control is a decrease in LIF intensity.

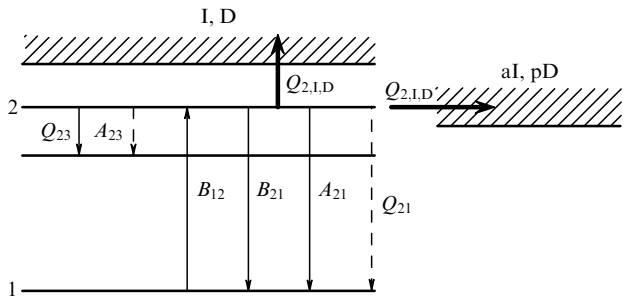

Figure 8. Excitation of fluorescence under the conditions of the upper level coupled to the continuous spectrum (I — ionization, aI — autoionisation, D — dissociation, pD — predissociation).

LIF methods are used to detect a number of heavy atoms (U, Pb), two- and three-atomic radicals (OH, CN, CH, CF, NO, C_3, CF_2), metastable molecules ($C_2(a^3\Pi)$, $N_2(A^3\Pi)$), ion N_2^+, etc. in plasma (see Section 6 below). The advantages of LIF are the locality of measurements when observing the glow at an angle to the laser beam and high sensitivity. To measure absolute concentrations, calibration is required, mainly using the direct absorption method.

The limitations of the traditional 'linear' LIF are due to the fact that the absorption spectra of many particles in the ground electronic states lie in the UV and VUV regions. First and foremost, this concerns atoms, since for molecules the methods of absorption and scattering by vibrational-rotational transitions of the ground electronic states can be used. The capabilities of LIF extend when inducing it by two-photon absorption (TALIF). The necessary frequency of transilluminating radiation is chosen, as a rule, by mixing fixed and tunable frequencies of lasers followed by frequency doubling. An additional advantage is the possibility of using the optical actinometry principle, according to which, in this case, the absolute concentration of the particles of interest X is found by comparing the fluorescence intensities of two particles if the concentration of one of them A is known, as well as the ratio $\sigma_{lu}^A/\sigma_{lu}^X$ of the two-photon absorption cross sections. The fluorescence intensities in this case nonlinearly depend on the intensity I_l of the inducing radiation: $I_f \sim \sigma_{lu}^{X,A} I_l^2$. Atoms of inert gases play the role of an actinometer A, the plasma-forming gas specifying their concentrations, and the frequencies of fluorescence excitation are close to the excitation frequencies for particles X. The ratio of cross sections can be determined in a similar experiment, but with the object in the equilibrium state, when the concentrations of X are also known. Such combinations with the participation of hydrogen, deuterium, nitrogen, krypton, and xenon atoms are shown in Fig. 9 [81–83]. The ratios of cross sections of fluorescence excitation in actinometric pairs are [82, 83]

$$\frac{\sigma_u^{Kr}(5p'[3/2]_2)}{\sigma_u^{H,D}(3^2D_J)} = 0.62\,; \quad \frac{\sigma_u^{Kr}(5p'[3/2]_2)}{\sigma_u^{N}(3^2D_J)} = 0.67\,;$$

$$\frac{\sigma_u^{Xe}(5p'[3/2]_2)}{\sigma_u^{O}(3p^3P_J)} = 0.36\,; \quad \frac{\sigma_u^{Xe}(7f[3/2]_2)}{\sigma_u^{H,D}(3^2D_J)} = 0.024\,.$$

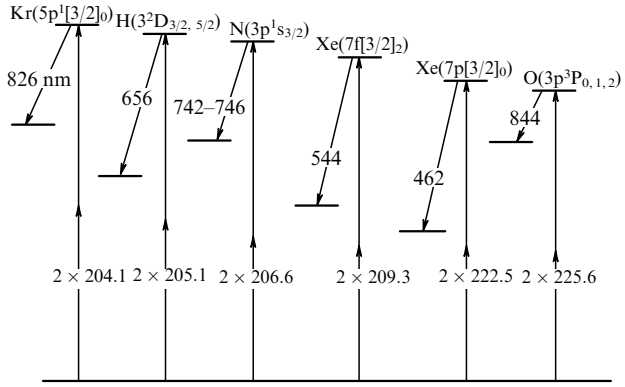

Figure 9. Schematic diagrams of two-photon excitation of Kr, H, N, and Xe atoms. Wavelengths are given in nanometers.

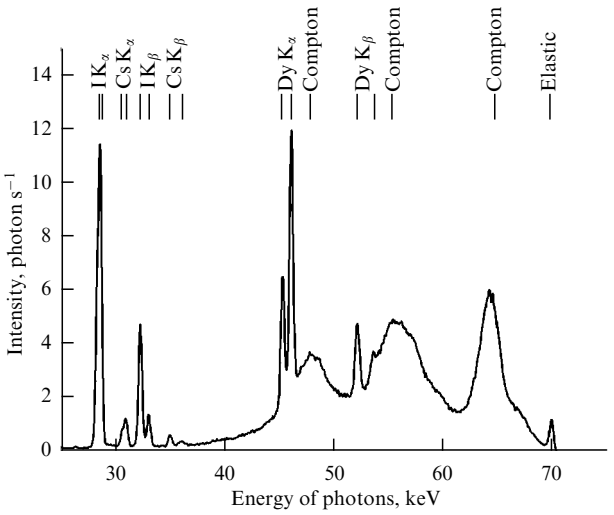

Figure 10. XRIF spectrum of a halogen lamp.

This technique has been under development, starting with Refs [27, 81, 82]; examples of measurements are presented in Section 6.

In principle, sources of hard radiation can be used for single-photon excitation of fluorescence. Methods of analysis using X-ray tubes are known in application to the diagnostics of condensed matter. Using such sources for plasma spectroscopy is, however, problematic because of the substantially smaller density of particles, small intensity of radiation (especially in combination with collimating optics), and the presence of intrinsic glow, especially if the detection is performed using scintillators. In the X-ray range, single-photon fluorescence (XRIF) may be induced by synchrotron radiation (SIF). In its properties, it is close to laser radiation, has a high intensity, and can be frequency-tuned and collimated. In Ref. [84], synchrotron radiation with photon energies of 40–100 keV, a wavelength of 0.3–0.12 Å, a monochromaticity of $\Delta\lambda/\lambda \sim 10^{-3}$, a divergence of $\sim 10^{-5}$ rad, and a beam cross section of 1×1 mm^2 was used. The XRIF spectra excited with such 'hard' radiation correspond to atomic transitions with the participation of inner electronic shells. The spatial distribution of elements in a high-brightness halogen lamp plasma was studied ($T \sim 6000$ K, pressure $P \sim 10$ atm). Figure 10 shows the XRIF spectrum [84] in the central zone of a lamp excited by photons with an energy of 68.9 keV. These are narrow characteristic lines of iodine, cesium, and dysprosium. The background is formed by the glow due to the Compton effect and elastic scattering. Broad Compton lines with the maxima at 47.6 keV, 54.8 keV, and 84.6 keV are in this case due to the scattering in the lamp shell with its specific geometry and orientation with respect to the observation direction. The XRIF technique allows studying the plasma behind shell walls not transparent in optical schemes. As in the case of using synchrotron radiation for absorption measurements, studies of SIF are still scanty; objects of study are placed in spectroscopic channels of synchrotrons and a specific measurement technique and intensity calibration are used.

3.2 Changes in the plasma ionization balance upon light absorption

The absorption of light transfers the particle to a state of smaller ionization potential as a result of a number of processes beyond absorption, affecting the charge balance and conductance of the plasma, which can be used in plasma spectroscopy.

3.2.1 Optogalvanic effect. The change in the current or scattered power in an external electric circuit correlated with the absorption spectrum under the transillumination of plasma with a tunable-frequency light has been recorded [85, 86]. The plasma itself becomes a detector of light absorbed by it. For stationary plasma with a low level of electric noises, the sensitivity to absorption may be higher than in direct absorption measurements. This is used in the elemental analysis, when the equilibrium plasma serves as an atomizer, and, using calibrations, it is possible to measure small concentrations of particles. Under nonequilibrium conditions, depending on the object, the relationship between the absorption and the response in the discharge circuit may be rather complex. Figure 11 shows a comparison of the spectra of absorption by a discharge in an He–Ne mixture obtained by measuring the power P of radiation transmitted through the plasma (A) and using the signal ΔV from a measuring resistor in the discharge circuit (B) [85]. In both cases, the line frequencies coincide, but, while in the optical spectrum all lines correspond to the absorption of light, in the optogalvanic (OG) spectrum, ΔV has different signs for different lines.

These relationships are best studied in the case of a positive glow discharge column. At small absorptions, the current change Δi in the discharge circuit is proportional to the change in the field strength ΔE in the positive column, $\Delta i \sim -\Delta E$, for a normal and abnormal discharge. If in a long tube the contribution of the near-electrode zones to the voltage-current characteristic is small, then quantitative changes are possible. In Ref. [69], the concentrations of CO_2

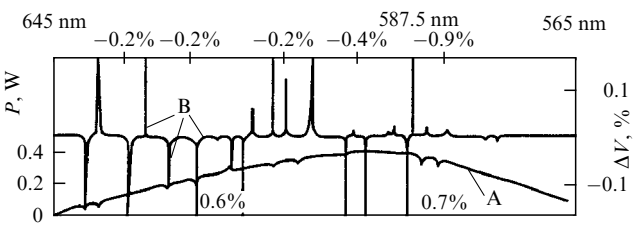

Figure 11. Absorption spectra of a discharge in an He–Ne mixture. A — recording changes in the power of the tuned laser, B — OG detection [85].

isotopes are measured in the CO_2-N_2 discharge by the absorption on CO_2 laser lines; their ratio, $^{13}CO_2/^{12}CO_2$, is determined with an accuracy better than 0.05%, thus demonstrating an important analytic technique for medical tests of human exhalation.

Note that quantitative OG measurements in a gas discharge plasma independent of the optical scheme (linear and nonlinear absorption, Doppler-free and polarization spectroscopy, etc. [85, 86]) are not local, since they are based on the response of the discharge as a whole. The localization is possible using additional electric probes.

3.2.2 Absorption of light by negative ions. A number of atoms and molecules can attach free electrons $X + e \rightarrow X^- + h\nu$ (photoattachment) with the emission of a continuum; the strength of the arising chemical bonds (affinity) of negative ions X^- is typically 0.5–3.5 eV. Under a wide range of conditions, thermal motion does not break these bonds, and the lifetime of X^- ions in the plasma is determined by various elementary processes [87]. They include the light absorption $X^- + h\nu \rightarrow X + e$ process (photodetachment). Typical values of photodetachment cross sections $\sigma_d \sim 10^{-18}-10^{-16}$ cm^2 are observed in the spectral range from near UV to near IR [11].

In addition to the methods of mass spectrometry, the concentrations of X^- ions can be determined by light absorption. At their density of $\sim 10^{10}$ cm^{-3}, comparable to the density of electrons, the absorption index for bound-free transitions is $\chi_{lu} \sim 10^{-8}-10^{-6}$ cm^{-1}. This can be achieved by direct absorption methods using lasers (see Section 2.2.5) when diagnosing plasma under conditions in the laboratory, industrial plasma chemical reactors, and ion generators for injection into the plasma of magnetic traps. Long optical paths are characteristic of Earth's ionosphere and extraterrestrial plasma. For example, studies of conditions in the solar photosphere with its extension of $\sim 3 \times 10^8$ cm have shown that the radiation balance in it is largely determined by absorption in the continuum of bound-free transitions of H^- ions [88].

The absorption of light by the X^- ion is accompanied by the release of an electron and a change in the local balance of ionization in the plasma. For a known light intensity I, the extra concentration of electrons Δn_e can be related to the concentration of ions as

$$\Delta n_e(t) + X^-(t) = X_0^-(t)\,, \tag{28}$$

where X_0^- is the density of ions unperturbed by the radiation. For light with frequency ν,

$$\Delta n_e(t) = X_0^- \left[1 - \exp\left(-\frac{\sigma_a(\nu)}{h\nu}\int I(\nu)\,dt\right)\right]. \tag{29}$$

A detailed balancing condition relates the cross sections of photoattachment σ_a and photodetachment σ_d:

$$\sigma_a = \frac{g_i}{g_a}\frac{k^2}{q^2}\,\sigma_d\,, \tag{30}$$

where g_a and g_i are the atom and ion statistical weights, $k = 2\pi\nu/c$ is the photon wavenumber, q is the electron wavenumber, $hq/2\pi = (2mE_e)^{1/2}$, $g_i = (2L^- + 1)(2S^- + 1)$, $g_a = (2L^a + 1)(2S^a + 1)$, L^- and S^- are the orbital and spin angular momentum quantum numbers for the X^- ion, and L^a and S^a are those for the atom.

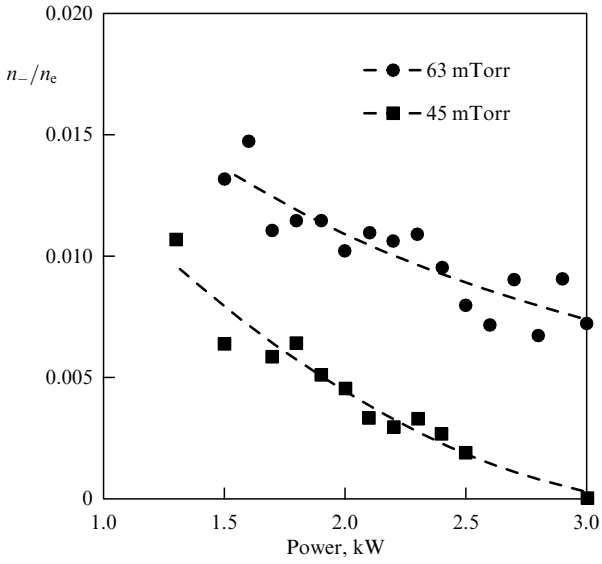

Figure 12. Ratio of concentration of H^- ions to the concentration of electrons 40 μs after terminating a HF discharge, depending on its power [89].

The averaged values of Δn_e can be measured, for instance, by the OG method; the local values can be measured with a Langmuir probe. Figure 12 shows an example of measuring the ratio of concentration of H^- ions to that of electrons n_e in the afterglow of a 13.56-MHz discharge in hydrogen transilluminated with 680-nm, 40-mJ cm^{-2}, 8-ns laser radiation pulses. The quantities Δn_e and n_e were measured by the probe method.

It should be noted that the spectra of absorption (photodetachment) cross sections for negative ions have the form of rather wide bands, and this requires attention with respect to the selectivity of determining the concentration of ions of different sorts. Practically, such a method is applied to those objects in whose plasma the presence of mainly negative ions of one sort is expected. The use of tunable-frequency lasers also allows identifying particles by the detachment thresholds and specific features of the cross section forms.

The good accuracy and sensitivity of methods based on observing violations of ionization balance are achieved for conditions under which the plasma is stable and the measured deviations Δn_e are not masked by the natural fluctuations of n_e. Such conditions are met by a positive column of a glow discharge, plasma afterglow, and flames, for which models of optogalvanic effect are being developed [85, 86]. Using the modulation of transilluminating radiation also facilitates a considerable increase in sensitivity.

3.2.3 Scattering of microwave radiation during resonance photoionization. To measure excess electron density upon absorption of light by neutral particles, the technique of Thomson scattering can also be used [90]. It is based on the REMPI laser spectroscopy method, as in the control of LIF quenching (see Section 3.1), when a particle absorbs light in an excited state with a transition to the continuum. The peculiarity is that the same light causes both multiphoton excitation and ionization (Fig. 13a). If an intermediate virtual state of the particle coincides with or is close to a real state, the cross section for the multiphoton absorption from the ground state and the ionization sharply increases (resonant enhanced

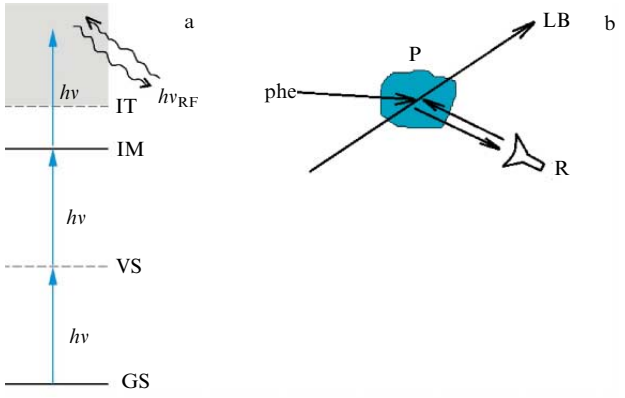

Figure 13. Diagrams of transitions upon multiphoton ionization (a) and observations of Radar-REMPI microwave back scattering; phe — region of photoelectrons (b). LB — laser beam.

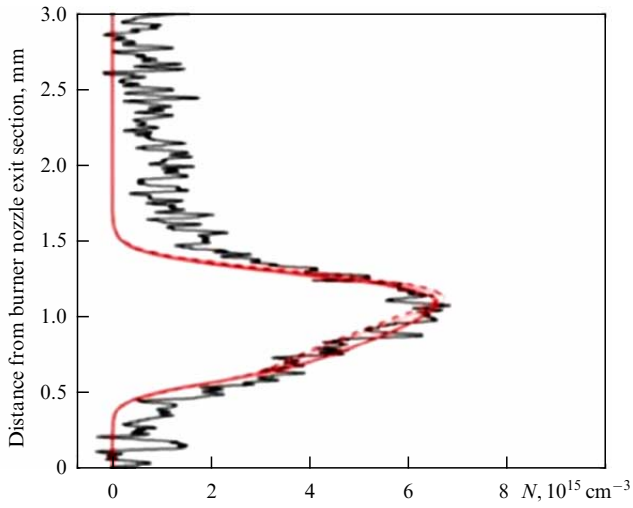

Figure 14. Concentrations of methyl radicals in the space of a burner flame. Smooth line is a result of calculations under equilibrium conditions.

multiphoton ionization, REMPI). If the ionization is detected by Thomson scattering, the method is called Radar-REMPI. To increase the sensitivity, the scattering is observed in the microwave RF range, usually $\sim 10^{10}$ Hz. Figure 13b illustrates a setup in which the same horn antenna R is used both to form the transilluminating radiation and to receive the backscattered RF radiation.

The advantage of the method, like that of other nonlinear optical methods, is the locality of the particle concentration measurements. It is easily achieved by even moderate focusing of transilluminating laser light of intensity I, since the scattered intensity is $I_{RF} \sim NI^m$, where m is the number of photons participating in the excitation-ionization. To measure the absolute concentrations of particles, the same scheme can be used as for fluorescence methods; to calibrate the scattering signal, a suitable actinometric pair consisting of the particle to be determined and an inert gas atom is chosen (see Section 3.1, Fig. 9). Using this method, the concentrations of atoms and molecules O, O_2, NO, CO, CH_3, polyatomic hydrocarbons, and ions are measured. Figure 14 shows an example of measured concentrations of CH_3 methyl radicals in a CH_4/air flame at atmospheric pressure at different distances from the exit section of a burner nozzle [91]. Also

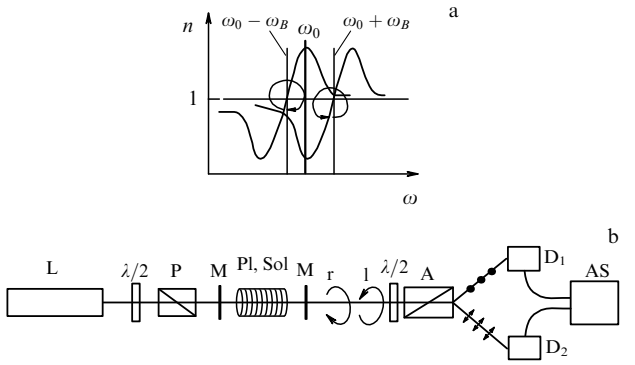

Figure 15. Measurements of polarization rotation and concentrations of paramagnetic particles. (a) Splitting of dispersion curves of refraction in magnetic field B. (b) Schematic diagram of measurements. Pl — plasma inside solenoid Sol and resonator with mirrors M; L — laser; $\lambda/2$ — plates; P and A — polarizer and analyzer; $D_{1,2}$ — detectors; AS — electronics.

shown is the result of a thermodynamic calculation of the methyl concentration. Good agreement between the calculation and measurement results shows that the flame plasma is close to equilibrium.

3.2.4 Magnetic rotation of the polarization plane. Some particles in certain states possess intrinsic magnetic moments. In the ground state, they constitute a rather wide class of particles with the paramagnetic property, manifesting itself in the induced anisotropy of the medium in an external magnetic field. They often possess high reactivity, which determines the importance of their monitoring.

The application of a field removes the degeneracy with respect to the magnetic quantum numbers m and splits the transition. For absorption, this is called the inverse Zeeman effect [92]. When light propagates along the lines of an external magnetic field, according to the selection rule $\Delta m = \pm 1$, the components have right-hand and left-hand circular polarizations at frequencies $\omega_0 \pm \omega_B$, where ω_0 is the zero-field transition frequency, and ω_B is splitting proportional to the magnetic field induction B. The right-hand polarization corresponds to $\Delta m = +1$, $\omega_R = \omega_0 - \omega_B$, the left one, to $\Delta m = -1$, $\omega_L = \omega_0 + \omega_B$. They have different refractive indices n_R and n_L (birefringence and, respectively, different phase incursions during propagation) and absorption indices χ_{lu} (dichroism). The phase difference of waves with right- and left-hand polarizations is $\beta = 2\pi\Delta n L_B/\lambda$, $\Delta n = n_R - n_L$, $\lambda_0 = 2\pi c/\omega_0$, where L_B is the length of the medium in the field. According to the Kramers–Kronig rule, in dispersive media, the values of refraction n and absorption χ_{lu} in the complex refractive index $\tilde{n}(\omega) = n(\omega) - i\kappa_{lu}(\omega)$ are rigidly related, regardless of the dispersion mechanism [93–95]. A spitting of dispersion dependences occurs (Fig. 15a). If linearly polarized radiation at the absorption frequency is directed along the field lines, then, due to adding fields of the incident wave components with different circulations, amplitudes, and phases, at the medium output the plane of its polarization is rotated relative to the initial one. This effect is the Faraday rotation, which grounds the Faraday rotation spectroscopy (FRS) method. The angle of rotation is $\theta = VBL_BN$, N is the density of particles in a homogeneous medium, and V is the Verdet constant for the considered sort of particles.

In a rarified gas and plasma, the typical values of V are $\sim 10^{-9} - 10^{-10}$ G^{-1} cm^{-1} atm^{-1} and the angles θ are small. To

measure them, optical systems are used with long optical paths $L_{B,\mathrm{eff}}$, just as for direct measurements of the small absorptions (e.g., CRDS) discussed in Section 2.2.5, supplemented with polarization elements [96]. Figure 15b shows an FR-CRDS setup, in which the plasma Pl with the applied magnetic field with induction **B** in solenoid Sol is placed in an optical resonator to increase the optical path length L_B. $\lambda/2$ plates are used to match the polarization of the pulsed laser radiation with the polarizer and to equalize the intensities of the beams with different polarizations at the analyzer output in the absence of absorption. This allows increasing the sensitivity to the polarization rotation measurement upon simultaneous detection of two beams with zero initial detuning. Decay times τ_s and τ_p for signals with s and p polarizations at the analyzer output are measured. The polarizer and analyzer are turned round by an angle of $\pi/2 \pm \varphi$ with respect to each other, where $\varphi \ll 1$.

In a number of papers [97, 98], relationships are derived between data on the Faraday rotation θ obtained from the FR-CRDS measurements and the concentrations of particles determined from the absorption index $\bar{\kappa}_{lu}$ by means of the BBL law (1),

$$\vartheta = \frac{L_B \cos(2\varphi)}{2c}\left(\frac{1}{\tau_\mathrm{s}} - \frac{1}{\tau_\mathrm{p}}\right), \tag{31}$$

$$\bar{\kappa}_{lu} = \frac{1}{2c}\left(\frac{1}{\tau_\mathrm{p}} + \frac{1}{\tau_\mathrm{s}} - \frac{2}{\tau_0}\right). \tag{32}$$

Here, $\bar{\kappa}_{lu} = (\kappa_{lu,\mathrm{R}} + \kappa_{lu,\mathrm{L}})/2$ is the mean value of the absorption index for waves with right- and left-hand circulation in a medium with a magnetic field, and $\tau_0 = -L/(c \ln R)$ is the decay time of light in an empty cavity formed by two mirrors with intensity reflections R. Equations (31) and (32) have a number of applicability limitations. The magnetic field is considered small enough so that the Zeeman splitting $\omega_B \ll \Delta\omega_L, \Delta\omega_C$, i.e., is less than the absorption linewidth of the particles and the transmission bandwidth of the resonator. This, in turn, imposes a condition on the smallness of the measured Faraday rotation angles, which provides a reasonable dynamic range of times sufficient for decay measurements. So, in Ref. [98], when measuring the concentration of HO_2 molecules at a transition of 1506 nm in a cavity with $R = 0.99998$ mirrors at decay times $\tau_{\mathrm{s,p}} \approx 150$ μs, the resonator length with the medium being $L = 86$ cm, the measured values were $\theta < 10^{-6}$ rad. On the other hand, the technique is oriented just at the measurement of small Faraday rotation angles and concentrations of particles. When using this setup to measure the concentration of HO_2 molecules in a plasma jet in humid inert gases expanding into the atmosphere, the minimum values of the polarization plane rotation amounted to 0.62×10^{-9} rad $\mathrm{Hz}^{-1/2}$, and the HO_2 concentration, to 6.7×10^7 cm^{-3}. Under these conditions, the sensitivity of the CRDS method without polarization measurements amounted to 3.1×10^8 cm^{-3}. Among the advantages of the method are:

— high sensitivity. The advantage over other methods using an external optical resonator is due to a number of factors, first of all, the fact that s- and p-polarized light signals are recorded simultaneously and their correlation allows substantial suppression of detection noises;

— possibility of detecting paramagnetic particles without a loss of sensitivity, when their absorption spectra are masked by those of diamagnetic particles.

The difficulty lies in the fact that even a weak magnetic field ($\sim 10^2$ G) applied to a discharge can affect its properties. This issue has not yet been studied enough, and, at present, the method is used to analyze flames and plasma jets outside their electric discharge sources or in the analysis of plasma reaction products in samples. Probably, the method will be useful for objects with an intrinsic magnetic field, for example, in ion beam injection generators, but the issue has not been studied in detail.

4. Light scattering

Light scattering in a medium is accompanied by the appearance of new radiation in the direction at an angle to the direction of the incident light greater than the diffraction angle. It can differ from incident radiation in frequency and polarization.

4.1 Two-wave processes

At least two waves take part in the scattering process: an incident one and a scattered one. The scattering can be elastic (not changing the particle internal energy) or inelastic. When incident radiation with intensity I_l and field strength E acts on a particle, the polarization $P(\omega) = \chi(\omega)E(\omega)$ is induced in it, and new scattered radiation appears, χ being the optical susceptibility. The intensity $I_\mathrm{s} = E_\mathrm{s}^2$ of the scattered light can be expressed as $I_\mathrm{s} = I_\mathrm{l} N\sigma$, where N is the number of particles per unit transverse area of beams in the scattering zone. If the particle is unstructured or the incident light frequency does not coincide with its eigenfrequencies, the scattered intensity is proportional to the intensity of the incident light independent of the focusing conditions, and the process is linear.

4.1.1 Scattering by a bound electron. If a plane wave of polarized radiation with frequency ω_0 is incident on a particle with a bound electron in it, the cross section of scattering observed at an angle θ to the incident radiation is given by the classical relationship

$$\frac{\mathrm{d}\sigma}{\mathrm{d}\Omega} = r_0^2 \sin^2\theta \, \frac{\omega_0^4}{(\omega_\mathrm{R}^2 - \omega_0^2)^2 + \gamma^2\omega_0^2}, \tag{33}$$

where γ is the decay rate, and ω_R is the intrinsic frequency of electron oscillations. At $\omega_0 \gg \omega_\mathrm{R}$, the scattering occurs with the cross section for a free electron

$$\frac{\mathrm{d}\sigma}{\mathrm{d}\Omega} = r_0^2 \sin^2\theta, \tag{34}$$

where $r_0 = 2.8 \times 10^{-13}$ cm is the classical radius of an electron. For an electron at rest, the cross section is independent of the frequency. At $\omega_0 \approx \omega_\mathrm{R}$, resonance fluorescence arises with the classical LIF cross section

$$\frac{\mathrm{d}\sigma}{\mathrm{d}\Omega} = r_0^2 \sin^2\theta \, \frac{\omega_0^2}{\gamma^2}. \tag{35}$$

Far from the resonance, $\omega_0 < \omega_\mathrm{R}$, elastic Rayleigh scattering takes place with the dependence of the cross section on the wavelength of $\sim 1/\lambda^4$:

$$\left(\frac{\mathrm{d}\sigma}{\mathrm{d}\Omega}\right)_\mathrm{ES} = r_0^2 \sin^2\theta \left(\frac{\omega_0}{\omega_\mathrm{R}}\right)^4. \tag{36}$$

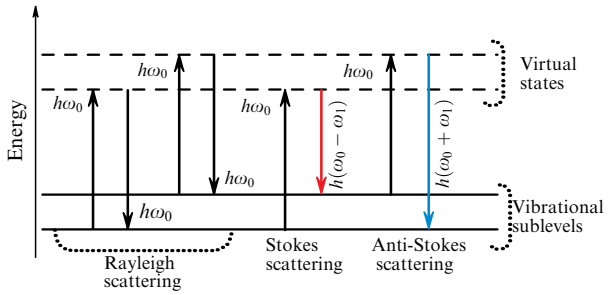

Figure 16. Spontaneous scattering by molecules. Upon coincidence of virtual energy levels with real ones, scattering becomes resonance.

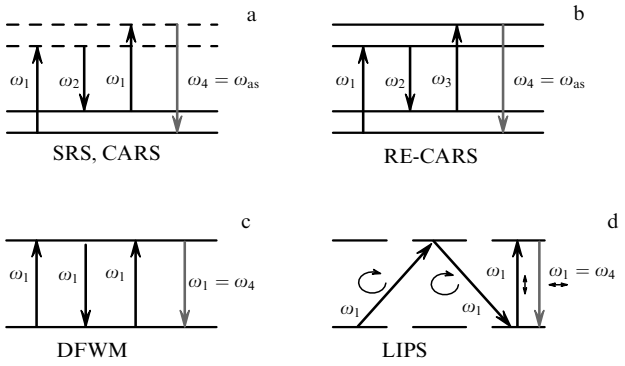

Figure 17. FWM spectroscopic diagrams. Waves with ω_4 are signal waves. (a) SRS and nonresonance CARS, in the case of CARS, $\omega_2 = \omega_s$ and corresponds to the frequency of a probe laser wave; (b) resonance RE-CARS; (c) degenerate DFWM; (d) laser-induced polarization LIPS.

Along the field vector of linearly polarized incident radiation, the scattered radiation is also linearly polarized. Except for LIF, the scattering is elastic: it does not affect the internal degrees of freedom of the scattering particles, is not selective, and is not directly used to measure their concentration (the free electron concentrations are determined by the collective scattering). However, it can be used to calibrate the LIF signal, including that under multiphoton excitation (see Section 3). The Doppler shift of the scattering line allows establishing the distribution of plasma flow velocities in space. The scattering line depolarization testifies to the presence of dust particles or clusters with a size comparable to or greater than the wavelength (Mie scattering). The lines of the narrow Q-branch of the Raman scattering can contribute to the depolarization and distortion of the Doppler shift (Cabanne profiles). For details, see, e.g., review [99].

4.1.2 Spontaneous Raman scattering. Raman scattering (RS) is photon $\hbar\omega$ inelastic scattering with a change in both the frequency and the internal energy of the particle:

$$\mathrm{M}(E_\mathrm{l}) + \hbar\omega \to \mathrm{M}(E') \to \mathrm{M}(E_\mathrm{f}) + \hbar\omega' \,. \tag{37}$$

RS is called Stokes if $\omega' = \omega_\mathrm{s} < \omega$ and anti-Stokes if $\omega' = \omega_\mathrm{as} > \omega$ (Fig. 16). According to the general rules for two-photon processes [100, 101], the initial and final states must have the same parity. In particular, these rules are followed by vibrational (within a fixed electronic state) energy levels v in a number of diatomic and polyatomic molecules. For example, for the Stokes component $\mathrm{v} \to \mathrm{v}+1$, the scattered light intensity is

$$I_\mathrm{ss} \sim N_\mathrm{v}(\mathrm{v}+1)\left(\omega - \frac{E_{\mathrm{v}+1} - E_\mathrm{v}}{\hbar}\right)^4 I_\mathrm{L} \,. \tag{38}$$

The cross sections of nonresonance RS are small, $\sigma_\mathrm{lf} \sim 10^{-30}$ cm^2 (for LIF $\sim 10^{-17}$ cm^2). If the intermediate virtual state $E^\mathrm{v} = E_\mathrm{l} + \hbar\omega$ in the scattering cycle coincides with one of the eigenstates of the particle, then the scattering intensity (38) increases and the scattering is referred to as resonance. In present-day RS spectroscopy, lasers are used for the excitation; in order to increase the sensitivity, multipass cuvettes are sometimes used (see Section 2.2.5). In studies of stationary or pulse-periodic objects, the accumulation of the scattered signal is applied [102].

4.2 Four-wave processes

Scattering can be initiated by more than one wave, or the same wave but repeatedly. The waves take part in the common process of frequency mixing, and, in the expansion of the induced polarization, several terms should be considered [103–105]:

$$P(\omega) = \chi^{(1)}(\omega)E_1(\omega_1) + \chi^{(2)}(\omega)E_1(\omega_1)E_2(\omega_2) + \chi^{(3)}(\omega)E_1(\omega_1)E_2(\omega_2)E_3(\omega_3) + \ldots \,, \tag{39}$$

where $\chi^{(i)}$ are tensor susceptibilities of different orders rapidly decreasing with the growth of i. Here, three waves with field strengths and frequencies $E_1(\omega_1)$, $E_2(\omega_2)$, $E_3(\omega_3)$ produce the fourth scattered wave $E_4(\omega = \omega_4)$, also participating in the common four-wave process. If the medium is isotropic, then $\chi^{(2)} = 0$ and the nonlinearity of $P(\omega)$ is determined by the third term in Eqn (39) with the tensor $\chi^{(3)}$ of the fourth rank. The conditions of energy and momentum conservation require the fulfilment of the following relationships for frequencies ω and wave vectors $\mathbf{k}$:

$$\omega_\mathrm{l} = \omega_i \pm \omega_j \pm \omega_k \,, \tag{40}$$

$$\mathbf{k}_\mathrm{l} = \mathbf{k}_i \pm \mathbf{k}_j \pm \mathbf{k}_k \,. \tag{41}$$

The contribution of the third term to (39) is particularly noticeable at high field strengths E_w and in the region of frequency resonances of $\chi^{(3)}(\omega)$ with the real intermediate energy levels of the particles.

Relations (40) and (41) offer various opportunities for four-wave mixing spectroscopy (FWMS). Some of the setups used in plasma spectroscopy are shown in Fig. 17. One of the first observations of FWM is stimulated Raman scattering (SRS) of a high-power laser radiation with a fixed frequency (Fig. 17a). As the laser power increases, the intensity of the Stokes component increases so much that a mechanism complementary to the RS is launched. The interaction between the Stokes component and the incident laser radiation leads to the biharmonic pumping of the upper vibrational level of the molecule and the appearance of the anti-Stokes component. The processes are coherent, and the anti-Stokes radiation has a directional diagram characteristic of the laser radiation. The direction of propagation is determined by condition (41). Although the scattering intensity depends on the concentration of particles, this relationship is rather complex, which is, first of all, determined by the threshold character of the effect and which can be overcome if the amplification of the SRS wave exceeds the losses in the medium. In this case, a high pump intensity is required: it is difficult to control the absence of

medium perturbations and the redistribution of the particles over the energy levels. To remove this difficulty, a few versions of FWM schemes have been proposed for spectroscopy. Let us consider two of them that are substantially in demand in plasma spectroscopy.

In the method of *coherent anti-Stokes Raman scattering* (CARS), combination (40) is used in the form $\omega_4 = \omega_1 - \omega_2 + \omega_1$ (Fig. 17a). The scheme coincides with the SRS, but, along with a pump at frequency ω_1, an external pump wave is used at the Stokes frequency $\omega_2 = \omega_s$ from an additional laser source, which plays the role of Stokes radiation poorly controlled in SRS. The intensity of the additional radiation can vary independently of pump ω_1, without reaching either the SRS threshold or a strong perturbation of the medium. With collinear superposition of beams ω_1 and ω_2, the intensity of anti-Stokes scattering is expressed as

$$I_{\omega 4} \sim (\Delta N)^2 I_{\omega 1}^2 I_{\omega 2} l_c^2 \left(\frac{\partial \sigma}{\partial \Omega}\right)_{\mathrm{RS}}, \qquad (42)$$

where ΔN is the difference between the particle concentrations in the initial and final states in the Stokes RS process, $I_{\omega 1}, I_{\omega 2}$ are the wave intensities at ω_1 and ω_2, and $(\partial\sigma/\partial\Omega)_{\mathrm{RS}}$ is the RS cross section. The quantity l_c is the interaction length of waves ω_1 and ω_2 depending on the focusing conditions and the dispersion of the medium. At reduced pressures, focusing of coaxial beams by lenses with a focal length of 10–100 cm provides local measurements with a transverse dimension of ~ 0.1 mm and a length of $\sim 1-10$ mm [106]. An additional limitation of the localization length is achieved by crossing beams ω_1, ω_2 at small (~ 0.1 rad) specially chosen angles without violating condition (41) according to the BOXCARS, FOLDRD BOXCARS method [103, 107].

The sensitivity of CARS is increased by choosing frequencies ω_1, ω_2 at which at least one of the intermediate virtual levels in the scattering diagram coincides with or is close to a real energy level of the particle in another electronic state (RE-CARS, Fig. 17b). To make all intermediate levels real, one more external wave ω_3 can be used (two-color four-wave mixing, TC FWM [103]).

The concentration sensitivity of the CARS method exceeds the sensitivity of RS. Due to the quadratic dependence of the signal on the concentration of particles (42), the advantage particularly expresses itself at higher pressures. According to estimates [11, 108], the advantage manifests itself already at the partial pressure of the scattering particles $P > 10^{-5}$ Torr, and at $P = 1$ Torr the CARS signal is 6–7 orders of magnitude stronger than the RS one. Since the 1980s, the method has been used in plasma spectroscopy. For example, measurements of the distribution of nitrogen molecules over the vibrational levels in a discharge at a pressure of 2 Torr show a sensitivity of $\sim 10^{14}$ cm^{-3} for vibrational states and $\sim(3-6)\times 10^{12}$ cm^{-3} in selected rotational states [109]. For rotational states of hydrogen molecules, the sensitivity is approximately 3×10^{11} cm^{-3} [110]. Using the resonance RE-CARS scheme, the behavior of CH, NO, and OH radicals in a plasma is studied in the range of $10^{10}-10^{11}$ cm^{-3} [111–113]. Note that, in addition to concentration measurements, the CARS scheme can provide additional courses of action, for example, measuring the strength and direction of the electric field in a plasma [114–117].

Degenerate four-wave mixing (DFWM), an option in FWM, is illustrated in Fig. 17c. It makes use of combination

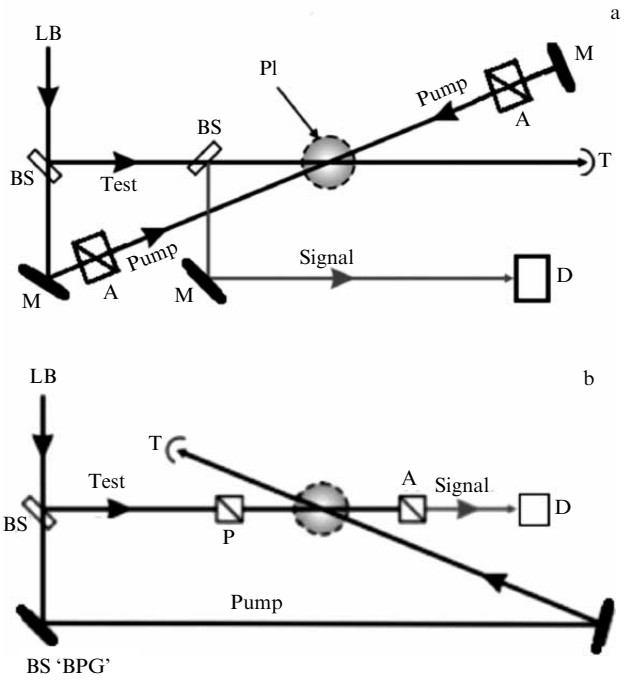

Figure 18. Propagation of beams in FWM measurements with backward scattering. LB — laser beam, BS — beam splitters, Pl — plasma, M — mirror, D — detector, T — trap for light, P — polarizer, A — analyzer. (a) DFWM, (b) LIPS-FWM.

(40) in the form $\omega_4 = \omega_1 - \omega_1 + \omega_1 = \omega_1$. As in the SRS case, one laser source with frequency ω_1 is used. The key issue is that all options of degenerate systems are resonance, and the separation of pump, probe, and signal waves is achieved at the expense of their different directions in space. In the case of DFWM, the laser beam is split into three components (two pump beams and one probe beam), so that, when summing them with the signal beam of the scattered light, vector diagram (41) would hold. In this case, the orientations with 'forward' ($\mathbf{e}_s = \mathbf{e}_p$ being the unit vectors of the scattered and probe waves) and 'backward' ($\mathbf{e}_s = -\mathbf{e}_p$) scattering are possible. An example of organizing an optical DFWM scheme with 'backward' scattering is shown in Fig. 18a (see [103] for details). The scheme with crossing beams has an advantage over the collinear CARS scheme from the point of view of reducing the length of coherent wave interaction, which enhances the measurement locality. The process theory needed to measure concentration continues to be refined. The scattering intensity nonlinearly depends not only on the intensities of the pump and probe beams but also on the ratio of transverse T_1 and longitudinal T_2 relaxation times of the medium. The experience of dealing with the DFWM method shows that acceptable interpretation is possible using simplified models [103, 118, 119]. A general factor of importance is that the scattering intensity quadratically depends on the population difference between the lower l and upper u energy levels, $I_{\mathrm{DFWM}} \sim \Delta N_{lu}^2$, and, in many papers, the method is used to study the distribution of particles over bound states. In particular, the distribution of radicals OH, CH, CN, C_2, ... over the rotational levels is used to analyze reactions involving them and to measure the temperature of the neutral gas component of plasma [120–122]. The interpretation of the measurements of spatial distributions of particles is relatively simple.

As a rule, absolute DFWM measurements are supplemented with test and calibration measurements:

— series of measurements at different saturation conditions, when these factors have different dependences on the conditions in the object [123, 124];

— comparison with the results of direct absorption measurements under conditions where the latter possess sufficient sensitivity [125];

— calibration measurements in the object, where the concentration of the desired particles can be reliably determined from other studies and the results can be repeated using independent methods [126].

One more noncollinear local FWM setup is completely degenerate *polarization spectroscopy* PS-FWM (Fig. 17d) with the same matching condition (40) $\omega_4 = \omega_1 - \omega_1 + \omega_1 = \omega_1$ as for the DFWM scheme. One laser beam split into pump and probe beams is used. The possible paths of the beam are shown in Fig. 18b.

If the radiation is polarized, then, propagating through an absorbing isotropic medium, it polarizes the medium, which affects the probe beam polarization, too. Beyond the absorption line, the medium is not polarized, and if the polarizer and analyzer are crossed, the probe beam does not pass to the detector. At radiation frequencies coincident with the medium absorption lines, the polarization plane of the probe beam rotates and part of the light arrives at the detector, which in this way records the medium absorption spectrum. In terms of the quantum theory, the polarized light induces transitions between the magnetic levels with different orientations of the magnetic moment. Both linear and circular polarization of the laser beam can be used. For molecules, according to the selection rules for the magnetic quantum numbers in the process of scattering, the lines of the P and R branches will be presented in the case of circular polarization, and the lines of the Q branch, for linear polarization. Overall, despite different mechanisms of inducing anisotropy, the situation is like that for the Faraday rotation of the polarization plane in an external magnetic field, as described in Section 3.2.4. This generality is a consequence of the Kramers–Kronig rule for complex permittivity, in which the real and imaginary parts are responsible for refraction and absorption and are interrelated.

The rigorous concrete quantitative relation between signal intensity I_{PS} passed through an analyzer at concentration N_l of particles in the initial state for the scattering cycle is rather complex and depends, in particular, on the transition saturation degree and broadening type. In Ref. [127], based on an analysis of various proposals and experimental data for the case of Lorentz broadening, a semiempirical formula is proposed:

$$I_{PS} = FN^2 I_{pr} I_p^2 (I_p + I_p^{sat})^{-2}, \quad (43)$$

where I_p is the pump radiation intensity, I_p^{sat} is the saturation intensity, I_{pr} is the probe radiation intensity, and F is the fitting coefficient, determined by calibrations. For more details on the theory and procedures for measuring particle concentrations by the nonlinear polarization method, see [103, 128–130].

Polarization nonlinear-optical methods of spectroscopy are highly sensitive compared to analogous direct absorption methods, and their development is promising for operating with radicals and metastable particles.

5. Plasma self-radiation

All methods of quantitative plasma spectroscopy measuring the intensities of the emitted (at finite optical density), absorbed, and scattered light provide information on the differences among the populations of the particle energy levels, coupled by optical transitions. From this point of view, as mentioned in the Introduction, none of them is direct, and substantiated physical models and/or specially organized additional experiments are required to relate the intensity to the total concentration of particles in the absence of equilibrium.

Absorption and scattering methods using light sources external with respect to plasma are active and, as a matter of fact, introduce perturbations into the plasma. This statement is less relevant for classical sources and low-power lasers, but, when using high-power lasers, it is necessary to consider the perturbations related to the saturation of the transition. This is of particular relevance to the discussed issue when, as often happens, the sensitivity is enhanced by increasing the density of transilluminating radiation. The advantage of absorption methods is that, as a rule, an energy level of the ground or metastable state is chosen as the absorbing one. This significantly simplifies the problem of calculating the partition function of the electronic state (5), especially for determining atomic concentrations. In the case of molecules, it is necessary to consider the distribution of particles over the rotational and vibrational energy levels, but, at present, the kinetics of vibrational and rotational relaxation and the functional relations of the population N_i in Eqn (5) are being studied quite well. Due to this reason, methods based on measuring the absorption by particles in ground or metastable states and introducing no perturbations are often called direct methods.

Classical emission methods using the self-radiation of plasma are noninvasive in principle and reflect the natural state of the object. Until now, they have been basic in the elemental spectral analysis using equilibrium plasma both for atomizing the matter and for exciting the glow. Their main difficulties when applied to nonequilibrium objects arise because it is required to know the excitation and decay mechanisms for the radiating states in order to associate the spectral intensities with the total concentration of particles. The difficulties increase if the studied plasma has molecular components, which has been of particular interest recently. However, we should note that the use and modification of classical emission methods are expanding, which is confirmed by the growing number of publications. This is due to a number of reasons, including the following:

— progress in the physics of nonequilibrium plasma and the extension of databases on elementary processes offer new opportunities to analyze the mechanisms of atomic and molecular spectra formation;

— the combination of emission and new laser methods of spectroscopy makes them mutually complementary;

— the extension of plasma technologies and their technical implementations imply choosing adequate means for the processes diagnostics and monitoring, compatible with the objects (thermonuclear and plasmochemical reactors, devices for synthesis of micro- and nanoelectronic elements, equipment for medicine and ecology, rapidly moving objects in a plasma environment, etc.). The use of fairly technically simple, distant, and autonomous methods often has had no alternative yet.

5.1 Absolute intensities of plasma spontaneous emission and particle concentration

For optically thin plasma, ignoring the induced transitions, the relation between the concentration of particles N_u at level u and the intensity of radiation at frequency ν_{ul} of the transition $u \to l$ from a volume element $\mathrm{d}V$ of plasma has the form

$$I_{ul}\,\mathrm{d}V = A_{ul} h\nu_{ul} N_u\,\mathrm{d}V\,. \tag{44}$$

In the case of *absolute* intensity measurements, $A_{ul}N_u$ is determined to the same degree. Formula (5) relates N_u to the total concentration of particles N. The absolute intensities are measured using etalon calibrated ribbon tungsten incandescent lamps (see Section 2.2.2).

For a homogeneous plasma of length L with the finite optical density

$$I'_{ul} = I^{1}_{ul} L S^{*}(\chi_{0,lu} L)\,, \tag{45}$$

where I^{1}_{ul} is the line intensity without self-absorption per unit length (so-called 'primary' intensity), the function $S^{*}(\chi_{0,lu}L)$ is the same as in Eqns (14), (15).

At a finite optical density, not all photons leave the plasma, which can be taken into account by introducing the effective lifetime (effective rate of spontaneous radiative decay, effective Einstein coefficient)

$$A^{*}_{ul} = A_{ul}\Theta(x)\,, \tag{46}$$

where $\Theta(x)$ is the probability of a photon leaving the plasma at point x. For a number of the simplest configurations (semispace, finite thickness layer, cylinder axis, etc.), the probabilities $\Theta(x)$ are expressed analytically [9, 11].

For inhomogeneous media, the spatial profiles of intensities I^{1} are reconstructed from a series of measurements along different observation paths using the methods of plasma optical tomography [131] based on the radiation transfer equation [132]. For axially symmetric plasma with local intensity isolines having the form of circles, when the measurements are executed along the chords of cross sections normal to the axis [133, 134], the reconstruction of I^{1} profiles is performed by means of the Abel transform.

A magnetic field removes degeneracy with respect to magnetic quantum numbers. It also affects self-absorption. In Refs [135, 136], transitions involving resonance and metastable energy levels of He and Ar were studied. In the case of Ar, at an induction of ~ 0.3 T, the plasma becomes more transparent, and self-absorption decreases by 10–50%.

Absolute intensity methods are widely used to measure small concentrations of particles in radiative states. These can be both states in which strong dipole transitions occur and long-lived metastable states, e.g., the important state of 'active' oxygen $O_2(^1\Delta_g)$, the states of atomic and molecular ions, etc. In this case, the results of measurements are independent of the plasma equilibrium conditions. The situation is more complicated when determining the total concentration of particles of a given sort or the populations of their ground states.

The intensity I_{Xul} of the emission line at the transition $u-l$ of particles X with the concentration N_X from a unit volume of optically thin homogeneous plasma, according to relations (44), (45) and the upper level population, is expressed by the formula

$$I_{Xul} = C_X h\nu_{Xul} A_{Xul} k_{Xu} N_X \left(Q_{Xu} + \tau^{-1}_{Xu}\right)^{-1}\,, \tag{47}$$

where C_X are coefficients determined by the optics and the detector, k_{Xu} and τ_{Xu} are the excitation rate and the radiation time of the upper state u, and Q_{Xu} is the rate of upper level decay due to nonradiative processes. Technically, this is one of the simple methods to determine the concentration of particles N_X; the main problem is to determine the values of Q_{Xu} and k_{Xu}, but, in the absence of equilibrium, it has no universal solution. Various processes can participate in the excitation and nonradiative decay of energy levels, and they should be considered in each particular case.

Such studies are described in multiple papers; there is also a generalizing analysis, e.g., in reviews and monographs [8, 10–12, 137]. Usually, one of the plasma models is taken as a base, most frequently, the balance coronal model (CM) or collisional-radiative model (CRM). Depending on the conditions, they include the processes of interaction between the charged and neutral particles with their characteristic manifestations in the emission spectrum.

There are various signs of the presence of parallel processes of exciting radiative states. For example, if the excitation occurs by direct electron impact, then, due to the mass difference, the changes in momentum and angular momentum of particles are not great, except the lightest ones (H, H_2) at low kinetic temperatures < 100 K in long-lived ground states with Maxwell velocity distributions and Boltzmann distribution over the rotational states. The emission spectra demonstrate normal Doppler broadening, and, in the case of molecules, a Boltzmann distribution in the ensemble of rotational levels of the excited states (so-called copying). This, in particular, underlies the definition of temperature for the main bulk of neutral gas in a plasma. If, on the other hand, the excitation occurs with the participation of heavy partner particles, then, depending on the energy defect in the reaction elementary event, groups of radiating particles with other velocity distributions and rotations form. In this case, singularities appear in the translational motion and rotation energy distributions, which manifest themselves in a line contour shape and intensity distributions in the rotational structure of vibrational bands of the spectrum of electronic transitions. Additionally manifested are such effects as alternating intensities in the rotational structure of diatomic homonuclear molecules, not related to the nuclear spin of the radiative particles; here, the symmetry of terms of colliding heavy particles plays a role. The distribution of molecules over the vibrational levels under electronic shell excitation by electron impact 'copies' that in the ground state in accordance with the Franck–Condon principle; it can be violated upon excitation with heavy particles. This should be taken into account when using the excitation models. Such specific features mostly manifest themselves in low-pressure plasma and for radiative states with a short radiative lifetime. However, they can also be restored at high pressures, when the lifetime of the radiative state is determined by collisional quenching with characteristic times less than (or comparable to) the relaxation time of the radiative states in the translational, rotational, or vibrational degrees of freedom. By combining such features, it is possible to separate the excitation mechanisms, which is of importance for the interpretation of spectra and diagnostics, including particle concentration measurements.

For example, the possibility is known of measuring the concentration of water molecules in plasma by the spectrum of hydroxyl radicals [5]. The resonance spectrum of $OH(X^2\Pi \leftarrow A^2\Sigma)$ is excited simultaneously by direct electron impact $e + OH$ and via the intermediate state of the initial water molecule $H_2O(X^1A_1) + e \rightarrow H_2O(B^1A_1) + e \rightarrow OH(A^2\Sigma) + H + e \rightarrow OH(X^2\Pi) + h\nu + H + e$. In the second exothermal process, the OH molecules are created with fast rotation and, due to the decay statistics of the repulsive $H_2O(B^1A_1)$ state, a Boltzmann ensemble of rotating radiative radicals is formed, but with a temperature that differs from the temperature of the ensemble produced by direct electron excitation. Analyzing the intensities in the rotational structure of the OH spectrum allows separating the contributions of mechanisms. If in the absolute intensity measurements only the $OH(A^2\Sigma)$ molecules with 'fast' rotations are taken into consideration, the H_2O concentration can be determined [138], and the group with 'slow' rotations yields the concentration of OH radicals.

In a number of papers (see, e.g., [139–141]), a method is developed for measuring the concentrations of hydrogen and deuterium atoms and molecules by the intensities of α, β, and γ lines of the Balmer series. The excitation of states with quantum number $n = 2, 3, 4$ by electron impact from the ground state of the atom, the dissociative excitation of molecules, the recombination of the molecular ion with an electron, and the self-absorption of radiation at resonance transitions of Lyman series are taken into account.

5.2 Actinometry

All processes occurring in plasma are initiated in one way or another by free electrons. Direct electron impact is the most universal and often the main mechanism giving rise to plasma emission. It is this universality that grounds the method of optical actinometry (OA). In the literature on this method, the term 'line ratio' is also used; it is more familiar in geophysics and meteorology in connection with studies of solar radiation transformation. In application to plasma spectroscopy, it was proposed in [142–144] and until now continues to be successfully applied and developed. The method is based on comparing the emission line intensities for particles X whose concentration is to be determined and particles A (actinometer) whose concentration is known. In this case, the measurement of absolute intensities becomes unnecessary. Such a calibration system is analogous to the one with laser excitation of two particles, discussed in Section 2.3 (LIF, TALIF). An important difference is that, in the fully optical version, the choice of the laser frequency ensures selective excitation of the radiative states, whereas the intensity of spontaneous emission of plasma is determined by the form of energy dependences of the excitation cross sections of these states by electrons.

If we write Eqns (47) for the particle X to be detected and the actinometer A and compose their ratio $N_X/N_A \sim I_X/I_A$, we can see that it is independent of the concentration of electrons (which similarly enters the rates k_{Xu} and k_{Au}). If the actinometer is chosen such that the cross sections of excitation of radiative state of X and A by electrons are close in both threshold values and form, then the ratio of intensities I_{Xul}/I_{Aul} becomes practically independent of the form of energy distribution of electrons, too. The differences in the form of cross sections can be taken into account by corrections. Particles whose concentrations in plasma are known from additional measurements [142, 143] or inert gas atoms [144] are chosen as actinometers. Recommended actinometer pairs are listed in review [5].

Not long ago, the OA method was modified into multispectral OA [145]. This version allows for the specific features related to plasma chemical activity, and the concept of intermediate actinometers is introduced. If the transformations of the particles of the initial plasma-producing gas are deep enough, then the problem of taking into account the collisional quenching of the radiative states arises, since it is unknown a priori which particles should be considered for both the detected particles X and the actinometer A. Due to this, the system of equations for different actinometric pairs $N_{Xi}/N_{Ai} \sim I_{Xi}/I_{Ai}$ is nonlinear because of the presence of particle concentration values in the expressions for quenching rates:

$$Q_{X_i} = q_{X_i} \sum_{j,l} (N_{X_j} + N_{A_l}), \quad Q_{A_i} = q_{A_i} \sum_{j,l} (N_{X_j} + N_{A_l}). \quad (48)$$

The procedure of analyzing the spectra in such a situation [145] implies using a number of sequential iterations, each including two approximations. In the first iteration, the concentrations of particles are determined, which manifest themselves in the plasma emission spectrum and for which only an atom of inert gas in the plasma-forming mixture satisfies the actinometric pair conditions. These data are used to solve the nonlinear equation with the quenching rates in the form (48). In the second iteration, the new-formed particles with the concentrations measured in the first iteration are used both to consider the quenching with their participation and as a new (intermediate, secondary) actinometer. Equations $N_{Xi}/N_{Ai} \sim I_{Xi}/I_{Ai}$ are supplemented with the condition of brutto chemical balance with the number of atoms of all sorts conserved. The iterations are repeated until convergence. As a result, the number of types of particles whose concentrations are determined increases, the accuracy of measurements increases, and the possibilities of choosing the region of the spectrum under the conditions of various objects of study expand. The procedure has been approved in the measurements of concentrations of H_2O, O, H, and OH in a hollow-cathode discharge in a humid inert gas [145].

The methods of absolute intensities and actinometry of spontaneous emission are rather general. Let us present a more specific example.

5.3 Relative intensities of resonance transition lines at finite optical density

The considered method of determining concentrations combines the elements of emission and line absorption methods, manifesting themselves in the self-absorption effect. No external source of light is needed to measure the absorption. The method is applied in spectroscopy to measure the optical transition probabilities [9] and concentrations of H atoms [139] and was mentioned above in Section 2.2. In Ref. [146], it was used to measure the concentration of boron atoms in the plasma of the glowing discharge positive column in a tube [146]. Figure 19 illustrates the appropriate schematic diagram. The intensities of the $3^2S_{1/2} - 2^2P_{1/2,3/2}$ doublet resonance lines are measured, with ^2P being the ground state. The energy difference dE for $^2P_{3/2} - ^2P_{1/2}$ amounts to 15 cm^{-1} and is small compared to the energy of thermal atomic motion $kT \approx 300$ cm^{-1}. The states can be considered thermalized with the Boltzmann factor $\exp(dE/kT) \sim 1$. The radiation from plasma in the region

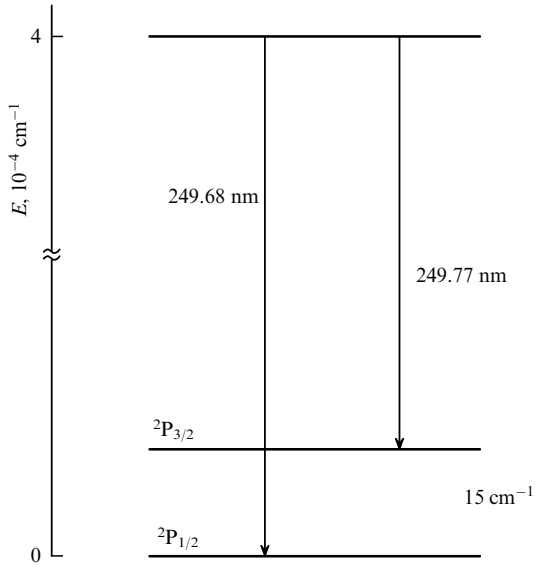

Figure 19. Resonance doublet of the boron atom.

near the discharge axis is recorded, and the plasma can be considered homogeneous. Under such conditions, the intensity of each line can be expressed using Eqns (45), (46); functions S^* depend only on $\chi_{0,lu}L$ and, in correspondence with (2)–(4), on the population of the absorbing energy level, which for atoms practically coincides with their total concentration. The described situation is rather typical, and the method is worth attention for generalizations in the quantitative spectroscopy of nonequilibrium objects.

6. Examples and results of studies

We summarize the results of applying the methods of quantitative spectroscopy to measuring the concentrations of small gaseous components of nonequilibrium plasma in Table 2. As planned in the Introduction, it is based on a list of particles (the first column). The second column indicates the studied plasmatic forms and its general characteristics. We restrict ourselves to laboratory and technological subjects, leaving apart astrophysical studies worth a separate analysis. The third column presents data on the methods of measurement. The abbreviations for objects and methods introduced in the previous sections have been clarified and explained once again. The fourth column contains details of conditions, aims, and the main results of studies and references to original papers.

7. Conclusion

The last two decades have been marked by a noticeably increasing interest in research in the field of the physics and chemistry of nonequilibrium plasma, combining applied and fundamental aspects. Most modern experimental methods are interesting and new ones are being developed, with the priority of noninvasive methods of optics and spectroscopy.

Methods of plasma laser spectroscopy, including the use of semiconductor lasers with tunable frequency, have become widespread and entered researchers' toolkits. Some problems with this technique are due to the fact that, although covering a wide range of wavelengths from the UV to IR regions, particular heterostructures suffer from frequency-tuning limitations and should be chosen based on the aims of studies of the processes with the participation of concrete particles. Progress in this area has been outlined in connection with the use of quantum cascade lasers tunable within ranges of up to ~ 100 cm^{-1} and operating at room temperature, along with the traditional laser diodes tunable within 1–10 cm^{-1}.

New methods of nonlinear spectroscopy have successfully established themselves as techniques that complement already known laser methods, for example, fluorescence, and methods and expanding applications of multiphoton degenerate and nondegenerate scattering schemes with the possibility of 2D and 3D measurement localization. Let us note the first studies on the use of methods based on femtosecond lasers, which provide high temporal and/or spectral resolution for different schemes of recording spectra. The advent of this new, although not yet universally

Table 2. Conditions, methods and results of studies of small components X in plasma.

Particle	Object*	Method**	Comment, concentrations [X], cm^{-3}
Atoms in ground states			
H	CVD; 160 – 300 W, 20 kPa	ACT	H_β 486 nm, Kr actinometer (427 – 455 nm, 557 – 587 nm); (a) Kr:H_2:CO (0.037:1:0.041) — [H] $\sim (1.3-2.2)\times 10^{16}$; (b) Kr:$H_2$ (1:24) — [H] $\sim (1-1.9)\times 10^{16}$ [147]
	ICP, 10 – 1000 W	L – L	L_α 121.6 nm, MHCD(L) light source, H_2 (7 Pa) + Ar (8.8×10^4 Pa); 1.33 Pa, [H] $\sim 2\times 10^{11}-1\times 10^{13}$ [148]
	MWD, 2.45 MHz, 250 W	WB AOS	C_2F_6:H_2 (1:2); 10 – 80 Pa; MHCD 121.6 nm; [H] $\sim 10^{12}-3\times 10^{14}$ [149]
	HFD 13 MHz, 600 W, tube 60 cm long, D 8 cm	TALIF	Excitation 2×205 nm, fluorescence 656 nm; calibration by Kr, excitation 2×204.2 nm, fluorescence 826 nm; saturation broadening [150]; [H] $\sim 2\times 10^{13}$ [151]
	Flame	LIPS	H_2 — air; 2000 K; calculated calibration [H] $\sim (2-8)\times 10^{15}$ [152]
	HFD-ICP, 13.56 – 500 MHz, 10 – 1000 W	WB AOS, L – L	H_2, N_2-H_2, N_2-NH_3 1.3 – 100 Pa; MHCD light source; [H] $\sim 7\times 10^{10}-4\times 10^{12}$ [23, 43]
	ICP 50 – 850 W	WB AOS, L – L	Ar:H_2 (1:9); 30 – 50 mTorr; MHCD light source 121.56 nm; [H] $\sim (2.1-12.5)\times 10^{11}$ [153]
D	HCD 50 cm^3, 30 – 50 W	ACT	0.6 mbar, He:Xe:Ar = 99:1:1:H_2O (0 – 10%):D_2(1 – 2%) D_α 655.6 nm, Ar actinometer 751.46 nm; [D] $\sim (1-14)\times 10^{13}$ [154]

Table 2. (continued)

Particle	Object*	Method**	Comment, concentrations [X], cm^{-3}
	Spherical tokamak HIT-SI3, $n_e \sim 10^{12}-10^{13}$, T_e 5–20 eV	TALIF	Discharge in D_2. Measurements 2 ms after injection. Excitation 2×205.08, fluorescence 656.27; Kr 2×204.3, fluorescence 826.3, at a distance from the wall: (1) 11 cm: $[D] \sim 5 \times 10^9$, $T_D \sim 0.7$ eV; (2) 18 cm: $[D] \sim 5 \times 10^9$, $T_D \sim 1.7$ eV [155]
H, D	Plasma outflow from discharge in a tube D 25 mm, CCP, ICP (H, L) modes 100–800 W, 10–16 MHz, 1200 G	TALIF	1–10 mTorr $Kr + H_2, D_2$; excitation 2×205 nm, fluorescence H 656 nm, axial resolution; calibration by Kr. $[D, H] \sim (2-6)\times10^{12}$, $T_{D,H} \sim 0.08$ eV; all other conditions being the same $[D] \sim 2[H]$ [156]
	Calibration test in gas, 1–100 mTorr	TALIF	Calibration with Xe, excitation 2×209.3 nm, fluorescence 656.0 nm. TALIF cross-section ratio $(\sigma^{Xe}/\sigma^{H,D}) = 0.024$ [81]
	ECR 2.4 GHz, 100 W, 500 cm^3	OES, L–L	$He:(H_2, D_2)$ (1 : 10); 2–20 Pa; $H_{\alpha,\beta,\gamma}$, self-absorption $[H] \sim (2-20) \times 10^{12}$; $[D] \sim (6-20) \times 10^{12}$ [139]
C	ICP: 13.56 MHz, 10–1000 W	WB AOS, L–L	8 Pa CO + 5%Ar; MHCD light source 165.7 nm; $[C] \sim 2 \times 10^{11}-10^{14}$ [149]
	MWD 2.45 MHz, 250 W	WB AOS, L–L	MHCD 165.7 nm; $C_2F_6:H_2$ (1 : 2); 10–80 Pa; $[C] \sim 5 \times 10^{12}$ [149]
	ICP 13.56 MHz, 250 W	WB AOS, LIF	CF_2-H_2; 10–80 Pa; MHCD light source 165.7 nm $[C] \sim 5 \times 10^{12}$ [43]
F	Flow from ICP 10–500 W	ACT	SF_6 + 5%Ar; 20–200 mTorr, F (703.8 nm), actinometer Ar (750.4 nm, 811.53 nm); $[F] \sim (0.3-1.8) \times 10^{14}$ [157]
	CCD 811 MHz, 90–110 V	ACT	50 mTorr, 150 mTorr, $Ar:CF_4:CF_3$ (1 : 1 : 1); $[F] \sim (5-8) \times 10^{12}$ [158]
	Flow from ICP 13.56 MHz, 0.3–1.5 kW	LIF	2×10^{-3} Torr C_4F_8; distribution of particles over the flow: $[F] \sim (1-20) \times 10^{13}$ [66]
Cr	PD vacuum switch D 40 cm, H 50 cm, Cr electrodes; 10 ms, 50 Hz, 1 kV, 20 kA	WB AOS	Residual pressure 5×10^{-4} Pa; laser spark as the light source, 425.43 nm, 427.48 nm, 428.97 nm. Resolution in time and along the discharge axis; $[Cr] \sim (1.5-4) \times 10^{12}$ [47]
Br	HFD, $d = 4$ cm, disks D 19.8 cm, 0.1–14 MHz, 50–150 W	WB AOS	0.15–0.30 Torr Br_2; Br_2 — (415 nm, 490 nm); GaAs etching; $[Br] \sim (2-5) \times 10^{15}$; $Br/B_2 \sim 0.3-0.7$ increases with frequency [159]
B	MWD $49 \times 25 \times 35$ cm^3, 2.45 GHz, 1.2–3.5 kW	L–L, DLS	1–8 mbar, $H_2:Ar:(3.3\%)B_2H_6$; 250 nm doublet reabsorption; $[B] \sim 10^{10}-4 \times 10^{11}$ [146]
	HFD 13.56 MHz, 60–300 W, ~ 500 cm^3	L–L, DLS	$H_2 + CH_4(0-5\%) + B_2H_6(0-0.3\%)$, 60–300 mbar; 250 nm doublet reabsorption; diamond coatings; $[B] \sim (2-11) \times 10^{12}$ [160]
	UHFD 2.45 GHz, 9–23 W cm^{-3}	ABS	$H_2:CH_4:Ar$ (97 : 1 : 2) + B_2H_6(0–100 ppm), 2.5–7.5 kPa; $BH(A^1\Pi-X^1\Sigma)$ 433 nm; Ar 750.3, 811.5 nm; plasma models; CVD technology; $[H] \sim (3-4) \times 10^{11}$ [161]
O	Discharge in a 12-mm tube, 3–40 mA	ACT	0.5–6 Torr, $O_2:Ar$ (2 : 98); 844.6 nm, Ar actinometer 811.5 nm; $[O] \sim (0.2-36) \times 10^{15}$ [162]
O	APPJ from a capillary	L–L	1 atm, $Ar + O_2$ (0.2–1.2%); MHCD light source 130 nm; $[O] \sim 10^{14}-10^{15}$; penicillin deactivation [20]
	Flow from ICP 100–500 W	ACT	20 mTorr, 200 mTorr, O_2 + 5%Ar; 777 nm, Ar actinometer (845 nm); $[O] \sim (0.3-2.4) \times 10^{13}$ [157]
	Flow from PD, 60 Hz	L–L	1 atm, $Ar + 1\%O_2$; light source MHCD 130.217 nm, 130.487 nm, 130.604 nm; $[O] \sim 1.5 \times 10^{13}-7.7 \times 10^{14}$ [163]
	Discharge with planar anode and HC, distance $d = 8$ mm	TALIF	1 atm $He:O_2$ (15 mbar) : NO (0.1 mbar); 2×225.65 nm, 844.68 nm; Xe calibration 2×224.31 nm, 834.91 nm; $[O] \sim 10^{12}-10^{16}$ [44]
	APPJ from discharge in 12-mm tube; MWD 2.45 GHz; 18–55 W	TALIF	1 atm He : air (94 : 6); O — 2×225.586 nm, 844.87 nm; Xe — 2×224.241 nm, 823.16 nm and 834.68 nm; $[O] \sim (10^{15}-7 \times 10^{16})$ [164]
	MWD 2.45 GHz; 16-mm tube	CRDS	$N_2O:Ar$ (19 : 360); resonator 104 cm; $^1D_2-{}^3P_2$, 630.03 nm, $[O] \sim (2-16) \times 10^{14}$ [165]
	APPJ from DBD and MHCD	VUV, L–L	Discharges in He, outflow into atmosphere, MHCD light source with H_2, N_2 filling. Absorption 130.217 nm, 130.487 nm, 130.604 nm. $[O] \sim (1-9) \times 10^{13}$ [166]
	Small-volume PD	REMPI (Radar)	100 Torr ($He + 1\%O_2$) 3×225.6 nm; plasma recombination times [167]

Table 2 (continued)

Particle	Object*	Method**	Comment, concentrations [X], cm^{-3}
	APPJ from a capillary (kINPen), 1.1 MHz, 2 – 6 kV	TALIF	1 atm Ar + 1%O_2; O — 2 × 225.6 nm, 844.6 nm; Xe calibration; resolution 0.2 × 0.5 mm^3; [O] ~ (1 – 37) × 10^{14} [168]
	PD, modulation 10 – 100% , carrier frequency 13.56 MHz, 234 V, 9 W, 1 – 50 kHz	OAS, VUV, FTS, OES	1 atm He + 1%(O_2 : N_2 = 1 : 4); source of light is SOLEIL synchrotron; Fourier spectroscopy 130 nm; radiation 2^+N_2 380 nm; effect of modulation; [O] ~ (0.18 – 3.7) × 10^{14} [50]
	HCD 100 × 50 × 10 mm^3, 280 mA	ACT	He : Xe : Ar : H_2O = 99 : 1 : 1 : 33, 0.8 mbar; [O] ~ (1 – 6) × 10^{13} [5, 145]
	DC 10 – 70 mA, NaCl electrolyte as cathode, $CuCl_2$	ACT	Air 1 atm; actinometry ($3p^3P – 3s^3S$) 845 nm, actinometer 2^+ N_2 (0 – 2) 380 nm, [O] ~ $10^{15} – 10^{16}$ [169]
Na	DC 10 – 70 mA, NaCl electrolyte as cathode, $CuCl_2$	ABS	Air 1 atm; Na ($3s^2S$) 589 nm, collisional radiative model; [Na] ~ (3 – 8) × 10^{13} [169]
Dy	Halogen lamp	DLS	300 mbar, Ar/Kr + Hg + DyI_3; 642.19 nm; the role of gravity; [Dy] ~ $10^{15} – 10^{16}$ cm^{-3} [170]
	Halogen lamp	XRIF	1.2 bar; Ar + Hg + DyI_3 + CsI; fluorescence k_α, 47.6 keV, k_β 54.8 keV; 69.8-keV synchrotron as a source; resolution 1 mm^2; [Dy] ~ (6 – 20) × 10^{16} [84]
Cu	DC 10 – 70 mA, NaCl electrolyte as cathode, $CuCl_2$	ABS	Air 1 atm, Cu 327 nm, collisional radiative model; [Cu] ~ (1 – 5) × 10^{13} [169]
N	DC 4 – 10 A with electron beam 120 eV; D = 15-cm chamber, d = 50 cm	VUV, L – L	N_2 0.05 – 0.4 Pa + Ar 0.03 Pa; light source N_2-MHCD, 119.955 nm, 120.022 nm, 120.71 nm; [N] ~ (2 – 20) × 10^{11} [171]
	Flow from ICP 13.56 MHz, 100 – 500 W	ACT	20 mTorr, 200 mTorr, N_2 + 5%Ar; N — 821.63 nm, actinometer Ar — 811.53 nm; [N] ~ (1.5 – 9) × 10^{11} [157]
	Flow from discharge in a tube, length 18.5 cm, D 2 cm; 433 MHz, 300 W	TALIF	440 Pa N_2; 2 × 206.7 nm, fluorescence 742 – 747 nm; Kr calibration 2 × 204.2 nm, 826 nm; [N] ~ (1.5 – 3.5) × 10^{15} [172]
	ICP 13.56 – 500 MHz; injection of atoms	WB AOS	10 – 100 Pa $N_2 – H_2$, $N_2 – NH_3$; light source MHCD 120.0 nm; [N] ~ ($10^{12} – 1.5 \times 10^{13}$) [43]
	MWD 2.45 GHz, D = 26-mm tube, 600 W	ACT	65 – 400 Pa N_2 + Ar (2%) + R, R = He, Ne, Kr, Xe; N_2 : R = (0 – 1); N 742 nm, 744 nm, 746 nm; Ar 811.5 nm; [N] ~ $10^{12} – 10^{14}$ [173]
	PD 10 – 50 kHz, 10 – 100%, carrier frequency 13.56 MHz, 234 V, 9 W	VUV, FTS, OES	1 atm He + 1%(O_2 : N_2 = 1 : 4); source of light is SOLEIL synchrotron; Fourier spectroscopy 130 nm; radiation N_2 380 nm: influence of modulation frequency; [O] ~ (0.2 – 4.4) × 10^{13} [50]
Ti	Low-pressure arc, current 50 – 150 A	L – L	10^{-3} Torr, vacuum sputtering, optical path 50 cm, 398.2 nm and 318.6 nm; light source — HC; [Ti] ~ (0.5 – 2.5) × 10^9 [174]
Si	PD 13.56 MHz, 2 – 20 W	CRDS	0.1 – 3 mbar Ar; Si atoms desorbed from quartz and silicon substrates; 251.4 nm; [Si] ~ $10^7 – 10^8$ [175]
	PD 13.56 MHz, 0.6 W cm^{-2}	WB AOS	5 Pa, SiH_4 (5 – 100%) : Ar (95 – 5%); light source is a deuterium lamp; [Si] ~ 8 × 10^8 – 3 × 10^{10} [23]
Si	ECRP, 2.45 GHz, 10 – 1000 W	WB AOS	(0.7 – 3.5) Pa, SiH_4 : H_2 (1 : 1); light source is deuterium lamp; [Si] ~ (0.2 – 2) × 10^9 [23]
	Reactor (LAM 9400) for etching, ICP 13.56 MHz, 300 W + 90 W (bias)	UVBA	HBr/Cl_2/O_2, HBr/Cl_2/O_2/CF_4, 5 mTorr; 251.43 nm, 250.69 nm, 252.85 nm, 288.16 nm, 263.1 nm; source is Xe lamp 150 W; [Si] ~ (1 – 10) × 10^{10} [176]
S	DC, tube l = 10 cm, d = 1 cm, 1.5 – 5 W	DLS	(1 – 20) mbar; I. CO_2 – Ar(He); content of S in CO_2; sensitivity [S]/[CO_2] ~ 7 × 10^{-7}. II. Discharge in Ar(He), content of S in CO_2 upon desorption from a wall; sensitivity [S]/[CO_2] ~ 2 × 10^{-7}; Calibration by SF_6, SO_2 [177]
Kr	Flow from ICP (H, L modes), 300 – 900 W, 10 – 16 MHz, 1200 G; tube D 25 mm	TALIF	1 – 6 mTorr Kr; 2 × 205 nm, 826 nm, profile along outflow axis; cold Kr calibration. [Kr] ~ 3 × 10^{11} – 3 × 10^{15} [156]
Pb	ICP 27.12 MHz	CRDS, LIF	Elemental analysis; 1 atm, carrier gas Ar; sensitivity: LIF — 3 × 10^{12}, CRDS — 10^{12} [25]
^{238}U	ICP 27.12 MHz	CRDS, LIF	Elemental analysis; 1 atm, carrier gas Ar; sensitivity: LIF — 2.2 × 10^{14}, CRDS — 2.1 × 10^{14} [25]
Excited atoms			
H(n = 2)	HFD 13.56 MHz, tube D 16 mm, 1 – 3 kW, 350 G	DLS	H_2 30 – 110 mTorr; 656 nm; [H(n = 2)] ~ (0.3 – 4) × 10^{10} [72, 178]

Table 2 (continued)

Particle	Object*	Method**	Comment, concentrations [X], cm^{-3}
	MWD-SWD 2.45 GHz, 150 – 700 W, 2.7 ms, tube D 16 mm	DLS	1 – 3 Torr $H_2 : O_2(99 : 1)$; $[H(n = 2)] \sim (1-20) \times 10^{10}$ [179]
	HFD 13.56 MHz, 22 kW coil flow D 40 mm	CRDS	H_2 6 Torr, 60 mm from coil; H_β 486.1 nm $[H(n = 2)] \sim 10^{10} - 10^{11}$ [180]
C (2^1S_0)	Ar flow from arc	CRDS	0.3 mbar Ar + C_2H_2 (0 – 0.06) mbar; $^1P_1 - {}^1S_0$, 247.931 nm; $[C(2^1S_0)] \sim (0.5-5) \times 10^9$ [181]
Xe (6^3P_2, $1s_5$)	DBD 16 kHz, 3 – 4 kV, ~ 1 mA	DLS	Xe 100 – 733 Torr; 2 – 15 mA; 823.163 nm, ($2p_6 - 1s_5$); $[Xe(1s_5)] \sim (1-15) \times 10^{17}$ [16]
He (2^3S_1)	DC 0.3 – 2 A, 0.3 – 3.5 kW, tube D 20 mm	WB AOS	1 atm He; $2^3S_1 - 2^3P_{0,1}$; incandescent lamp as source; spatial resolution; $[He(2^3S_1)] \sim (0.5-5) \times 10^{13}$ [182]
	APPJ from tubes D 2 – 4 mm, DBD, 5 kHz	DLS	1 atm He, flow 3.7 – 14.8 m s^{-1}; $2^3S_1 - 2^3P_{0,1,2}$ 1083 nm, $[He(2^3S_1)] \sim 10^{10} - 2 \times 10^{12}$ [183]
	APPJ from DBD tube D 2.1 mm	DLS	1 atm He, 1083 nm, $[He(2^3S_1)] \sim (1-3) \times 10^{13}$ [184]
	APPJ from DBD tube D 1.6 mm, 940 kHz	DLS	1 atm He, 1083 nm; various propagation media; $[He(2^3S_1)] \sim (1-13) \times 10^{12}$ [185]
	APPJ from DBD channel $40 \times 1 \times 1.8$ mm^3, HFD 13.56 MHz, 30 – 80 W	DLS	1 bar He (1 – 5) : Ar (10%), flux 2 m s^{-1}; 1083 nm; spatial resolution; $[He(2^3S_1)] \sim 10^9 - 1.4 \times 10^{11}$ [186]
He (2^1S_0)	DC 0.3 – 2 A, 0.3 – 3.5 kW; tube D 20 mm	WB AOS	1 atm He; 501 nm; spatial resolution; $[He(2^1S_0)] \sim (1-10) \times 10^{12}$ [182]
Ar ($1s_5$)	Tube, D 7.5 mm, 200 – 600 W, 2.45 GHz	L – L	2 Torr N_2 : Ar (0.1 – 1.0); light source is discharge in Ar. $[Ar(1s_5)] \sim 10^{11} - 10^{13}$ [187]
	APPJ from DBD discharge $40 \times 1 \times 1.8$ mm^3, 13.56 MHz; 30 – 80 W	DLS	1 atm He : Ar (10 : (0 . . . 1); $1s_5 - 2p_9$ 811.531 nm; 1 bar He (1 – 5) : Ar(10%), $[Ar(1s_5)] \sim 10^9 - 1.6 \times 10^{11}$ [186]
	APPJ from discharge in tube D 6 mm, 22 kHz	DLS	1 atm Ar : N_2 (0.999 : 0.001); 811.531 nm; $[Ar(1s_5)] \sim 10^{12} - 2.5 \times 10^{14}$ [188]
	APPJ from DBD, tube D 1.7 mm, 20 kHz, 230 ns, 6 kV, 15 – 20 μJ	DLS	Flux 1100 cm^3 s^{-1}, Ar 1 atm, $1s_5 - 2p_9$, 811.531 nm; $5 \times 10^{12} - 10^{13}$ [189]
	APPJ from DBD in Ar tube is incident on glass in air, 6 kV, 224 ns, 20 kHz	DLS	$2p_7 - 1s_4$ (810.37 nm), $2p_9 - 1s_5$ (811.53 nm), along the flux $[Ar(1s_5)] \sim 10^{11} - 3 \times 10^{13}$; Ar ($1s_5$) lifetime 25 – 550 ns depending on jet velocity [190]
	MWD – MHCD, 1.8 GHz, 0.1 – 0.5 W	DLS	Ar – He 100 – 730 Torr, $2p_9 - 1s_5$, $[Ar(1s_5)] \sim 5 \times 10^{12} - 2 \times 10^{13}$ [191]
	DBD, 6.4 mm, 13.56 MHz, 10 W	OES	200 – 500 Torr (Ar : He = 0.05 . . . 1); spatial resolution. $[Ar(1s_5)] \sim (0.1-5) \times 10^{12}$ [192]
Ar ($1s_{3,4,5}$)	SWD 2.45 GHz, tube D 6 mm	DLS	0.65 – 105 mbar Ar; 772.38 nm, 772.42 nm, 811.53 nm; $[1s_3, 1s_4, 1s_5] \sim 10^{10} - 10^{12}$ [193]
Ar ($1s_{2,3,4,5}$)	DBD, tube D 100 mm, $d = 4$ cm, 4 kV, 30 kHz	OES, DLS, L – L	Ar 40 – 160 Pa, 2p – 1s; L – L self-absorption; OES 738 – 852 nm; DLS 772.42, 800.62, 801.48, 826.45 nm $[Ar(1s)] = 5 \times 10^{10} - 10^{12}$ [194]
	DBD, $d = 4$ mm, 4 kV, 30 kHz, $B = 0.3$ T	DLS, L – L	Ar 100 Pa; 1s – 2p, 801.48, 842.47 nm; self-absorption effect on the kinetics and populations of magnetic sublevels; temporal resolution; $[Ar(1s_4)] = (1.8-3.2) \times 10^{11}$, $[Ar(1s_5)] = (0.6-1.1) \times 10^{12}$ [136]
	DC, region 1 – 1000 μm above structured cathode	DLS	Ar 50 and 400 mbar; 801.699, 800.838, 772.633, and 826.680 nm; $[Ar(1s_{2,3,4,5})] \sim (0.8-20) \times 10^{13}$ [195]
	Overview, various conditions, models	OES, DLS	Argon concentration in metastable states relative to ground state $n_m/n_g \sim 10^{-4} - 10^{-7}$; ionization degree $n_e/n_g \sim 10^{-1} - 10^{-7}$; rates of elementary processes [196]
	Glowing discharge, tube D 26 mm, 20 mA	WB AOS, COMB	Ar, 1 Torr, light source is femtosecond laser continuum; $[Ar(1s_2)] = 5.5 \times 10^9$; $[Ar(1s_4)] = 1.1 \times 10^9$ [68]
Ionized atoms			
H^-	HFD-PD, carrier frequency 13.56 MHz, 4-ms pulses, 10 Hz, 3 kW; afterglow; 350 G	AOS	40 – 63 mTorr H_2; probe measurements of electron concentration during photodetachment; laser 680 nm, 40 mJ cm^{-2}; $[H^-] \sim (1-2) \times 10^{11}$ [89]
	PD 1 kHz, 500 μs, (1 – 12) A; magnetic field, chamber $d = 27$ cm, D 16 cm	AOS, CRDS	H_2 0.2 – 2.4 Pa; lasers 632.8 nm, 532 nm; photodetachment, probe measurements; MPC ~ 22 m; $[H^-] \sim (1.5-15) \times 10^9$ [110, 197, 198]

Table 2 (continued)

Particle	Object*	Method**	Comment, concentrations [X], cm^{-3}
	HFD $47 \times 57 \times 2.4$ cm^3, 13.56 MHz, 120 W	CRDS	0.075 – 0.4 Torr; O_2; H_2; 556 nm; $[H^-] \sim 10^9 - 10^{10}$ [199]
	HFD 13.56 MHz, 20 – 1200 W, 13.56 MHz, magnetic field 40 – 100 G, H, L modes	OES, CRDS	CRDS — 1.06 μm, optical length 120 cm. Relative intensities $H_\alpha/H_\beta/H_\gamma$; ion injection into hot plasma $[H^-] \sim 10^{10} - 10^{11}$ [200]
H^-, D^-	HFD, 1 MHz, ~ 70 – 80 kW, $d = 14$ cm, D 24 cm; expansion into a chamber $32 \times 59 \times 19$ cm^3, 6 G	OES	HFD, 1 MHz, 0.3 – 0.7 Pa, intensities H_α/H_β, D_α/D_β; $[H^-] \sim 10^{16} - 10^{17}$; radiative collisional model; injection of ions into hot plasma [201]
	MWD 2 – 5 kW, 800 G, helical mode	CRDS	H_2, D_2 0.2 – 0.5 Pa, $T_e \sim 1.5 - 2.5$ eV, $n_e \sim (1-3) \times 10^{11}$; injector of ions into hot plasma; $[H^-]$, $[D^-] \sim (0.5-8) \times 10^9$, $[H^-]/n_e \sim 6[D^-]/n_e$ [202]
Ti^+	Low-pressure arc, 50 – 150 A	L – L	$10^{-2} - 10^{-3}$ Torr He; optical path 50 cm, 324.2 nm and 318.6 nm; light source — HCD; [Ti] ~ $(2-7) \times 10^9$; optical coatings [174]
O^-	HFD 13.56 MHz, 120 W $47 \times 57 \times 2.4$ cm^3	CRDS	0.075 – 0.4 Torr; O_2; H_2; 556 nm; $[O^-] \sim 10^{10} - 10^{11}$ [199]
Diatomic molecules			
NO	PD 5 kHz, corona, pin (nozzle) — plane $d = 30$ mm	LIF	Air: NO (2×10^{-4}%); excitation 226.19 nm, fluorescence 230 – 320 nm – γ – system NO (NO $\gamma(0-1)$ – NO $\gamma(0-6)$); spatial distribution; air cleaning; $[NO] \sim 2 \times 10^{14} - 4 \times 10^{15}$ [203]
	PD 100 ms, 0.1 Hz, tube $d = 50$ cm, D 1 cm, 35 mA	DLS	266 Pa N_2 : NO (99 : 1); 1897.35 cm^{-1}; temporal resolution; $[NO] \sim 2 \times 10^{13} - 5 \times 10^{14}$ [204]
	Flame	RECARS	1 atm; H_2 – air, NO additives; 200 K; sensitivity $[NO] \sim 7 \times 10^{14}$; calibration — calculation [205]
	APPJ, 13.56 MHz, DC 5 – 20 W	DLS	1 atm Ar + air (< 1%); MPC 100 m; 1906.14, 1906.73, 1912.07 cm^{-1}; $[NO] \sim (2-38) \times 10^{12}$ [206, 207]
NH	Heated CVD reactor	CRDS	20 Torr H_2 + 1%CH_4 + 1%NH_3; 336 nm ($A^3\Pi - X^3\Sigma^-$); $[NH] \sim 10^{12} - 10^{13}$ [208]
OH	Flame	L – L	Combustion of H_2 in air; light source is MWD in water vapor; 306 – 318 nm, 8 lines of $OH(^2\Pi - ^2\Sigma(0,0),(1,1))$ transitions; $[OH] \sim 5 \times 10^{14} - 2 \times 10^{16}$ [209]
	PD-DBD 50 ns, 0.016 – 1.6 J, 19 cm^{-3}	L – L	1 atm Ar: H_2O (200 ppm) or air; light source — DBD, 11 lines of $OH(^2\Pi - ^2\Sigma(0,0))$ band; OH afterglow dynamics; OH destruction by organic molecules; $[OH] \sim 10^{13} - 10^{15}$ [210]
	PD-DBD 30 – 200 mA, 1 kHz; $55 \times 55 \times 0.55$ mm^3	WB AOS	1 atm Ar : H_2O (7 Torr); light source — LED (10 nm FWHM); $[OH] = (2.65 \pm 0.65) \times 10^{13}$; LIF method calibration [211]
	PD-DBD 10 ms, 0.1 Hz, 44 – 50 W; 5.5 cm^3 and 2.45 cm^3; 10 ms, 0.1 Hz, 44 – 50 W	WB AOS	780 Torr He – H_2O(0.05 – 0.67)% – O_2(0 – 2)%; $[OH] = (6-94) \times 10^{13}$ [212]
OH	DC discharge in a 24-mm diameter tube, 30 mA	L – L	0.3 Torr H_2O, additives 0 – 6 Torr N_2, He, CO_2, O_2; $[OH] = (0-2) \times 10^{13}$ [213]
	pin-to-pin PD, $d = 2$ mm, 170 ns, afterglow 0 – 100 μs	LIF, WB OAS, Rayleigh scattering	1 atm He + 0.84%H_2O; LIF excitation 282.58 nm, fluorescence 308 – 309 nm; UVBA 307 – 309 nm; LIF calibration by Rayleigh scattering in N_2; $[OH] = (0.1-2.5) \times 10^{15}$ [214]
	pin–plane PD, $d = 13$ mm, 24 – 32 kV, < 12 A, 0.2 μs	LIF	1 atm, N_2 + 2.8%H_2O + 2%O_2; spatiotemporal resolution; $[OH] = 5 \times (10^{12} - 10^{14})$ [215]
	APPJ in air from capillary discharge	LIF, WB OAS	LIF excitation 282.58 nm, fluorescence 308 – 309 nm; UVBA 307 – 309 nm; $[OH] \sim (0.1-2.5) \times 10^{15}$ at distance of 1–8.5 mm from plasma source [216]
	ICP 27.12 MHz, 200 W, $l = 27$ mm, D 16 – 20 mm	CRDS	1 atm Ar, H_2O traces; 306 – 308 nm, $[OH] \sim (1.7-8.5) \times 10^{14}$ [217]
	Flame	DFWM	1 atm; H_2 – air – Ar; $T \sim 1400 - 2400$ K; $[OH] \sim (2-20) \times 10^{15}$; no chemical equilibrium in flame [124]
BH	UHFD 2.45 GHz, 9 – 23 W cm^{-3}	ABS	$H_2 : CH_4 : Ar$ (97 : 1 : 2) + B_2H_6 (0 – 100 ppm), 2.5 – 7.5 kPa; $BH(A^1\Pi - X^1\Sigma)$ 433 nm; Ar 750.3, 811.5 nm; plasma model; diamond films; $[BH] \sim (7-20) \times 10^{12}$ [161]
Br_2	HFD 0.1 – 14 MHz, 50 – 150 W, $d = 4$ cm, disks D 19.8 cm, 0.1 – 14 MHz, 50 – 150 W	OES	0.15 – 0.30 Torr Br_2; Br_2 — 415 nm, 490 nm; modeling; $[Br_2] \sim (5-1.5) \times 10^{15}$ [Br] ~ $(2-5) \times 10^{15}$; GaAs etching [159]

Table 2 (continued)

Particle	Object*	Method**	Comment, concentrations [X], cm^{-3}
HCl	Lam Research 9400SE TCP reactor for Si etching 430 W	DLS	10 mTorr. $Cl_2 : HBr$ (0 : 100 – 100 : 0) + 5% Ar; v = 0 → v = 2, 1.79 μm. [HCl] = $10^{13} - 10^{14}$; sensitivity 2×10^{11} [218]
	Hydrocarbon flame in atmosphere	FTIR	3.6 μm. Conditions of flame suppression using CF_3Br [HCl] = 6×10^{13} [192]
	Hydrocarbon flame in atmosphere	DFWM PS	$CH_4 : O_2 : Ar$ (x : y : z); 1 atm; 2000 K; sensitivity ~ 10^{14}; 2D resolution [HCl] ~ $(1.5-70) \times 10^{14}$ [219]
HF	Hydrocarbon flame in atmosphere	FTIR	2.3 μm. Conditions of flame suppression using CF_3Br — [HF] = 7.5×10^{14} and C_3F_7H — [HF] = 3.6×10^{14} [192]
HBr	Hydrocarbon flame in atmosphere	FTIR	4.1 μm. Conditions of flame suppression using CF_3Br — [HBr] = 7.5×10^{14} [192]
CN	DC in a 20-mm diameter tube, current 10 – 40 mA, gas flow 0.2 m s^{-1}	L – L	$CO : N_2 : He : O_2$ 2 – 8 Torr, light source is identical discharge; quenching of CO lasing levels CO; [CN] ~ $3 \times 10^9 - 6 \times 10^{11}$ [220]
	MWD, 2.45 GHz, 1.5 – 3 kW, $121 \times 21 \times 15$ cm^3	DLS	0.3 – 1.5 mbar $N_2 : Ar : H_2 : CH_4$; 1900 – 2130 cm^{-1}; [CN] ~ $(1-3) \times 10^{11}$ [221]
	APPJ from arc 1.6 kW, 12 A, 140 V	LIF	0.7 – 25 Torr, $Ar : H_2 : CH_4$ (1 : 0.9 : 0.005); excitation CN(B – X) 380 – 390 nm, [CN] ~ $(1-6) \times 10^{12}$ [222, 223]
CH	Low-pressure plasmotron jet 5.5 – 6.5 kW	CRDS	50 Torr $Ar : H_2 : CH_4$ (1.4 : 1.8 : 0.06); spatial resolution; 431 nm, $CH(X^2\Pi, v = 0)$ $3 \times 10^{12} - 1.5 \times 10^{13}$ [224]
	Low-pressure arc jet 22 – 74 A	CRDS	0.3 mbar, $Ar : C_2H_2$ (100 : (0.5 – 14)); $X^2\Pi$ (v = 0) – $A^2\Delta$ (v = 0); 430 nm; [CH] ~ $5 \times 10^9 - 8 \times 10^{10}$ [225]
	Low-pressure arc jet 1.6 kW, 140 V	LIF	0.7 – 25 Torr, $Ar : H_2 : CH_4$ (1 : 0.9 : 0.005); excitation CH(A – X) 380 – 390 nm, fluorescence CH 425 – 438 nm; [$CH(X^2\Pi)$] ~ $(1-6) \times 10^{12}$ [222, 223]
	MWD, 2.45 GHz, 1.8 kW, 1200 cm^3, afterglow	RECARS	664 Pa $Ar : CH_4$ (68 : 15); $CH(A^2\Delta - X^2\Pi)$; rotational T_r and vibrational T_v temperatures; calibration by LIF [$CH(X^2\Pi)$] ~ $10^{10} - 10^{11}$ [111]
C_2	Plasmotron jet 5.5 – 6.5 kW	LIF	0.7 – 25 Torr, $Ar : H_2 : CH_4$ (1 : 0.9 : 0.005); excitation 380 – 390 nm, fluorescence 425 – 438 nm; [C_2] ~ $(0.1-4) \times 10^{12}$ [222, 223]
	Plasmotron jet 5.5 – 6.5 kW	CRDS	50 Torr $Ar : H_2 : CH_4$ (1.4 : 1.8 : 0.06); spatial resolution; 515 nm $C_2(a^3\Pi)$ ~ $3 \times 10^{11} - 2.2 \times 10^{13}$ [224]
O_2	HFD 13.56 MHz, 160 cm^3, 80 W	DLS	10 – 1000 Pa, $CH_4 : O_2$ (2 : 1); 13,098.8 cm^{-1} MPC 2.8 m; [O_2] ~ $(0.2-2.5) \times 10^{16}$ [225]
	DC 20 mm, 10 – 40 mA, afterglow	WB AOS	0.2 – 4 Torr, O_2 + 5%Ar, source of light is SOLEIL synchrotron, 170 nm, [O_2] ~ $5 \times 10^{13} - 5 \times 10^{15}$ [226]
CO	HFD 13.56 MHz, 160 cm^3, 80 W	DLS	10 – 1000 Pa, $CH_4 : O_2$ (2 : 1); 2060 cm^{-1} MPC 2.8 m; [CO] ~ $(0.1-2) \times 10^{16}$ [227]
	ICP, 1 kW	DLS	SiCOH etching; 7 mTorr CH_4(12) : (Ar, O_2, C_4F_8, H_2, N_2, CO)(2 – 8); [CO] ~ $(2-7) \times 10^{12}$ [228]
	HFD 13.56 MHz, 1500 cm^3, 15 W	DLS, FTIR	13 Pa Ar, He + C_2H_2, CH_4, 2169 cm^{-1}, [CO] ~ $(3-20) \times 10^{12}$ [229]
	PD, 1 kHz, 2 – 10 kW, 1 m^3	DLS	$N_2 : H_2 + x\,CH_4(CO_2)$, $x < 10\%$; 2119.68 cm^{-1}; [CO] ~ $10^{13} - 2 \times 10^{15}$; using line 2119.68 cm^{-1} sensitivity is ~ 10^{12} [230]; under close conditions [231] sensitivity is ~ 2×10^{11} for line 2150.34 cm^{-1}
CF	HFD-ICP 13.56 MHz, afterglow, 0.3 – 1.5 kW, 1 kG, 20-ms pulses, 5 Hz	LIF	2×10^{-3} Torr C_4F_8; distribution of particles in flow: [CF] ~ $(1-15) \times 10^{12}$ [232]
	ECRP, 2.45 GHz, 10 – 800 W	DLS	0.4 Pa; gases: C_4F_8 — [CF] ~ $(4-10) \times 10^{11}$; C_2F_6 — [CF] ~ $(1-4) \times 10^{11}$; CF_4 — [CF] ~ $(1-4) \times 10^{12}$; CHF_3 — [CF] ~ $(1-4) \times 10^{11}$ surface etching [23]
SiH	PD 13.56 MHz, 0.6 W cm^{-2}	WB OAS	5 Pa, gases SiH_4 (5 – 100%) : Ar (95 – 5%); [SiH] ~ $(1-5) \times 10^{10}$ surface etching [23]
S_2	Flame	DFWM	1 atm; $C_3H_8 : air : SO_2$; 1400 – 1700 K; $S_2(^3\Sigma_u - \Sigma_g)$ 308 – 310 nm; 2D resolution; [S_2] ~ $(5-18) \times 10^{14}$; calibration by absorption in neutral gas [125]
SiX	LAM 9400 reactor for etching, ICP 13.56 MHz, 300 W + 90 W (bias), D 200 mm	WB AOS	$HBr/Cl_2/O_2/CF_4$, 5 mTorr; light source is Xe lamp; $HBr/Cl_2/O_2$, $HBr/Cl_2/O_2/CF_4$, 5 mTorr; 220 – 340 nm, X = Cl, 280 nm, [SiCl] ~ $(1-15) \times 10^{10}$; X = O, 220 – 238 nm, [SiO] ~ $(0.5-2) \times 10^{10}$; X = F, 290 nm, [SiF] ~ $(0.1-2) \times 10^{10}$ [176, 233]

Table 2 (continued)

Particle	Object*	Method**	Comment, concentrations [X], cm^{-3}
NH	CVD with heated element ~ 2500 K	CRDS	20 Torr $H_2 + 1\%CH_4 + xN_2 + yNH_3$; $(A^3\Pi - X^1\Sigma)$ 336 nm; profile near heater $T \sim (2100-700)$ K; $[NH] \sim (10^{12}-10^{13})$ [208]
Polyatomic molecules			
BCl_3	PD 50 mHz, 800 K, 3 kW	DLS	1.6 Torr $N_2 : H_2 : Ar : BCl_3$ (10 : 65 : 20 : 2); 963.46 cm^{-1}; optical path 15 cm; $[BCl_3] \sim (0.2-3.5) \times 10^{14}$ [234]
B_2H_6	HFD 13.56 MHz, 60 – 300 W, ~ 500 cm^3	DLS	$H_2 + CH_4(0-5\%) + B_2H_6(0-0.3\%)$, 60 – 300 mbar; 2599.78 cm^{-1}; MPC 9.6 m; $[B_2H_6] \sim (2-12) \times 10^{12}$ [160]
H_2O	DC, tube D 20 mm, 2 – 10 mA	OES, DLS	$H_2O : He : Xe$ (148 : 99 : 1), $[H_2O] \sim (1-2.5) \times 10^{14}$, 0.5 mbar [235, 236]
	HFD 13.56 MHz, 5×10^4 cm^3, 40 – 100 W	DLS	1 – 10 Pa $Ar : N_2 : (Al(OC_3H_7)_3)_x$, $(x = 1-7)$; MPC 15.8 m; 1375.086 cm^{-1}; $[H_2O] \sim (0.1-4) \times 10^{13}$ [237]
	PD, 1 kHz, 2 – 10 kW, 1 m^3	DLS	$N_2 : H_2 + xCO_2$, $x < 10\%$; 3837.87 cm^{-1}; $[H_2O] \sim 10^{14}$ [230]
HNO_3	HFD 13.56 MHz, 5×10^4 cm^3, 40 – 100 W	DLS	1 – 10 Pa $Ar : N_2 : (Al(OC_3H_7)_3)_x$, $(x = 1-7)$; MPC 15.8 m; 1332.891 cm^{-1}; $[HNO_3] \sim (1-5) \times 10^{13}$ [237]
HDO	DC, tube D 20 mm, 2 mA	DLS	$He : D_2 : H_2O$ $(x : y : z)$, ~ 1 Torr, 7179.79 – 7180.61 cm^{-1}, $[HDO] \sim (3.5-5.5) \times 10^{13}$; sensitivity $\sim 10^{12}$ [235, 236]
	DC, tube D 20 mm, 4 mA	DLS	0.5 mbar $He(8.5 \times 10^{15}) + H_2O(2.1 \times 10^{14}) + D_2(1.8-5.3) \times 10^{15}$; $[HDO] \sim (3.5-5.5) \times 10^{13}$ [139, 140]
C_3	Jet from DC arc 1.6 kW, 12 A, 140 V	LIF	100 Pa, $Ar : H_2 : CH_4$ (1 : 0.9 : 0.005); excitation $C_3(A-X)$ 380 – 390 nm, fluorescence 425 – 438 nm; $[C_3] \sim (0.5-12) \times 10^{12}$ [222, 223]
CF_2	DBD (5.4 – 31.6) cm^3, 4 – 96-ms pulses; 3 – 18 kV	FTIR, WB OAS	1 atm Ar/9%(CF_4, C_2F_6, $C_2H_2F_4$, C_3F_8, c-C_4F_8); FTIR 1114 cm^{-1}; UVBA 250 – 270 nm, source is Xe lamp; $[CF_2] \sim (0.14-8.12) \times 10^{14}$ [238]
	CCP 81 MHz	WB OAS	150 mTorr, $Ar/CF_4/CF_3$; 50 mTorr; 250 nm, $CF_2(^1B_1 - {}^1A_1)$, source is D_2 lamp; $[CF_2] \sim 10^{12}-10^{14}$ [158]
	ICP 13.56 MHz, 1000 W	DLS	1.33 Pa CF_4; QQL 1106.2 cm^{-1}; density dynamics in the process of etching; SiCOH, $[CF_2] \sim 10^{12}-10^{14}$ [239]
	Flow from ICP 13.56 MHz, 0.3 – 1.5 kW, 1 kG, 20-ms pulses, 5 Hz	LIF	2×10^{-3} Torr C_4F_8; distribution of particles over flow: $[CF_2] \sim (1-12) \times 10^{12}$ [232]
	ECRP, 2.45 GHz, 10 – 800 W	DLS	0.4 Pa; gases: C_4F_8 — $[CF_2] \sim (4-9) \times 10^{11}$; C_2F_6 — $[CF_2] \sim (6-10) \times 10^{11}$; CF_4 — $[CF_2] \sim (1-10) \times 10^{11}$; CHF_3 — $[CF_2] \sim (8-11) \times 10^{11}$ [23]
CF_2O	Hydrocarbon flame in atmosphere	FTIR	When suppressing the flame by CF_3Br, $[CF_2O] = 2.7 \times 10^{14}$ are formed, by C_3F_7H — $[CF_2O] = 1.8 \times 10^{14}$ [192]
CF_3, CF_4, CHF_3	ECRP, 2.45 GHz, 10 – 800 W	DLS	0.4 Pa; gases: C_4F_8, CF_4, CHF_3; $[CF_3] \sim (1-6) \times 10^{12}$; $[CF_4] \sim (1-7) \times 10^{13}$; $[CHF_3] \sim (4-20) \times 10^{12}$ [23]
CO_2	HFD 13.56 MHz, 160 cm^3, 80 W	DLS	10 – 1000 Pa, $CH_4 : O_2$; 2043 cm^{-1} MPC 2.8 m; $[CO_2] \sim (0.2-2.5) \times 10^{16}$ [227]
	PD, 1 kHz, 2 – 10 kW, 1 m^3	DLS	$N_2 : H_2 + xCH_4(CO_2)$, $x < 10\%$; 606.277 cm^{-1}; $[CO_2] \sim (0.1-1.2) \times 10^{15}$ [230]
	DC discharge, tube $d = 60$ cm, D 2 cm, 230 W	DLS	1 Torr $N_2 : CO_2$ $(1 : (10^{-2} - 5 \times 10^{-4}))$; 2324.976 cm^{-1}; $[CO_2] \sim 1.5 \times 10^{13} - 3 \times 10^{16}$; sensitivity 2×10^{12} [240]
$^{13}CO_2$	MWD, 2.4 GHz, 7 J cm^{-1}	DLS	100 Torr ($^{13}CO_2/^{12}CO_2 = 0.011$, $^{13}CO_2$ (2283.48 cm^{-1}, $X^1\Sigma$ $(v_3 = 0 - v_3 = 1)$); path length 9 cm; $[^{13}CO_2] \sim 3 \times 10^{15}$ [241]
	HVD 1 – 5 W	L – L	10.6 μm, 11.2 μm; 3 Torr, $N_2 + 5\%CO_2$; optogalvanic effect; $[^{13}CO_2] \sim 10^{11}$ [69]
CH_3, CH_4, C_2H_2, C_2H_4, C_2H_6, CH_2O, CH_2O_2, CH_3OH, C_2N_2, NH_3, HCN	Planar reactor, discharge $121 \times 21 \times 15$ cm^3, 2.45 GHz, 1.5 – 3 kW	DLS, WB OAS	$N_2 + Ar + H_2 +$ hydrocarbons, total pressure 0.3 – 1.5 mbar; quantum cascade lasers at 16 μm; MPCs with the optical path length 2.4 – 36 m; in the UV region light source is MHCD 0.216 μm; concentration of particles in range $10^{11} - 10^{15}$. Data are used to determine energy cost of particle decay in plasma $10^{14} - 10^{16}$ molecules J^{-1} [221, 242 – 244]

Table 2 (continued)

Particle	Object*	Method**	Comment, concentrations [X], cm^{-3}
CH_3	HFD 13.56 MHz, 160 cm^3, 80 W	DLS	10 – 1000 Pa, $CH_4 : O_2$; 606 cm^{-1} MPC 2.8 m; $[CH_3] \sim (1-8) \times 10^{11}$ [227]
	SWD 2.45 GHz, 0 – 50 W cm^{-3}, tube D 6 mm	DLS	$H_2 - CH_4$ 0.1 – 4 Torr, 606.12 cm^{-1}, $[CH_3] \sim (6-20) \times 10^{11}$ [245]
	Flame	REMPI (Radar)	1 atm; CH_4/air; (2 + 1)-photon scheme; 2D resolution; calibration by Ar using the (4 + 1)-photon scheme; coherent scattering 10 GHz. $[CH_3] \sim (0.5-5) \times 10^{15}$ [246]
	Flame	DFWM	1 atm CH_4/air; 216 nm; 3D resolution; $[CH_3] \sim (2-28) \times 10^{14}$ [247]
C_2H_2	Flame	DFWM, PS	1 atm; C_2H_4/air; 1660 – 1750 K; soot; 2D resolution; calibration — gas; $[C_2H_2] \sim (1.5-40) \times 10^{15}$ [130]
CH_2O	PD-DBD 9 kV, 24 kHz	WB AOS	620 Torr, air + H_2O (+ H_2O_2); closed gas flow cycle; femtosecond laser as a light source; MPC 18 m; $[CH_2O] \sim 1.5 \times 10^{13}$ [67]
HCN	PD, 1 kHz, 2 – 10 kW, 1 m^3	DLS	$N_2 : H_2 + xCH_4(CO_2)$, $x < 10\%$; 3339.88 cm^{-1}; $[HCN] \sim 10^{14}$ [230]
	CCD 13.56 MHz, 40 – 100 W	DLS	$L_{eff} = 15/8$ m; Ar, $Ar : N_2 + Al(OC_3H_7)_3$; 1382.5 cm^{-1}; $[HCN] \sim (1-4) \times 10^{13}$ [237]
CH_3OH	ICP 40 MHz, 30 – 200 W; D 20-mm tube	TS	$Ar : CH_3OH$ (6 : 1), 0.5 – 6 Torr, MPC, path 37 cm; rotational spectrum 100 – 600 GHz. $[CH_3OH] \sim (1-3) \times 10^{16}$ [248]
CH_3OH, CCl_4, CH_2Cl_2, C_2HCl_3	D 17-cm tube; (a) supported by electron beam 125 keV, (b) pulsed corona discharge, (c) DBD	FTIR	Plasma air cleaning of pollution at a level of 100 ppm. Measured concentrations $\sim 10^{13} - 2 \times 10^{15}$ [249]
O_3	APPJ — steady-state and pulsed (bunches) plasma jets, from CW and pulsed discharges at atmospheric pressure — DC, DBD, streamers, coronas, MHC-based micro-discharges, capillary... . Transport of active particles from plasma to object and result of impact are studied	WB AOS, DLS, L – L	Gas mixtures at atmospheric pressure $Ar : O_2 : N_2$ H_2O, $He : (O_2$, NO, Xe, $CF_4)$. O_3 concentrations varied $(10^{12} - 10^{16})$ depending on plasma source, plasma-forming gas, and distance in the transportation medium. H_2, D_2, Xe lamps [44, 250, 251], Hg – Ar lamps [252], and KrF excimer lasers [160, 253] are used in absorption measurements in the region of O_3 electronic band maximum at 250 nm. DL including QCL lasers [254], diffraction [255] and FTIR spectrometers [256] are used in the IR range of vibrational transitions at 10 μm
O_2F	APPJ from discharge 0.2 × 5 × 10 cm^3; 20 W cm^{-3}	WB AOS	1 atm in $He : CF_4 : O_2$ (20 : 04 : 0.2) discharge; D_2 lamp light source; 215 nm; major radical $[O_2F] \sim 3.5 \times 10^{14} - 1.3 \times 10^{15}$ [250]
NO_2	APJJ from capillary	FTIR	1 atm $Ar : O_2 : N_2 : H_2O$ in various proportions; MPC 19.2 m, 100 Torr; 1550 – 1650 cm^{-1}; $[NO_2] \sim (1-8) \times 10^{14}$; kinetics [256]
	DBD 50 Hz, 56 – 70 kV, 60 × 50 × 2 cm^3	WB AOS	1 atm air 5–70% humidity; 250 – 257 nm; afterglow 15 – 120 s; $[NO_2] \sim (2-20) \times 10^{16}$ [255]
	DBD 9 kV, 24 kHz	WB AOS, COMB	620 Torr, air + H_2O + H_2O_2; gas flow in closed cycle; femtosecond laser as light source; MPC 18 m; $[N_2O] \sim 2.5 \times 10^{13} - 5 \times 10^{14}$ [67]
NO_2, NO_3, N_2O_4, N_2O_5	DBD 56 – 70 kV, 50 Hz, 60 × 50 × 2 cm^3	WB AOS	1 atm air 5–70% humidity; D_2 lamp 250 – 257 nm; afterglow 15 – 120 s; $[NO_2] \sim (2-20) \times 10^{16}$; $[NO_3] \sim (4-8) \times 10^{16}$, $[N_2O_4] \sim (1.6-16) \times 10^{16}$, $[N_2O_5] \sim (1-16) \times 10^{16}$ [255]
N_2O	PD, tube, 5 ms, 1.23 J	DLS	1.33 mbar $air : NO_2$ (1 : 0.08); QCL set, 2207 cm^{-1}; $[N_2O] \sim (0.2-3) \times 10^{14}$ [257]
	DBD 9 kV, 24 kHz	WB AOS, COMB	620 Torr, air + H_2O + H_2O_2; gas flow in closed cycle; femtosecond laser as light source; MPC 18 m; $[NO_2] \sim 2.5 \times 10^{13} - 9 \times 10^{14}$ [67]
NH_3	DBD, 50 × 50 × 2 mm^3, 0.11 W cm^{-2}	FTIR	1 atm $Ar : NH_3$(200 ppm) : SiH_4(60 ppm); 930 cm^{-1}, 965 cm^{-1}; optical path 50 mm; $[NH_3] \sim (3-5) \times 10^{15}$; sensitivity $\sim 10^{15}$ [258]
	MWD 2.45 GHz, 1.5 – 3 kW, 121 × 21 × 15 cm^3	DLS	1.5 mbar; $Ar : H_2 : CH_4$; $Ar : H_2 : CH_4 : CH_3OH$; MPC 2.4 m; 948.232 cm^{-1}; $[NH_3] \sim 4 \times 10^{12} - 2 \times 10^{14}$ [221, 242]
	HFD 13.56 MHz, 3 – 13 W	FTIR	0.3 – 1 mbar, $N_2 + (0-5\%)H_2$; $[NH_3] \sim (0.5-3) \times 10^{13}$ [259]
SiH_2	DC tube l = 80 cm, D 3.6 cm, 20 – 40 W	CRDS, ICOS, ICLS	1 Torr SiH_4 and $SiH_4 : Ar$ (1 : 20); $[SiH_2] \sim (7-13) \times 10^9$ [260, 261]

Table 2 (continued)

Particle	Object*	Method**	Comment, concentrations [X], cm^{-3}
SiH_2, SiH_3	HFD 13.56 MHz, planar 0.6 W cm^{-2}	ICLS, CRDS	5 Pa, SiH_4(5 – 100%) : Ar(95 – 5%); $[SiH_2] \sim (2-9) \times 10^9$, $[SiH_3] \sim (2-8) \times 10^{11}$ [23]
SiH_3	ECRP, 2.45 GHz, 10 – 1000 W	CRDS	0.01 – 25 mTorr $SiH_4 : H_2$ (1 : 1); $[SiH_3] \sim (1-2) \times 10^{10}$ [23]
	APPJ jet from arc 45 A DC 1 atm	CRDS	Jet 0 – 20 mbar Ar : H_2 : SiH_4 (55 : 10 : x); $X^2A_1 - A^2A_1'$; 215 nm; at $x = (1-23)$ $[SiH_3] \sim (3-13) \times 10^{12}$ [262]
SiH_4	DBD, 50 × 50 × 2 mm^3, 0.11 W cm^{-2}	FTIR	1 atm Ar : NH_3(200 ppm) : SiH_4(60 ppm); 2186 cm^{-1}; optical path 50 mm; $[SiH_4] \sim (1-3) \times 10^{15}$; sensitivity $\sim 5 \times 10^{13}$ [258]
$SiCl_x$, SiF_x, $x = 1, 2$; SiClF	ICP, 13.56 MHz, 300(600) W + 90 W (bias), D 200 mm	WB AOS	$HBr/Cl_2/O_2/CF_4$; Si etching on Al_2O_3 substrate 5 – 20 mTorr, Xe lamp (200 – 400) nm; [. . .] $\sim 10^{10} - 6 \times 10^{12}$ [176, 233]
SiF_4	ICP, 1 kW, CW	DLS	7 mTorr CH_4(12) : (Ar, O_2, C_4F_8, H_2, N_2, CO)(2 – 8); SiCOH etching; $[SiF_4] \sim (1-3) \times 10^{13}$ [228]
	DF CCP (2 MHz + 60 MHz), 2 kW	DLS	0.333 mbar Ar : NF_3 (9 : 1); SiO_2 etching; QCL 1030 cm^{-1}; $[SiH_4] \sim (1-8) \times 10^{13}$ [263]
SF_6	DC, tube, $d = 10$ cm, D 1 cm, 1.5 – 5 W	DLS	1 – 20 mbar CO_2 – Ar(He); CO_2 pollutions; SF_6 is detected using absorption by metastable S atoms at 921.539 nm; in the range of $[CO_2]/[Ar] = (0-3) \times 10^{-3}$ sensitivity $[SF_6]/[CO_2] = (1-15) \times 10^{-6}$ [177]
H_2O_2	APPJ from capillary KinPen ID 1.5 mm, 1 MHz, 2 – 6 kV	FTIR	1 atm Ar + (0 – 0.017)%H_2O; MPC 19.2 m; 1250 – 1330 cm^{-1}; $[H_2O_2] \sim (0-12) \times 10^{13}$ [215]
	DBD 9 kV, 24 kHz	WB AOS, COMB	620 Torr, air + H_2O + H_2O_2; femtosecond laser as light source; MPC 18 m; $[H_2O_2] \sim 2.5 \times 10^{13} - 10^{16}$ [67]
HO_2	APPJ from HFD 1 MHz, 1 W	CRDS, OF-ICOS	1 atm Ar + H_2O(4 – 10%), 6638.2 cm^{-1}, $[HO_2] \sim (1-7) \times 10^{13}$; afterglow at 5.33 kPa $[HO_2] \sim 1.4 \times 10^{11}$; sensitivity $\sim 10^{10}$ [264]
	APPJ from capillary KinPen D 1.6 mm, 1 MHz	CRDS	1 atm Ar + H_2O(0.1%); 6638.2 cm^{-1}; $[HO_2] \sim (0.5-5) \times 10^{14}$; sensitivity $(6.5-1.5) \times 10^{10}$ [265]
	APPJ from AC discharge at 21.5 kHz into atmosphere	FR-CRDS	1 atm Ar : He (20 : 1), H_2O traces; in the measurement region, pressure is 30 Torr, induction $B = 694$ G; 6638.2 cm^{-1} $[HO_2] \sim 9.3 \times 10^{10}$; sensitivities $[HO_2] \sim 6.7 \times 10^7$ [98]
Molecules in excited electronic states			
$CN(B^2\Sigma)$	DC tube D 20 mm, 10 – 40 mA	ABS	2 – 8 Torr CO : N_2 : He : O_2 (1 : 2.5 : 10 : x), $x = 0 - 0.06$; cooling 300 K, 77 K; effect of radicals on CO laser operation; $[CN(B^2\Sigma)] \sim 4 \times 10^6 - 3 \times 10^9$ [220]
$C_2(a^3\Pi)$	Plasmotron 6.5 kW	CRDS	50 Torr Ar : H_2 : CH_4 (1.4 : 1.8 : 0.06); $[C_2(a^3\Pi, v = 0)] \sim 6 \times 10^{12} - 1.5 \times 10^{13}$ [224]
	Jet from arc 1.6 kW, 12 A	LIF	100 Pa, Ar : H_2 : CH_4 (1 : 0.9 : 0.005); excitation C_2(d – a), fluorescence 437 – 439 nm; $[C_2(a^3\Pi, v = 0)] \sim (1-6) \times 10^{10}$ [222]
$N_2(C^3\Pi)$	PD in tubes with diameters 1 – 5 cm; Pin–plane PD	ABS	0.1 Torr 1 atm air, N_2, 2^+ nitrogen, air system; at $P = 4$ Torr in ionization wave in range 5–20 ns, concentration is $[N_2(C^3\Pi)] \sim (0.02-1) \times 10^{11}$ [266]
$N_2(C^3\Pi, v = 0-4)$, $N_2(B^3\Pi, v = 1-4)$, $N_2(A^3\Sigma, v = 0-2)$	Planar PD	ABS	50 Torr N_2; 1^+ and 2^+ systems; population dynamics for 0 – 350 μs; afterglow for 350 – 1000 μs; $[N_2(C^3\Pi)] \sim 10^5 - 10^8$, $[N_2(B^3\Pi)] \sim 10^7 - 4 \times 10^9$; $[N_2(A^3\Sigma)] \sim (1-25) \times 10^{11}$ [267]
$N_2(A^3\Sigma, v = 0)$	HFD 433 MHz, 300 W, afterglow in tube D 3.8 cm	ICLS	1^+ system N_2 888 nm, Ti:Sa laser, effective absorption length 1.73 m $[N_2(A^3\Sigma)] \sim 10^9 - 5 \times 10^{11}$; sensitivity 10^9 cm^{-3} [219, 268, 269]
	PD 10 ns, 10 kHz, 5 – 8 kV	CRDS	1 atm of heated air or N_2, 1000 K; $N_2(A, v = 0-B, v = 2)$ 1^+ system; $[N_2(A^3\Sigma, v = 0)] = 10^{14} - 10^{15}$ [270]
$N_2(A^3\Sigma, v = 2-8)$	PD CO_2 laser, 8 μs	ICLS	CO_2 : N_2 : He; 240 Torr; 575 – 610 nm; in 1.6 μs after beginning of pulse $[N_2(A^3\Sigma, v = 2-8)] \sim (2-0.2) \times 10^{14}$ [24]
	Planar PD 100 ns, 0.2 – 0.3 mJ, 10 kHz	CRDS, DLS	22 – 132 Torr N_2, 752 – 768 nm; afterglow 0.1 – 2 ms; $[N_2(A^3\Sigma, v = 0-2)] \sim 10^{11} - 7 \times 10^{12}$ [271]

Table 2 (continued)

Particle	Object*	Method**	Comment, concentrations [X], cm^{-3}
$N_2(A^3\Sigma, v=0, 1, 3, 6)$	ICP, 100–300 W	ICOS	N_2 10–100 mTorr, 760 nm, 784 nm, 662 nm, $L_{eff} = 530-900$ m, $[N_2(A^3\Sigma, v = 0, 1, 3, 6)] \sim (5-130) \times 10^9$ [272]
$O_2(^1\Delta_g)$	HFD 13.56 MHz, 100 W, tube $d = 400$ mm, D 16 mm	ICLS	1.9 Torr O_2, afterglow; $^1\Delta_g(0)-b^1\Sigma_g^+(0)$, 1.908–1.911 μm; $[O_2(^1\Delta_g)] \sim (2-5) \times 10^{14}$ [24]
	MWD 2.37 GHz, 100 W, tube $d = 400$ mm, D 16 mm	ICLS	1.9 Torr O_2, afterglow; $^1\Delta_g(0)-b^1\Sigma_g^+(0)$, 1.908–1.911 μm; $[O_2(^1\Delta_g)] \sim 1.5 \times 10^{15}$ [273]
	MCSD with planar anode	ABS, WB AOS, TALIF	1 atm He + O_2(0–15 mbar) + NO(0–0.2 mbar); emission 1.27 μm; absorption 125–130 nm, H_2 lamp light source; $[O_2(^1\Delta_g)] \sim (1-15) \times 10^{15}$ [44, 274]
	APPJ from HFD 13.56 MHz, series 1–20 kHz, 50–400 mW	ABS	1 atm He : O_2(< 2%); emission 1.27 μm; $[O_2(^1\Delta_g)] \sim (1-3) \times 10^{14}$ [275]
	HFD 13.56 MHz, 270 W, tube $d = 0.8$ m, D 25 mm, afterglow	DLS, ICOS	20 Torr O_2 : He (1 : 10); $L_{eff} = 972$ m, $b^1\Sigma-a^1\Delta$, 1910 nm, $[O_2(^1\Delta_g)] \sim 3 \times 10^{15}$ sensitivity 2.5×10^{13} [276]
	APPJ from sources, 0.05–1 W: (1) RFD 13.56 MHz, (2) DBD ~ 10^4 Hz	ABS, WB AOS	1 atm He + (0–2)%O_2; emission 1.27 μm, absorption (124–130) nm, H_2 lamp light source; RFD — $[O_2(^1\Delta_g)]_j \sim 6.2 \times 10^{15}$, DBD — $[O_2(^1\Delta_g)] \sim 3 \times 10^{14}$ [277]
Molecular ions			
$N_2^+(B^2\Sigma)$	PD (1) in tubes D 1–5 cm; (2) pin–plane	ABS	0.1 Torr–1 atm N_2, air; 1^- system of N_2; spatiotemporal resolution; in N_2 at $P = 4$ Torr in ionization wave 5–20 ns $[N_2^+(B^2\Sigma)] \sim (0.2-2) \times 10^{10}$ [266]
$N_2^+(X^2\Sigma)$	APPJ from DBD in air, 5 kHz, tubes D 2–4 mm	LIF	1 atm He; excitation 391.4 nm, fluorescence 427.8 nm; radial dependences; Penning ionization; $[N_2^+(X^2\Sigma)] \sim 2 \times 10^{10}-3 \times 10^{11}$ [183]
	PD–HCD $d = 84$ cm, D 2 cm; 100–300 μs, 30 Hz, 400–600 V, 1.7–2.5 A	CRDS	1.1 Torr He : N_2 (1 : 0.1); cooling 77 K; $L_{eff} = 4.5-21$ km; transition $X^2\Sigma_g^+-A^2\Pi_u$ (6–0), 19,790 cm^{-1}; $[N_2^+(X^2\Sigma)] \sim 10^{11}$; sensitivity estimate $[N_2^+(X^2\Sigma)] \sim 10^9$ [278]
	Pin-to-pin DC, $l = 0.85$ cm, 52–187 mA	CRDS	1 atm N_2; $B^2\Sigma-X^2\Sigma$, 391 nm; radial dependences; $[N_2^+(X^2\Sigma)] \sim 10^{11}-3.5 \times 10^{12}$ [279]
$N_2^+(X^2\Sigma)$	ICP, 400 W	ICOS	N_2 10 mTorr, $X^2\Sigma_g^+-A^2\Pi_u$ (2–0) 785 nm, $L_{eff} = 660$ m, $[N_2^+(X^2\Sigma), v = 0] \sim 2.7 \times 10^9$ [272]
ArH^+	DC tube $l = 2$ m, $d = 2.1$ cm, 60 kW	DLS	1–10 Torr; Ar : H_2 (30 mTorr); 2525.475 cm^{-1}, 2525.414 cm^{-1}; $[ArH^+] \sim 10^{11}-5 \times 10^{12}$ [280]
H_3^+	DC tube $l = 2$ m, $d = 2.1$ cm, 60 kW	DLS	0.55–1.15 mTorr H_2, wall cooling 77 K; radial dependences; 2529.724 cm^{-1}; $[H_3] \sim 7 \times 10^{11}$ [280]
NO_3^-	AC discharge if air flow between needle array and water surface. $l = 3.5$ mm, 8.8 kV, 7.6 kHz, 105 W, afterglow	FTIR	Air 1 atm, 304 nm, $[NO_3^-] \sim 2 \times 10^{15}-1.5 \times 10^{17}$; liquid surface activation by plasma (PWA) [281]

* Objects of study, plasma and light sources.
DC — direct current; PD — pulse discharge; CVD — chemical vapor deposition; MWD — microwave discharge; HFD — high frequency discharge; HCD — hollow cathode discharge; MHCD — micro hollow cathode discharge; ICP — inductively coupled plasma; ECRP — electron cyclotron resonance plasma; CCD — charge coupled device; SWD — surface wave discharge, DBD — dielectric barrier discharge; APPJ — atmospheric pressure plasma jet; TS — terahertz spectroscopy; DF CCP — double frequency capacitively coupled plasma.
** Measurements (methods).
ACT — actinometry; AOS — absorption optical spectroscopy; WB AOS (wideband absorption optical spectroscopy) — absorption in continuum; L–L — line absorption; LIF — laser-induced fluorescence; TALIF — two-photon absorption laser induced fluorescence; XRIF — X-ray induced fluorescence; ABS — absolute intensities; LIPS — laser-induced polarization spectroscopy; OES — optical emission spectroscopy; DLS (diode laser spectroscopy) — spectroscopy using traditional DLs and quantum cascade lasers (QCLs); COMB — spectrum of a short laser pulse; REMPI — resonance-enhanced multiphoton ionization; Radar — resonance multiphoton ionization (with microwave scattering); (D)FWM(PS) — (degenerate) four-wave mixing (polarization) spectroscopy; (RE)CARS — (resonance) coherent anti-Stokes scattering; ICLS — intracavity laser spectroscopy; ICOS — integrated cavity output spectroscopy; OF ICOS — optical feedback integrated cavity output spectroscopy; FR (Faraday rotation) — spectroscopy of polarization rotation in a magnetic field.

available, technology to the field of plasma research is in full accordance with the general trends in spectroscopy, in which prism optics was gradually replaced by diffraction optics, and then by broadband Fourier interferometry and crossed systems. In essence, the technique of combs using lasers with ultrashort pulses is a promising line of development in Fourier spectroscopy on a new basis, which takes on the tasks of analyzing multicomponent plasma.

It is important to ascertain that the emergence of new experimental methods, the expansion of databases on elementary processes, and the development of plasma simulation methods contributed to the fact that the classical

methods of quantitative spectroscopy have also reached a qualitatively new level. New light sources for absorption spectroscopy based on discharges with miniature hollow cathodes and LEDs are being developed and applied, and VUV and X-ray plasma spectroscopy using synchrotron radiation is entering the practice. Hundreds of atoms, two- and polyatomic particles in ground and excited states, and their ions have become available for monitoring. Experience shows that by now the contributions of laser and classical methods to plasma spectroscopy are quite comparable, and these groups of methods are mutually complementary.

The author is grateful to A V Bernatsky, I V Kochetov, and V V Lagunov for their collaboration and participation in preparing this review. The work was carried out with the aid of the Russian Science Foundation, project no. 19-12-00310.

References

1. Fortov V E (Ed.-in-Chief), Ochkin V N (Exec. Ed.) *Entsiklopediya Nizkotemperaturnoi Plazmy Ser. B Spravochnye Prilozheniya, Bazy i Banki Dannykh* (Encyclopedia of Low-Temperature Plasma Ser. B Reference Applications, Databases and Databanks) Vol. 3-2 *Termodinamicheskie, Opticheskie i Transportnye Svoistva Nizkotemperaturnoi Plazmy* (Thermodynamic, Optical and Transport Properties of Low-Temperature Plasma) Pt. 1 *Opticheskie Svoistva Nizkotemperaturnoi Plazmy* (Optical Properties of Low-Temperature Plasma) (Moscow: Yanus-K, 2008) p. 1
2. Lochte-Holtgreven W (Ed.) *Plasma Diagnostics* (Amsterdam: North-Holland, 1968)
3. Prokhorov A M (Ed.-in-Chief) *Fizicheskii Entsiklopedicheskii Slovar'* (Physical Encyclopedic Dictionary) (Moscow: Sov. Entsiklopediya, 1984)
4. Artsimovich L A, Sagdeev R Z *Fizika Plazmy dlya Fizikov* (Plasma Physics for Physicists) (Moscow: Atomizdat, 1979)
5. Bernatskiy A V, Kochetov I V, Ochkin V N *Plasma Phys. Rep.* **46** 874 (2020); *Fiz. Plazmy* **46** 783 (2020)
6. Griem H R *Plasma Spectroscopy* (New York: McGraw-Hill, 1964)
7. Thorne A, Litzén U, Johansson S *Spectrophysics*: *Principles and Applications* (Berlin: Springer, 1999)
8. Fujimoto T *Plasma Spectroscopy* (Oxford: Clarendon Press, 2004)
9. Frish S E (Exec. Ed.) *Spektroskopiya Gazorazryadnoi Plazmy* (Spectroscopy of Gas-Discharge Plasma) (Leningrad: Nauka, 1970)
10. Slovetskii D I *Mekhanizmy Khimicheskikh Reaktsii v Neravnovesnoi Plazme* (Mechanisms of Chemical Reactions in Nonequilibrium Plasma) (Moscow: Nauka, 1980)
11. Ochkin V N *Spectroscopy of Low Temperature Plasma* (Weinheim: Wiley-VCH Verlag, 2009)
12. Fantz U *Plasma Sources Sci. Technol.* **15** S137 (2006)
13. Chen F F, Chang J P *Lecture Notes on Principles of Plasma Processing* (New York: Kluwer Acad., Plenum Publ., 2003)
14. Engeln R, Klarenaar B, Guaitella O *Plasma Sources Sci. Technol.* **29** 063001 (2020)
15. Peverall R, Ritchie G A D *Plasma Sources Sci. Technol.* **28** 073002 (2019)
16. Lange H, Bussiahn R *Proc. SPIE* **4460** 177 (2002)
17. Reuter S et al. *Plasma Sources Sci. Technol.* **24** 054001 (2015)
18. Lu X et al. *Phys. Rep.* **630** 1 (2016)
19. Reuter S, von Woedtke T, Weltmann K-D *J. Phys. D* **51** 233001 (2018)
20. Iseki S et al. *Appl. Phys. Express* **4** 116201 (2011)
21. Zhang K et al. *Crit. Rev. Food Sci. Nutr.* **59** 812 (2019)
22. Röpcke J et al. *Plasma Sources Sci. Technol.* **15** S148 (2006)
23. Hori M, Goto T *Appl. Surf. Sci.* **192** 135 (2002)
24. Podmar'kov Yu P, Raspopov N A, Frolov M P *Proc. SPIE* **4460** 188 (2002)
25. Wang C *J. Anal. At. Spectrom.* **22** 1347 (2007)
26. Maity A, Maithani S, Pradhan M *Anal. Chem.* **93** 388 (2021)
27. Ochkin V N et al. *IEEE Trans. Plasma Sci.* **26** 1502 (1998)
28. Kiefer J, Ewart P *Prog. Energy Combust. Sci.* **37** 525 (2011)
29. Wiese W L, Smith M W, Miles B M, in *Atomic Transition Probabilities* Vol. 2 *Sodium through Calcium. A Critical Data Compilation* (NSRDS-NBS, 22) (Washington, DC: US Department of Commerce, National Bureau of Standards, 1969)
30. Ochkin V N, Savinov S Yu, Sobolev N N, in *Electron-Excited Molecules in Nonequilibrium Plasma* (Eds N N Sobolev) (Commack, NY: Nova Science Publ., 1989) p. 7
31. Herzberg G *Molecular Spectra and Molecular Structure* 1. *Spectra of Diatomic Molecules* (New York: Van Nostrand, 1951)
32. Herzberg G *Molecular Spectra and Molecular Structure* Vol. 2 *Infrared and Raman Spectra of Polyatomic Molecules* (New York: Prentice-Hall, 1945); Translated into Russian: *Kolebatel'nye i Vrashchatel'nye Spektry Mnogoatomnykh Molekul* (Vibrational and Rotational Spectra of Polyatomic Molecules) (Moscow: IL, 1949)
33. Glushko V P (Exec. Ed.) *Termodinamicheskie Svoistva Individual'nykh Veshchestv* (Thermodynamic Properties of Individual Substances) (Moscow: Nauka, 1978)
34. Mikaberidze A A, Ochkin V N, Sobolev N N *J. Quant. Spectrosc. Radiat. Transf.* **12** 169 (1972)
35. Letokhov V S (Exec. Ed.) *Lazernaya Analiticheskaya Spektroskopiya* (Laser Analytical Spectroscopy) (Moscow: Nauka, 1986)
36. Kopylov S M et al. *Perestraivaemye Lazery na Krasitelyakh i Ikh Primeneniya* (Tunable Dye Lasers and Their Applications) (Moscow: Radio i Svyaz', 1991)
37. Witteman W J *Detection and Signal Processing*: *Technical Realization* (Berlin: Springer, 2006)
38. Ochkin V N *Plasma Phys. Rep.* **41** 350 (2015); *Fiz. Plazmy* **41** 381 (2015)
39. Mitchell A C G, Zemansky M W *Resonance Radiation and Excited Atoms* (Cambridge: The Univ. Press, 1934); Translated into Russian: *Rezonansnoe Izluchenie i Vozbuzhdennye Atomy* (Moscow: GTTL, 1937)
40. Gerasimov G N et al. *Sov. Phys. Usp.* **35** 400 (1992); *Usp. Fiz. Nauk* **162** (5) 123 (1992)
41. Lebedeva V V, in *Entsiklopediya Nizkotemperaturnoi Plazmy Ser. B Spravochnye Prilozheniya, Bazy i Banki Dannykh* (Encyclopedia of Low-Temperature Plasma Ser. B Reference Applications, Databases and Databanks) Vol. 3-2 *Termodinamicheskie, Opticheskie i Transportnye Svoistva Nizkotemperaturnoi Plazmy* (Thermodynamic, Optical and Transport Properties of Low-Temperature Plasma) Pt. 1 *Opticheskie Svoistva Nizkotemperaturnoi Plazmy* (Optical Properties of Low-Temperature Plasma) (Ed.-in-Chief V E Fortov, Exec. Ed. V N Ochkin) (Moscow: Yanus-K, 2008) p. 469
42. Lomaev M I et al. *Phys. Usp.* **46** 193 (2003); *Usp. Fiz. Nauk* **173** 201 (2003)
43. Hori M, Kondo H, Hiramatsu M *J. Phys. D* **44** 174027 (2011)
44. Sousa J S, Puech V *J. Phys. D* **46** 464005 (2013)
45. Ogurtsova N N, Podmoshenskii I V, in *Nizkotemperaturnaya Plazma. Trudy Mezhdunarodnogo Simpoziuma po Svoistvam i Primeneniyu Nizkotemperaturnoi Plazmy pri XX Mezhdunarodnom Kongresse po Teoreticheskoi i Prikladnoi Khimii, Moskva, Iyul' 15–17, 1965* (Low-Temperature Plasma. Proc. of the Intern. Symp. on Properties and Applications of Low-Temperature Plasma at the 20th Intern. Congress of Theoretical and Applied Chemistry, Moscow, July 15–17, 1965) (Ed. A E Sheindlin) (Moscow: Mir, 1967) p. 432
46. Mit'ko S V et al. *Kr. Soobshch. Fiz. FIAN* (11) 47 (1989)
47. Wang H et al. *J. Phys. D* **51** 035203 (2018)
48. Kern C et al. *Appl. Opt.* **45** 2077 (2006)
49. Ternov I M *Phys. Usp.* **38** 409 (1995); *Usp. Fiz. Nauk* **165** 429 (1995)
50. Dedrick J et al. *J. Phys. D* **50** 455204 (2017)
51. Hall J L *Rev. Mod. Phys.* **78** 1279 (2006)
52. Udem Th, Holzwarth R, Hänsch T W *Nature* **416** 233 (2002)
53. Zheltikov A M *Phys. Usp.* **49** 605 (2006); *Usp. Fiz. Nauk* **176** 623 (2006)
54. Bagaev S N, Chebotaev V P *Sov. Phys. Usp.* **29** 82 (1986); *Usp. Fiz. Nauk* **148** 143 (1986)
55. Adler F et al. *Annu. Rev. Anal. Chem.* **3** 175 (2010)
56. Gotti R et al. *J. Chem. Phys.* **148** 054202 (2018)
57. Picqué N, Hänsch T W *Nat. Photon.* **13** 146 (2019)
58. Griffiths P R, de Haseth J A *Fourier Transform Infrared Spectrometry* (Hoboken, NJ: Wiley-Interscience, 2007)
59. Telle H R et al. *Appl. Phys. B* **69** 327 (1999)
60. Zimmermann M et al. *Opt. Lett.* **29** 310 (2004)

61. Dianov E M Kryukov P G *Quantum Electron.* **31** 877 (2001); *Kvantovaya Elektron.* **31** 877 (2001)
62. Schliesser A, Picqué N, Hänsch T W *Nat. Photon.* **6** 440 (2012)
63. Weichman M L et al. *J. Mol. Spectrosc.* **355** 66 (2019)
64. Link S M et al. *Science* **356** 1164 (2017)
65. Shelton R K et al. *Science* **293** 1286 (2001)
66. Niermann B et al. *J. Phys. D* **45** 245202 (2012)
67. Golkowski M et al. *IEEE Trans. Plasma Sci.* **40** 1984 (2012)
68. Durocher-Jean A et al. *J. Phys. D* **54** 085204 (2021)
69. Murnick D E, Peer B J *Science* **263** 945 (1994)
70. Chernin S M *J. Mod. Opt.* **48** 619 (2001)
71. Pakhomycheva L A et al. *JETP Lett.* **12** 43 (1970); *Pis'ma Zh. Eksp. Teor. Fiz.* **12** 60 (1970)
72. Baev V M, Latz T, Toshek P E *Appl. Phys. B* **69** 171 (1999)
73. Ochkin V N, Raspopov N A, in *Entsiklopediya Nizkotemperaturnoi Plazmy. Vvodnyi Tom* (Encyclopedia of Low-Temperature Plasma. Introductory Volume) Book 2 (Ed.-in-Chief V E Fortov, Comp. Ed. A F Aleksandrov et al.) (Moscow: Nauka, 2000) p. 583
74. Crosson E R et al. *Anal. Chem.* **74** 2003 (2002)
75. Nikolaev I V et al. *Spectrochim. Acta A* **66** 832 (2007)
76. Lagunov V V, Nikolaev I V, Ochkin V N *Spectrochim. Acta A* **246** 119060 (2021)
77. Anevskii S I et al., in *Entsiklopediya Nizkotemperaturnoi Plazmy. Vvodnyi Tom* (Encyclopedia of Low-Temperature Plasma. Introductory Volume) Book 2 (Ed.-in-Chief V E Fortov, Comp. Ed. A F Aleksandrov et al.) (Moscow: Nauka, 2000) p. 532
78. Oda T, Ono R *Proc. SPIE* **4460** 263 (2002)
79. Salmon J T, Laurendeau N M *Appl. Opt.* **26** 2881 (1987)
80. Andresen P et al. *Appl. Opt.* **27** 365 (1988)
81. Niemi K, Schulz-von der Gathen V, Döbele H F *J. Phys. D* **34** 2330 (2001)
82. Doebele H F, Niemi K, Sculz-von der Gathen V, in *Proc. of the X Intern. Conf. on Laser-Aided Plasma Diagnostics, Fukuoka, Japan, 2001*, p. 71
83. Elliott D, Scime E, Short Z *Rev. Sci. Instrum.* **87** 11E504 (2016)
84. Curry J J et al., in *Proc. of the X Intern. Conf. on Laser-Aided Plasma Diagnostics, Fukuoka, Japan, 2001*, p. 362
85. Ochkin V N et al. *Sov. Phys. Usp.* **29** 260 (1986); *Usp. Fiz. Nauk* **148** 473 (1986)
86. Ochkin V N, Preobrazhensky N G, Shaparev N Ya *Optogalvanic Effect in Ionized Gas* (London–Moscow–Amsterdam: Lebedev Physical Institute. Foundation for Intern. Scientific and Education Cooperation, distributed by Gordon and Breach, 1999)
87. Aleksandrov N L, Napartovich A P *Phys. Usp.* **36** 107 (1993); *Usp. Fiz. Nauk* **163** (3) 1 (1993)
88. Lebedev V S, Presnyakov L P, Sobel'man I I *Phys. Usp.* **46** 473 (2003); *Usp. Fiz. Nauk* **173** 491 (2003)
89. Shibagaki K, Sasaki K *J. Phys. D* **41** 195204 (2008)
90. Kim M *AIP Scilight* **21** (2019) https://doi.org/10.1063/1.5110720
91. Wu Y, Zhang Z *Appl. Opt.* **54** 157 (2015)
92. Landsberg G S *Optika* (Optics) (Moscow: Nauka, 1976)
93. Kronig R de L *J. Opt. Soc. Am.* **12** 547 (1926)
94. Kramers H A *Atti Congresso Int. Fisici, Como* (*Trans. Volta Centenary Congress, Como*) **2** 545 (1927)
95. Kirzhnits D A *Sov. Phys. Usp.* **30** 575 (1987); *Usp. Fiz. Nauk* **152** 399 (1987)
96. Engeln R et al. *J. Chem. Phys.* **107** 4458 (1997)
97. Westberg J, Wysocki G *Appl. Phys. B* **123** 168 (2017)
98. Gianella M et al. *J. Chem. Phys.* **151** 124202 (2019)
99. Miles R B, Lempert W R, Forkey J N *Meas. Sci. Technol.* **12** R33 (2001)
100. Boyd R W *Nonlinear Optics* (Boston: Academic Press, 1992)
101. Akhmanov S A, Koroteev N I *Metody Nelineinoi Optiki v Spektroskopii Rasseyaniya Sveta*: *Aktivnaya Spektroskopiya Rasseyaniya Sveta* (Nonlinear Optics Methods in Light Scattering Spectroscopy: Active Light Scattering Spectroscopy) (Moscow: Nauka, 1981)
102. Zhivotov V K, Rusanov V D, Fridman A A *Diagnostika Neravnovesnoi Khimicheski Aktivnoi Plazmy* (Diagnostics of Non-Equilibrium Chemically Active Plasma) (Moscow: Energoatomizdat, 1985)
103. Kiefer J, Ewart P *Prog. Energy Combust. Sci.* **37** 525 (2011)
104. Eckbreth A C *Laser Diagnostics for Combustion Temperature and Species* (Amsterdam: Gordon and Breach, 1996)
105. Schrötter H W, Klöckner H W, in *Raman Spectroscopy of Gases and Liquids* (Topics in Current Physics, Vol. 11, Ed. A Weber) (Berlin: Springer-Verlag, 1979) p. 123; Translated into Russian, in *Spektroskopiya Kombinatsionnogo Rasseyaniya v Gazakh i Zhidkostyakh* (Ed. A Weber) (Moscow: Mir, 1982) p. 154
106. Regnier P R, Moya F, Taran J P E *AIAA J.* **12** 826 (1974)
107. Prior Y *Appl. Opt.* **19** 1741 (1980)
108. Nibler J W, Knighten G V, in *Raman Spectroscopy of Gases and Liquids* (Topics in Current Physics, Vol. 11, Ed. A Weber) (Berlin: Springer-Verlag, 1979) p. 253; Translated into Russian, in *Spektroskopiya Kombinatsionnogo Rasseyaniya v Gazakh i Zhidkostyakh* (Ed. A Weber) (Moscow: Mir, 1982) p. 310
109. Massabieaux B et al. *J. Phys. France* **48** 1939 (1987)
110. Péalat M et al. *J. Chem. Phys.* **82** 4943 (1985)
111. Doerk T et al. *Opt. Commun.* **118** 637 (1995)
112. Ono R *J. Phys. D* **49** 083001 (2016)
113. Stauffer H U et al. *J. Chem. Phys.* **145** 124308 (2016)
114. Ochkin V N, Tskhai S N *Phys. Usp.* **46** 1214 (2003); *Usp. Fiz. Nauk* **173** 1253 (2003)
115. Tskhai S N et al. *J. Raman Spectrosc.* **32** 177 (2001)
116. van der Schans M et al. *Plasma Sources Sci. Technol.* **26** 115006 (2017)
117. Goldberg B M et al. *Plasma Sources Sci. Technol.* **25** 045008 (2016)
118. Abrams R L, Lind R C *Opt. Lett.* **2** 94 (1978)
119. Lucht R P, Farrow R L, Rakestraw D J *J. Opt. Soc. Am. B* **10** 1508 (1993)
120. Smith A P, Astill A G *Appl. Phys. B* **58** 459 (1994)
121. Tsay S J et al. *Opt. Lett.* **20** 1725 (1995)
122. Nyholm K, Kaivola M, Aminoff C G *Opt. Commun.* **107** 406 (1994)
123. Germann G J, Rakestraw D J *Science* **264** 1750 (1994)
124. Reichardt T A et al. *Appl. Opt.* **38** 6951 (1999)
125. Mischler B et al. *Combust. Sci. Technol.* **119** 375 (1996)
126. Williams S et al. *J. Am. Chem. Soc.* **114** 9122 (1992)
127. Walewski J et al. *Phys. Rev. A* **64** 063816 (2001)
128. Reichardt T A, Giancola W C, Lucht R P *Appl. Opt.* **39** 2002 (2000)
129. Alwahabi Z T et al. *Eur. Phys. J. D* **42** 41 (2007)
130. Sun Z W et al. *Appl. Phys. B* **101** 423 (2010)
131. Pikalov V V, in *Entsiklopediya Nizkotemperaturnoi Plazmy. Vvodnyi Tom* (Encyclopedia of Low-Temperature Plasma. Introductory Volume) Book 2 (Ed.-in-Chief V E Fortov, Comp. Ed. A F Aleksandrov et al.) (Moscow: Nauka, 2000) p. 563
132. Biberman L M, Vorob'ev V S, Yakubov I T *Kinetics of Nonequilibrium Low-Temperature Plasmas* (New York: Consultants Bureau, 1987); Translated from Russian: *Kinetika Neravnovesnoi Nizkotemperaturnoi Plazmy* (Moscow: Nauka, 1982)
133. Lebedeva V V *Tekhnika Opticheskoi Spektroskopii* (Technique of Optical Spectroscopy) (Moscow: Izd. Mosk. Univ., 1977)
134. Pikalov V V, Mel'nikova T S *Tomografiya Plazmy* (Plasma Tomography) (Novosibirsk: Nauka, 1995)
135. Fujimoto T, Kazantsev S A *Plasma Phys. Control. Fusion* **39** 1267 (1997)
136. Bergert R, Mitic S *Plasma Sources Sci. Technol.* **28** 115001 (2019)
137. Ochkin V N, Savinov S Yu, Sobolev N N, in *Electron-Excited Molecules in Nonequilibrium Plasma* (Proc. of the Lebedev Physics Institute of the Academy of Sciences of the USSR, Vol. 179, Suppl. 2, Ed. N N Sobolev) (Commack, NY: Nova Science Publ., 1989); Translated from Russian, in *Elektronno-vozbuzhdennye Molekuly v Neravnovesnoi Plazme* (Trudy Fizicheskogo Instituta im. P.N. Lebedeva, Vol. 157, Exec. Ed. N N Sobolev) (Moscow: Nauka, 1985) p. 6
138. Bernatskiy A V et al. *Plasma Phys. Rep.* **41** 705 (2015); *Fiz. Plazmy* **41** 767 (2015)
139. Behringer K, Fantz U *New J. Phys.* **2** 23 (2000)
140. Wünderlich D, Fantz U *Atoms* **4** (4) 26 (2016)
141. Friedl R et al. *Plasma Sources Sci. Technol.* **29** 015014 (2020)
142. Polak L S et al., in *Eksperimental'nye i Teoreticheskie Issledovaniya Neravnovesnykh Fiziko-khimicheskikh Protsessov* (Experimental and Theoretical Study of Non-Equilibrium Physical and Chemical Processes) Issue 2 (Exec. Ed. L S Polak) (Moscow: Inst. Neftekhim. Sinteza im. A.V. Topchieva, 1974) p. 188
143. Polak L S *Neravnovesnaya Khimicheskaya Kinetika i Ee Primenenie* (Nonequilibrium Chemical Kinetics and Its Applications) (Moscow: Nauka, 1979)

144. Coburn J W, Chen M *J. Appl. Phys.* **51** 3134 (1980)
145. Bernatskiy A V, Ochkin V N, Kochetov I V *J. Phys. D* **49** 395204 (2016)
146. Lavrov B P et al. *Plasma Sources Sci. Technol.* **12** 576 (2003)
147. Filippov A V et al. *Proc. SPIE* **4450** 285 (2002)
148. Takashima S et al. *Appl. Phys. Lett.* **75** 2520 (1999)
149. Takeuchi W et al. *J. Appl. Phys.* **105** 113305 (2009)
150. Bokor J et al. *Phys. Rev. A* **24** 612 (1981)
151. Magee R M et al. *Rev. Sci. Instrum.* **83** 10D701 (2012)
152. Kulatilaka W D et al. *Combust. Flame* **137** 523 (2004)
153. Cho D G, Han J, Moon S Y *Appl. Phys.* **20** 550 (2020)
154. Bernatskiy A V, Ochkin V N *Plasma Sources Sci. Technol.* **26** 015002 (2017)
155. Elliott D et al. *Rev. Sci. Instrum.* **87** 11E506 (2016)
156. Galante M E, Magee R M, Scime E E *Phys. Plasmas* **21** 055704 (2014)
157. Lopaev D V et al. *J. Phys. D* **50** 075202 (2017)
158. Proshina O V et al. *Plasma Sources Sci. Technol.* **26** 075005 (2017)
159. Ibbotson D E, Flamm D L, Donnelly V M *J. Appl. Phys.* **54** 5974 (1983)
160. Hamann S et al. *Plasma Sources Sci. Technol.* **23** 045015 (2014)
161. Rayar M et al. *J. Appl. Phys.* **104** 033304 (2008)
162. Ivanov V V et al. *Plasma Phys. Rep.* **26** 980 (2000); *Fiz. Plazmy* **26** 1046 (2000)
163. Takeda K et al. *J. Phys. D* **46** 464006 (2013)
164. Gessel A F H, Grootel S C, Bruggeman P J *Plasma Sources Sci. Technol.* **22** 055010 (2013)
165. Teslja A, Dagdigian P J *Chem. Phys. Lett.* **400** 374 (2004)
166. Takeda K et al. *J. Phys. D* **52** 165202 (2019)
167. Gragston M et al. *J. Appl. Phys.* **125** 203301 (2019)
168. Reuter S et al. *Plasma Sources Sci. Technol.* **21** 024005 (2012)
169. Sirotkin N A, Khlyustova A V, Titov V A *Plasma Chem. Plasma Process.* **40** 187 (2020)
170. Flikweert A J "Spectroscopy on metal-halide lamps under varying gravity conditions", PhD Thesis (Eindhoven: Technische Univ. Eindhoven, 2008)
171. Tada S et al. *J. Appl. Phys.* **88** 1756 (2000)
172. Mazouffre S et al. *Plasma Sources Sci. Technol.* **10** 168 (2001)
173. Kuwano K et al. *J. Appl. Phys.* **55** 086101 (2016)
174. Lelevkin V M, Otorbaev D K, Schram D C *Physics of Non-Equilibrium Plasmas* (Amsterdam: North-Holland, 1992)
175. Schwabedissen A et al. *J. Phys. D* **34** 1116 (2001)
176. Kogelschatz M, Cunge G, Sadeghi N *J. Phys. D* **37** 1954 (2004)
177. Franzke J, Stancu D G, Niemax K *Spectrochim. Acta B* **58** 1359 (2003)
178. Aramaki M et al. *Jpn. J. Appl. Phys.* **44** 6759 (2005)
179. Rousseau A, Teboul E, Sadeghi N *Plasma Sources Sci. Technol.* **13** 166 (2004)
180. Wu S et al. *Jpn. J. Appl. Phys.* **52** 071301 (2013)
181. Benedikt J et al. *J. Appl. Phys.* **94** 6932 (2003)
182. Arkhipenko V I, Simonchik L V *Proc. SPIE* **4450** 1 (2002)
183. Urabe K et al. *J. Phys. D* **43** 095201 (2010)
184. Cadot G et al. *IEEE Trans. Plasma Sci.* **42** 10 (2014)
185. Winter J et al. *Plasma Sources Sci. Technol.* **24** 025015 (2015)
186. Niermann B et al. *Eur. Phys. J. D* **60** 489 (2010)
187. Ferreira C M, Tatarova E *Proc. SPIE* **4450** 99 (2002)
188. Schroter S et al. *J. Phys. D* **46** 464009 (2013)
189. Es-sebbar Et et al. *J. Appl. Phys.* **126** 073302 (2019)
190. Gazeli K et al. *Plasma Sources Sci. Technol.* **27** 065003 (2018)
191. Hoskinson A R et al. *J. Appl. Phys.* **119** 233301 (2016)
192. Modiano S H et al. *Appl. Opt.* **35** 21 (1996)
193. Hubner S et al. *J. Appl. Phys.* **113** 143306 (2013)
194. Kaupe J, Coenen D, Mitic S *Plasma Sources Sci. Technol.* **27** 105003 (2018)
195. Penache M C "Study of high-pressure glow discharges generated by micro-structured electrode (MSE) arrays", Dissertation zur Erlangung des Doktorgrades der Naturwissenschaften (Frankfurt am Main: Univ. in Frankfurt am Main, 2002)
196. Makabe T *J. Phys. D* **52** 213002 (2019)
197. Quandt E, Kraemer I, Dobele H F *Europhys. Lett.* **45** 32 (1998)
198. Quandt E et al. *Appl. Phys. Lett.* **72** 2394 (1998)
199. Grangeon F et al. *Plasma Sources Sci. Technol.* **8** 448 (1999)
200. Pandey A et al. *Plasma Phys. Control. Fusion* **61** 065003 (2019)
201. Fantz U, Wünderlich D *New J. Phys.* **8** 301 (2006)
202. Agnello R et al. *Nucl. Fusion* **60** 026007 (2020)
203. Ohkubo T et al. *Proc. SPIE* **4450** 318 (2002)
204. Welzel S et al. *Plasma Sources Sci. Technol.* **20** 015020 (2011)
205. Kulatilaka W D et al. *Opt. Lett.* **31** 3357 (2006)
206. Pipa A V et al. *J. Phys. D* **41** 194011 (2008)
207. Pipa A V et al. *J. Phys. D* **45** 085201 (2012)
208. Smith J A et al. *J. Appl. Phys.* **92** 672 (2002)
209. Lempert W R *Combust. Flame* **73** 89 (1988)
210. Hibert C et al. *J. Appl. Phys.* **85** 7070 (1999)
211. Dilecce G et al. *J. Phys. D* **45** 125203 (2012)
212. Martini L M et al. *Plasma Process. Polym.* **11** 232 (2014)
213. Ochkin V N, Savinov S Yu, Sobolev N N *J. Appl. Spectrosc.* **26** 647 (1977); *Zh. Prikl. Spektrosk.* **26** 900 (1977)
214. Verreycken T et al. *J. Phys. D* **46** 464004 (2013)
215. Winter H T et al. *J. Phys. D* **47** 285401 (2014)
216. Verreycken T et al. *Plasma Sources Sci. Technol.* **22** 055014 (2013)
217. Wang C et al. *Appl. Spectrosc.* **58** 734 (2004)
218. Kim S et al. *Meas. Sci. Technol.* **14** 1662 (2003)
219. Li Z S et al. *Opt. Lett.* **33** 1836 (2008)
220. Trubacheev E A, in *Gazovye Lazery i Ikh Primenenie* (Gas Lasers and Their Applications) (Proc. of the Lebedev Physical Institute, Vol. 102, Exec. Ed. N N Sobolev) (Moscow: Nauka, 1977) p. 3
221. Hempel F et al. *Mol. Phys.* **101** 589 (2003)
222. Luque J, Juchmann W, Jeffries J B *J. Appl. Phys.* **82** 2072 (1997)
223. Juchmann W, Luque J, Jeffries J B *Appl. Opt.* **39** 3704 (2000)
224. Wills J B et al. *J. Appl. Phys.* **92** 4213 (2002)
225. Engeln R et al. *Chem. Phys. Lett.* **310** 405 (1999)
226. Booth J-P et al. *Plasma Sources Sci. Technol.* **29** 115009 (2020)
227. Busch C, Moller I, Soltwisch H *Plasma Sources Sci. Technol.* **10** 250 (2001)
228. Zimmermann S et al. *Microelectron. Eng.* **88** 671 (2011)
229. Hempel F et al. *Plasma Sources Sci. Technol.* **21** 055001 (2012)
230. Hamann S et al. *Plasma Sources Sci. Technol.* **22** 055022 (2013)
231. Puth A et al. *Plasma Sources Sci. Technol.* **29** 035001 (2020)
232. Susuki C, Sasaki K, Kadota K *Jpn. J. Appl. Phys.* **37** 5763 (1998)
233. Cunge G, Kogelschatz M, Sadeghi N *Plasma Sources Sci. Technol.* **13** 522 (2004)
234. Lang N et al. *Jpn. J. Appl. Phys.* **50** 08JB04 (2011)
235. Bernatskiy A V, Lagunov V V, Ochkin V N *Phys. At. Nucl.* **82** 1382 (2019); *Yad. Fiz. Inzh.* **10** 151 (2019)
236. Bernatskiy A V, Lagunov V V, Ochkin V N *Quantum Electron.* **49** 157 (2019); *Kvantovaya Elektron.* **49** 157 (2019)
237. Lopatik D et al. *Contrib. Plasma Phys.* **52** 864 (2012)
238. Vinogradov I P, Dinkelmann A, Lunk A *J. Phys. D* **37** 3000 (2004)
239. Hubner M et al. *Appl. Phys. Lett.* **106** 031102 (2015)
240. Marinov D et al. *J. Phys. D* **45** 175201 (2012)
241. Kerimkulov M A et al. *JETP Lett.* **54** 208 (1991); *Pis'ma Zh. Eksp. Teor. Fiz.* **54** 212 (1991)
242. Hempel F et al. *Plasma Sources Sci. Technol.* **12** S98 (2003)
243. Ropcke J et al. *Plasma Chem. Plasma Process.* **19** 395 (1999)
244. Lombardi G et al. *Plasma Sources Sci. Technol.* **13** 27 (2004)
245. Mechold L et al. *Plasma Sources Sci. Technol.* **10** 52 (2001)
246. Wu Y et al. *Appl. Phys. B* **111** 391 (2013)
247. Sick V, Bui-Pham M N, Farrow R L *Opt. Lett.* **20** 2036 (1995)
248. Ouaras K, Righetti F, Cappelli M A *J. Phys. D* **52** 195202 (2019)
249. Penetrante B M et al. *Plasma Sources Sci. Technol.* **6** 251 (1997)
250. Kim Y et al. *Appl. Phys. Lett.* **87** 011502 (2005)
251. Winter J et al. *J. Phys. D* **45** 385201 (2012)
252. Schulz-von der Gathen V et al. *Contrib. Plasma Phys.* **47** 510 (2007)
253. Ono R, Oda T *J. Phys. D* **37** 730 (2004)
254. Reuter S et al. *Plasma Sources Sci. Technol.* **21** 034015 (2012)
255. Moiseev T et al. *Plasma Sources Sci. Technol.* **23** 065033 (2014)
256. Schmidt-Bleker A et al. *J. Phys. D* **47** 145201 (2014)
257. Hübner M et al. *Rev. Sci. Instrum.* **82** 093102 (2011)
258. Laroche G et al. *Rev. Sci. Instrum.* **83** 103508 (2012)
259. Chatain A et al. *Plasma Sources Sci. Technol.* **29** 085019 (2020)
260. Campargue A, Romanini D, Sadeghi N *J. Phys. D* **31** 1168 (1998)
261. Escribano R, Campargue A *J. Chem. Phys.* **108** 6249 (1998)
262. Boogaarts M G H et al. *Chem. Phys. Lett.* **326** 400 (2000)
263. Lang N et al. *IEEE Trans. Plasma Sci.* **37** 2335 (2009)
264. Gianella M et al. *Plasma Sources Sci. Technol.* **27** 095013 (2018)
265. Klose S-J et al. *Plasma Sources Sci. Technol.* **29** 085011 (2020)

266. Starikovskaia S M et al. *Proc. SPIE* **4450** 63 (2002)
267. Akishev Yu S et al. *Proc. SPIE* **4450** 90 (2002)
268. Foissac C et al. *J. Phys. D* **33** 2434 (2000)
269. Sadeghi N, Foissac C, Supiot P *J. Phys. D* **34** 1779 (2001)
270. Stancu G D et al. *J. Phys. Chem. A* **114** 201 (2010)
271. Jans E R et al. *J. Mol. Spectrosc.* **365** 111205 (2019)
272. Hancock G et al. *J. Phys. D* **39** 1846 (2006)
273. Pazyuk V S et al. *Quantum Electron.* **31** 363 (2001); *Kvantovaya Elektron.* **34** 363 (2001)
274. Sousa J S et al. *Appl. Phys. Lett.* **93** 011502 (2008)
275. Sousa J S et al. *Eur. Phys. J. Appl. Phys.* **47** 22807 (2009)
276. Gupta M et al. *Chem. Phys. Lett.* **400** 42 (2004)
277. Sousa J S et al. *J. Appl. Phys.* **109** 123302 (2011)
278. Kotterer M, Conceicao J, Maier J P *Chem. Phys. Lett.* **259** 233 (1996)
279. Yalin A P et al. *Plasma Sources Sci. Technol.* **11** 248 (2002)
280. Pan F, Oka T *Phys. Rev. A* **36** 2297 (1987)
281. Liu K et al. *J. Phys. D* **54** 065201 (2021)